



seit 1558

Friedrich-Schiller-Universität Jena



WAGENINGEN UNIVERSITY
WAGENINGENUR



Max-Planck-Institut
für Meteorologie



LSCE



Met Office

LUXEMBOURG
INSTITUTE
OF SCIENCE
AND TECHNOLOGY

LIST



GAMMA REMOTE SENSING

Land Cover CCI

CLIMATE ASSESSMENT REPORT YEAR 3 - 1.0

Document Ref:	CCI-LC-CARv3
Deliverable Ref:	CAR-yr3
Version:	1.0
Creation Date:	2017-07-01
Last Modified:	2017-07-11

	Ref	LC CCI Phase 2: Climate Assessment Report, Year 3		
	Issue	1.0	Date 2017-07-11	
	Page	2		

This page is intentionally blank.

	Ref	LC CCI Phase 2: Climate Assessment Report, Year 3		
	Issue	1.0	Date 2017-07-11	
	Page	3		

Document Signature Table

	NAME	FUNCTION	COMPANY	SIGNATURE	DATE
PREPARED	Vladislav Bastrikov	Postdoctoral research scientist	LSCE/CNRS		
PREPARED	Philippe Peylin	Research Scientist	LSCE/CNRS		
PREPARED	Catherine Ottlé	Research Scientist	LSCE/CNRS		
PREPARED	Andy Hartley	Research Scientist	MOHC		
PREPARED	Stefan Hagemann	Research Scientist	MPI-M		
PREPARED	Goran Georgievski	Research Scientist	MPI-M		
PREPARED	Debbie Hemming	Research Scientist	MOHC		
PREPARED	Neil Kaye	Research Scientist	MOHC		
PREPARED	Gillian Kay	Research Scientist	MOHC		
VERIFIED					
APPROVED					

Document Change Record

VERSION	DATE	DESCRIPTION	APPROVED
0.1	2012-09-10	First version of the Deliverable name	
1.0	2017-07-01	First version of the CARv3 (Phase 2, Year3)	

Document Diffusion List

ORGANISATION	NAME	QUANTITY
ESA	O. Arino, F. Ramoino	

	Ref	LC CCI Phase 2: Climate Assessment Report, Year 3		
	Issue	1.0	Date 2017-07-11	
	Page	4		

SYMBOLS AND ACRONYMS

APAR	Absorbed Photosynthetically Active Radiation
AVHRR	Advanced Very High Resolution Radiometer
BL	Broadleaf
CAR	Climate Assessment Report
CCI	Climate Change Initiative
CCI-LC	Climate Change Initiative – Land Cover
CGLS	Copernicus Global Land Service
CMIP	Coupled Model Intercomparison Project
CO ₂	Carbon Dioxide
CRU	Climate Research Unit
CW	Cross Walking
DGVM	Dynamic Global Vegetation Model
ECV	Essential Climate Variable
ESA	European Space Agency
ESM	Earth System Model
ET	EvapoTranspiration
GIMMS	Geographic Information Mapping and Management System
GPCC	Global Precipitation Climatology Centre
GPP	Gross primary productivity
HadGEM2A	Met Office Hadley Centre’s Global Environmental Model
IGBP	International Geosphere-Biosphere Programme
JSBACH	The LSM used at MPI-M
JULES	The LSM used at MOHC (the Joint Uk Land-Environment Simulator)
K-G	Köppen-Geiger
LAI	Leaf Area Index
LC	Land Cover
LCCS	Land Cover Classification System
LSCE	Laboratoire des Sciences du Climat et de l’Environnement
LSM	Land Surface Model
LST	Land Surface Temperature
LUH	Land Use Harmonisation
LULCC	Land Use and Land Cover Change
MOHC	Met Office Hadley Centre
MOSES	Met Office Surface Exchange Scheme
MPI	Max Planck Institute
MPI-M	Max Planck Institute für Meteorologie
NCAR	National Center for Atmospheric Research

	Ref	LC CCI Phase 2: Climate Assessment Report, Year 3		
	Issue	1.0	Date 2017-07-11	
	Page	5		

NCEP	National Centers for Environmental Prediction
NDVI	Normalized Difference Vegetation Index
NIR	Near Infrared
NL	Needleleaf
NOAA	National Oceanic and Atmospheric Administration
NVP	Non vascular plants
ORCHIDEE	The LSM used at LSCE (ORganizing Carbon and Hydrology in Dynamic EcosystEms)
PAR	Photosynthetically Active Radiation
PFT	Plant Functional Type
PUG	Product User Guide
SPOT-VGT	Système Pour l'Observation de la Terre Vegetation
TM	Thematic mapper
TRENDY	TRENDY
TRIFFID	Top-down Representation of Interactive Foliage and Flora Including Dynamics
UCL	Université Catholique de Louvain
VIS	Visible
WEED	Model for the representation of wetland extent dynamics
WFDEI	WATCH Forcing Data methodology applied to ERA-Interim data

	Ref	LC CCI Phase 2: Climate Assessment Report, Year 3		
	Issue	1.0	Date 2017-07-11	
	Page	6		

REFERENCE DOCUMENTS

Applicable documents

ID	TITLE	ISSUE	DATE
[AD-1]	CCI Land Cover project: Climate Assessment Report	2.0	27.04.2016
[AD-2]	ESACCI-LC-PUG-v2.5. Land Cover CCI Product User Guide. Version 2.5. Last Modified 2016-01-26: http://www.esa-landcover-cci.org/?q=documents		
[AD-3]	LC-CCI Newsletter. Climate Change Initiative. Issue 5 August 2013. http://www.esa-landcovercci.org/sites/default/files/documents/documents/Newsletters/LC_CCI_Newsletter5_LPSymp.pdf		
[AD-4]	CCI-LC ATBD Phase I. Land Cover Climate Change Initiative - Algorithm Theoretical Basis Document		2013

TABLE OF CONTENTS

SYMBOLS AND ACRONYMS	4
REFERENCE DOCUMENTS	6
TABLE OF CONTENTS	7
1 INTRODUCTION	9
2 LSCE: ASSESSMENT OF THE ADDED VALUE OF THE NEW LAND COVER MAPS WITHIN THE ORCHIDEE MODEL	11
2.1 Construction of a web-site to display all CCI_LC results.....	11
2.2 Update and evaluation of the CCI_LC-derived ORCHIDEE PFT maps for CMIP6.....	13
2.2.1 Adjustment of the cross-walking table.....	14
2.2.2 Evaluation of the annual CCI_LC-derived PFTs.....	16
2.3 Impact of new CCI LC maps on the water, energy and carbon budgets simulated by ORCHIDEE.....	19
2.3.1 Method.....	19
3.1.2.1. Datasets.....	19
3.1.2.2. Simulation protocol.....	21
2.3.2 Analysis of LC versus meteorological forcing impacts.....	22
3.1.2.3. Global analysis.....	22
3.1.2.4. Regional analysis.....	27
3 MPI-M: ASSESSMENT OF THE IMPACT OF THE NEW LAND COVER MAPS WITHIN THE MPI-ESM MODEL	29
3.1 Sensitivity of the MPI-ESM to the uncertainty in ESA-CCI Land Cover observation.....	29
3.1.1 Introduction.....	29
3.1.2 Data and Methods.....	30
3.1.2.1. ESA-CCI Land Cover Data.....	31
3.1.2.2. MPI-ESM.....	31
3.1.2.3. Cross-walking procedure.....	32
3.1.3. Results.....	33
3.1.3.1. The range of PFT uncertainty.....	34
3.1.3.2. MPI-ESM sensitivity to the PFT uncertainty.....	37
3.1.4. Conclusions.....	45
3.2. Assessing Carbon Emissions from Wildfires using observed data from ESA-CCI-Fire and the JSBACH vegetation model.....	46
3.3. Benchmarking sensitivity of biophysical processes to leaf area changes in land surface models.....	48
3.4 Recommendation.....	52
4. MOHC ASSESSMENT OF SR AND NDVI CONDITION PRODUCTS FOR EVALUATING THE GROWING SEASON IN JULES	53
4.1. Introduction.....	53
4.2. Method.....	54
4.2.2. Datasets.....	54
4.2.2.1. Copernicus NDVI v1.3 (Copernicus-NDVI).....	54
4.2.2.2. MERIS Surface Reflectance (SR-NDVI).....	54
4.2.2.3. NDVI Condition Product (NDVI Condition).....	54
4.2.2.4. JULES NDVI Simulations (JULES-NDVI).....	54
4.2.3. Obtaining the data.....	55
4.2.4. Giorgi regions.....	55
4.2.5. Phenology Indicators.....	55
4.2.6. Approach.....	58

	Ref	LC CCI Phase 2: Climate Assessment Report, Year 3		
	Issue	1.0	Date 2017-07-11	
	Page	8		

4.3.	Assessment	58
4.3.2.	Data Coverage	58
4.3.3.	Spatial Scale of aggregation	60
4.3.4.	Mean seasonal cycle	62
4.3.5.	Phenology Indicators	65
4.3.6.	Caveats to the detection of indicators	67
4.4.	Significance of results	69
4.5.	Conclusions and recommendations	69
5.	INTERCOMPARISON OF CLIMATE MODELLERS' PRODUCT ASSESSMENT	71
5.1.	Introduction	71
5.2.	Protocol for the model inter-comparison	71
5.2.2.	Initial data - LCC maps	71
5.2.3.	Experimental Set up	76
5.2.4.	Valorization of the results with an interactive web site	77
5.3.	Regional to continental scale results	77
5.3.2.	Method	77
5.3.3.	Energy and Water budget	78
5.4.	Perspectives	81
5.4.2.	Impact of land cover change at local scale	81
5.4.3.	Opportunities to exploit high resolution land cover and land cover change maps	82
6.	REFERENCES	84
7.	APPENDIX	91
7.1.	Appendices for MOHC model results	91
7.1.2.	Appendix MOHC – 1	91
7.1.3.	Appendix MOHC - 2	95
7.1.4.	Appendix MOHC - 3	97

List of Figures

List of Tables

	Ref	LC CCI Phase 2: Climate Assessment Report, Year 3		
	Issue	1.0	Date 2017-07-11	
	Page	9		

1 INTRODUCTION

Land Cover (LC) and its bio-geochemical and bio-geophysical feedbacks are important for the understanding of climate and its vulnerability to changes on the surface of the Earth. According to the Global Climate Observing System (GCOS) LC is classified as one of Essential Climate Variables (ECV). It represents different properties of the impervious (artificial and natural), urban, water bodies, snow and ice, bare or vegetated area on the Earth's surface. LC and in particular vegetation, controls water and energy exchange, photosynthesis rates, nutrient levels and surface roughness at the land-atmosphere interface and therefore influences the many aspects of Earth's climate. Comprehensive review of research over recent decades provided by Mahmood et al (2014) highlights the impacts of LC changes on atmospheric temperature, humidity, cloud cover, circulation, and precipitation as well as local, regional and global climate forcing.

Recent studies have shown that vegetation, especially tree cover, has an impact on terrestrial water cycle, energy balance and carbon cycle. By combining available observations of evapotranspiration (ET) in geographic modelling and verifying results with a Land Surface Model (LSM), Sterling et al (2013) found that current anthropogenic LC change reduces annual ET by approximately 3500 km³/yr. Previously, Gordon et al (2005) estimated a decrease in global vapor flows from land by 4% (3000 km³/yr), but also an increase in vapor flow due to irrigation (2600 km³/yr), so that net change in global vapour flow over the land according to this study is just slightly decreased. Wang and Dickinson (2012) have reviewed basic theories, observational methods, satellite algorithms, and land surface models for terrestrial ET and its relation to LC, wind and precipitation. They found that estimates of ET vary, depending on theoretical expression and observational method, while land surface models provide widely different ratios of transpiration by vegetation to total terrestrial ET.

Applying an observation-driven diagnostic model, Zhang et al (2016) found opposing trends in ET components during the past three decades. The increase of transpiration and vaporization of intercepted rainfall from vegetation is counteracted by decreasing soil evaporation. They have extended critique of land surface models, arguing that most of the Earth System Models (ESMs) used in Coupled Model Intercomparison Project phase 5 (CMIP5) do not show opposing trends in ET components.

Temperature change due to LC change is strongly connected with changes in albedo. Davin and Noblet-Ducoudré (2010) found that in climate models increased albedo due to deforestation may result with 1 degree cooling. This result is confirmed for high latitudes by comparisons of temperature at forested eddy covariance towers (Lee et al, 2011). Changes in surface albedo are the key biophysical mechanism alternating terrestrial energy budget and hence the climate. On the basis of historical land use data (Hurtt et al, 2006, 2011), and satellite land cover products derived from Moderate Resolution Imaging Spectroradiometer (MODIS) and Advanced Very High Resolution Radiometer (AVHRR), Ghimire et al (2014) estimated mean annual global albedo increase due to land cover change during 1700–2005 to be 0.00106 ± 0.00008 . According to the authors, this change is mainly driven by snow exposure due to land cover transitions from natural vegetation to agriculture. Jones et al (2015) have conducted a study with Community Earth System to estimate changes in radiative forcing due to albedo changes associated with major LC transitions. They found that total global radiative forcing from albedo change due to potential future LC land use change, ranging from -0.06 to -0.29 W/m² by 2070. Zhao and Jackson (2014) examined biophysical forcing and climatic impact of vegetation replacement across North America

	Ref	LC CCI Phase 2: Climate Assessment Report, Year 3		
	Issue	1.0	Date 2017-07-11	
	Page	10		

by comparing satellite-derived products. They estimated the mean albedo-induced radiative forcing for each land conversion in terms of carbon emission.

The largest source of terrestrial CO₂ as well as the largest source of uncertainty is vegetation Gross Primary Production (GPP). In particular, due to a possible overestimation of coverage rate of forests in global eco-system, their GPP may be overestimated according to Ma et al (2015). Evaluating components of the global carbon cycle representation in CMIP5 models, Anav et al (2013) reported general overestimation of photosynthesis and leaf area index and therefore overestimated terrestrial carbon uptake, for most of the models. Le Quere et al (2016) in their annual report of global carbon budget for the last decade (2006-2015) estimated annual uncertainty due to land use change in carbon emission to ± 0.5 PgC/year, while the uncertainty of terrestrial carbon uptake is ± 0.9 PgC/year.

Despite of clear impact of LC change on climate, studies with numerical models assimilating LC changes as derived from satellite observations are relatively rare. The reason for that might be that the period of satellite data acquisition is too short to produce reliable LC change maps. However, one such map - the first satellite-derived long term record of global land cover change - has been produced recently in the frame of the ESA-CCI-LC project. However, numerical models used to study climate and observational techniques are still far from perfect. The internal variability of climate models, in addition to well-known biases in precipitation and climate variability are the main origins of uncertainty in the climate system that may affect our ability to interpret the impacts of land use change in coupled land-atmosphere climate models.

In this context, the 3 climate user groups of the ESA-CCI-LC project have used 3 different land surface models, ORCHIDEE, JSBACH and JULES, to investigate the impact of having i) new land cover maps at medium resolution (300 m) derived from satellite observations and ii) new estimate of annual land cover changes over the period 1992 – 2015. The 3 groups have conducted separate studies focusing on different aspect of the climate system (reported in the next 3 sections) as well as a joint experiment to assess the impact of the new land cover change product (reported in section 5).

	Ref	LC CCI Phase 2: Climate Assessment Report, Year 3		
	Issue	1.0	Date 2017-07-11	
	Page	11		

2 LSCE: ASSESSMENT OF THE ADDED VALUE OF THE NEW LAND COVER MAPS WITHIN THE ORCHIDEE MODEL

Authors: **Catherine Ottlé¹, Philippe Peylin¹ and Vladislav Bastrikov¹**
Contributors: **Natasha MacBean², Devaraju Narayanappa¹, Wei Li¹**

¹Laboratoire des Sciences du Climat et de l'Environnement, Gif-sur-Yvette, France.

²School of Natural Resources and the Environment, University of Arizona, USA.

In Year 3 of Phase 2 of the CCI LC project, the LSCE team has continued to assess the impact of the new land cover maps for a range of applications. The first one concern the mapping of the land cover classes derived from satellite into the plant functional types that are used in land surface models, through a revision of the cross walking table. The second aspect concerns the merge of the ORCHIDEE PFTs derived from the CCI product with the LUHv2.2 land cover historical transitions to derive the annual land cover maps that will be used in the upcoming CMIP6 simulations, including a comparison between the CCI-LC-derived PFTs and few other products. Finally, we have evaluated the impact of the new CCI land cover product on the carbon/water/energy fluxes simulated by ORCHIDEE (1992-2015 period). Broadly this is the overall context behind the work we have done this past year (see sections below).

2.1 Construction of a web-site to display all CCI_LC results

Most of the work and results associated to the use of the CCI land cover products, including the results of the joint experiment described in section 5, are summarized in a dedicated web-site (<https://orchidas.lsce.ipsl.fr/dev/LCCCI.php>). This web-site comprises several pages:

1. A page describing the new cross walking table (see section 2.2): <https://orchidas.lsce.ipsl.fr/dev/LCCCI.php>
2. A page displaying the 22 CCI_LC maps from the latest product version (v2.0.7) for several selected years: https://orchidas.lsce.ipsl.fr/dev/LCCCI_ccimaps.php
3. A page displaying the so-called "generic PFTs" that will be used by the three modeling groups, obtained from different version of the cross walking table: https://orchidas.lsce.ipsl.fr/dev/LCCCI_pftmaps.php
4. A page displaying the current 13 PFTs for ORCHIDEE derived from the generic PFTs distribution with specific additional grouping and the split between C3 and C4 plants (see section 2.2): https://orchidas.lsce.ipsl.fr/dev/LCCCI_orcpftmaps.php
5. A page comparing some grouping of the ORCHIDEE PFTs into major land cover type to the LUHv2.2 product (used to provide the historical transition land cover for CMIP6): https://orchidas.lsce.ipsl.fr/dev/LCCCI_luhmaps.php

	Ref	LC CCI Phase 2: Climate Assessment Report, Year 3		
	Issue	1.0	Date 2017-07-11	
	Page	12		

6. A page comparing the new ORCHIDEE PFTs derived from the CCI_LC maps with the old PFTs used for the CMIP5 exercise and based on the Olson dataset (Olson et al., 1983): https://orchidas.lsce.ipsl.fr/dev/LCCCI_ar5maps.php
7. A page displaying the results from several ORCHIDEE simulations with different land cover products and different climate forcing to evaluate the impact of the new CCI land cover maps: https://orchidas.lsce.ipsl.fr/dev/LCCCI_orcsims.php
8. A page displaying the results of the joint experiment between the 3 modeling groups (ORCHIDEE, JSBACH and JULES) to assess the impact of the annual land cover changes newly produced (see section 5): https://orchidas.lsce.ipsl.fr/dev/LCCCI_sims.php

Figure 1 below illustrates the layout for the two model results inter-comparison pages (ORCHIDEE dedicated page and the page for the joint experiment with the three models). This web-page offers the following capabilities:

- a) A map facility where we can select: i) the type of variables to display (related to energy, water and carbon cycles), ii) the temporal average (yearly or seasonal) and iii) the type of plot (raw data, difference between the “lcc” and a “ref” simulations for each model and difference with few “data oriented product” (referred as observations))
- b) A time series facility where we can select: i) an ensemble of regions from a predefined set of continental to regional domains (regions defined accordingly to the observed land cover changes) and ii) the temporal average (yearly, monthly or the monthly mean climatology).

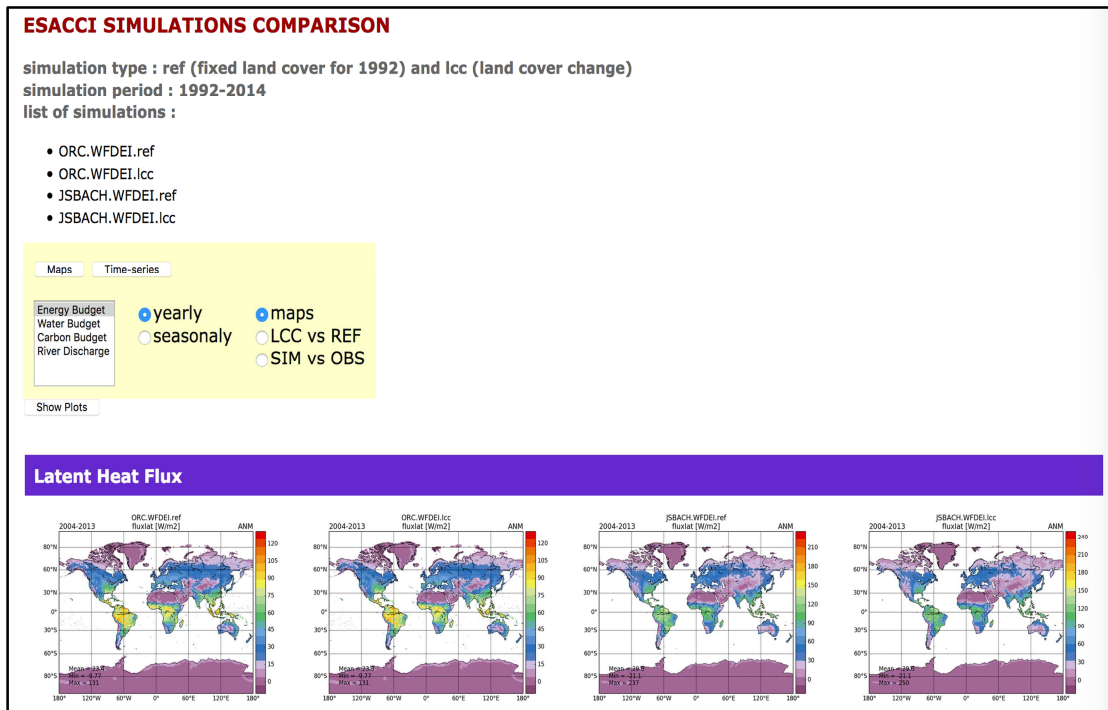


Figure 1: Display of the web-site for the comparison of the different simulations.

2.2 Update and evaluation of the CCI_LC-derived ORCHIDEE PFT maps for CMIP6

As described in the previous Climate Assessment Report (CAR), we are using both the CCI_LC-derived PFT map and Land Use Harmonisation (LUH) dataset provided by George Hurtt (Hurtt et al., 2011), in order to construct a historical LC time series map for the upcoming CMIP6 simulations. Natural vegetation will be prescribed from the CCI LC map while crops and urban area will be prescribed from the LUH data. The backward construction will be done using the LUH year-to-year transition matrix. Overall the derivation of the land cover maps for ORCHIDEE follows several steps that are summarize below and presented in dedicated web-pages as detailed above:

1. Definition and use of a cross walking table to derive the so-called “generic” PFTs that will be use by the three modeling groups involved in this project. The spatial distribution of these PFTs is available at: https://orchidas.lscce.ipsl.fr/dev/LCCCI_pftmaps.php
2. Processing of the “generic” PFTs in order to derive the 13 PFTs of ORCHIDEE; In particular the shrub land cover are merged into the tree land cover given that ORCHIDEE in its standard configuration do not treat shrub separately. The grass and crop PFTs are further split between C3 and C4 photosynthetic pathway using the distribution of C4 plant from still et al. (2003); The resulting ORCHIDEE PFTs are display under: https://orchidas.lscce.ipsl.fr/dev/LCCCI_orcpftmaps.php

	Ref	LC CCI Phase 2: Climate Assessment Report, Year 3		
	Issue	1.0	Date 2017-07-11	
	Page	14		

3. Merge of the current CCI_LC-derived PFT with the LUHv2.2 land cover product for the year 2014 in order to keep the cropland and city areas from LUH; the other PFT are expanded/shrunked accordingly.
4. Backward reconstruction of the whole historical PFT changes (from present to year 850) using the transitions provided in LUHv2.2 in order to provide LCC compliant with the CMIP6 protocol.

The sections below describe the revision of the cross walking table (step 1) and provide a comparison of the ORCHIDEE PFTs (from step 2) with other products.

2.2.1 Adjustment of the cross-walking table

Analysis conducted during year 2 led us to propose a first revision of the cross walking table (CWT) established in Phase 1 of the project (and documented in Poulter et al., 2015). Further analysis conducted in year 3, especially some in depth comparison of the CCI-LC product with the land cover of the last LUH release, the version v2.2, led us to reconsider again the CWT. Note that this is not a simple task as the class descriptions, and indeed purpose, of the two datasets are different. More specifically we have compared the fraction and spatial distribution of crop areas between the two products for the recent years (1992 to 2014). The large discrepancies (already noticed in the previous CAR report) pushed us to further improve the CWT established in year 2 of the project (based on a revision of the CWT for the mixed land cover classes). The primary difference was a much larger crop area in the annual CCI-LC maps (around 24 Mkm²) than in LUHv2.2 (around 16 Mkm²). This difference pushed us to reconsider what should be the split of LCCs containing crop types (classes 10, 11, 12 20, 30 and 40) into fractions of crop, grass and possibly tree PFTs.

Of the land cover types that consist fully of cropland, grass or shrubs, we decided that only 90% can be used for the equivalent PFT, following Goldewijk et al. (2016). This is to account for small areas of infrastructure, wetlands, unsuitable terrain, steep slopes or small patches of vegetation that are not explicitly identified in the original land cover product. Note finally that the ESA cropland land cover types identified at 300 m resolution are most likely a mix of cropland and intensive pasture land in many regions.

The results of these refinements are reported in the web-page:
<https://orchidas.lsce.ipsl.fr/dev/LCCCI.php>

On this page you can find a table that describes the CWT and its different revisions. Figure 2 below displays the different revision of the CWT: i) the original values derived in phase 1 of the project (CWTv1.0), the revised values derived in year 2 of this phase 2 (CWTv2.0) and the final values derived in year 3 (CWTv2.3). The recent changes have thus led to a significant decrease of the cropland PFT fraction. Figure 3 illustrates the difference in cropland fraction due to changes in the CWTs: the cropland area decreases by 2.5 Mkm² at the profit of natural grass that increases by 2Mkm². The spatial distribution remains similar and these changes are mainly due to changes in fractional covers.

• red — new values under discussion (CWT v2.3, including blue values as well)
 • blue — values used in LSCE aggregation (CWT v2.0)
 • black — values from the default CWT coming with "lc-user-tools-3.11" (link : <http://geo10.elie.ucl.ac.be/home/lc-user-tools-3.11.zip>) (CWT v1.0)

CCI CLASS	KG CLASS	TREES				SHRUBS				GRASSES		Bare Soil	Water	Snow and Ice	Urban	No Data
		TrBrEv	TrBrDe	TrNeEv	TrNeDe	ShBrEv	ShBrDe	ShNeEv	ShNeDe	NatGr	Crops					
0	no data															100
10	cropland, rainfed									10	90					0
11	cropland, rainfed, herbaceous cover									10	90					0
12	cropland, rainfed, tree or shrub cover						70				30					50
20	cropland, irrigated or post-flooding									10	90					0
30	mosaic cropland (>50%) / natural vegetation (tree, shrub, herbaceous cover) (<50%)	5	5			5	5	5		15	60					
40	mosaic natural vegetation (tree, shrub, herbaceous cover) (>50%) / cropland (<50%)	7.5	7.5			10	15	10		30	20					25
50	tree cover, broadleaved, evergreen, closed to open (>15%)	90				5	5									
60	tree cover, broadleaved, deciduous, closed to open (>15%)		50				20			30						15
61	tree cover, broadleaved, deciduous, closed (>40%)		70				15			15						
62	tree cover, broadleaved, deciduous, open (15-40%)		30				25			45		0				10
70	tree cover, needleleaved, evergreen, closed to open (>15%)			70		5	5	5		15						
71	tree cover, needleleaved, evergreen, closed (>40%)			70		5	5	5		15						
72	tree cover, needleleaved, evergreen, open (15-40%)			30			0	25		45		0				30
80	tree cover, needleleaved, deciduous, closed to open (>15%)				50	2.5	2.5	2.5	12.5	30						15
81	tree cover, needleleaved, deciduous, closed (>40%)				70	5	5	5		15						
82	tree cover, needleleaved, deciduous, open (15-40%)				30		0	0	25	45		0				30
90	tree cover, mixed leaf type (broadleaved and needleleaved)		30	20	10	5	5	5		25		0				10
100	mosaic tree and shrub (>50%) / herbaceous cover (<50%)	10	20	5	5	5	10	5		40						
110	mosaic herbaceous cover (>50%) / tree and shrub (<50%)	5	10	5		5	10	5		60						
120	def					20	20	20		20		20				
	1					15	30	15		40						
	21					15	30	15		40						
	22					15	30	15		40						
	31					20	40	20		20						
	32					20	40	20		20						

Figure 2: Part of the cross-walking tables used to make the PFT maps (the full CWT is displayed under <https://orchidas.lsce.ipsl.fr/dev/LCCCI.php>): in black the original values derived in Phase 1 of the project and documented in Poulter et al. (2015); in blue the revised values during year 2 of Phase 2 of the project where the sparse

	Ref	LC CCI Phase 2: Climate Assessment Report, Year 3		
	Issue	1.0	Date 2017-07-11	
	Page	16		

vegetation classes (150-153) were modified (following Ottlé et al. (2013)) ; in red the last modification during year 3 of Phase 2 for the cropland classes.

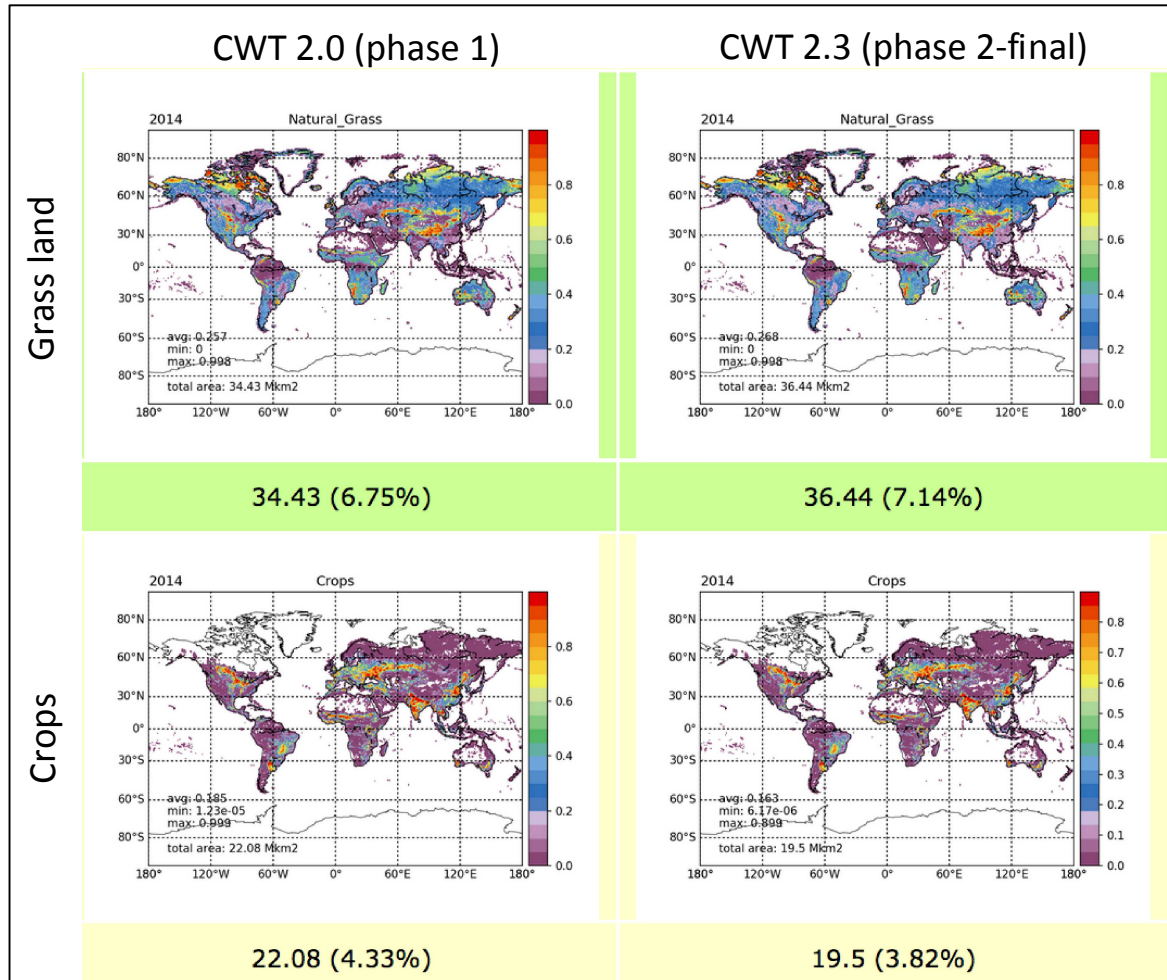


Figure 3: Maps of the crop areas with the surface in Mkm² (as well as the global percentage of coverage) for the grassland and the cropland with the two cross walking table.

2.2.2 Evaluation of the annual CCI_LC-derived PFTs

After the application of the cross walking table and further grouping to match the 13 ORCHIDEE PFTs the global and regional areas of forest, cropland and grassland PFTs are compared for different years with other products. We used the LUHv2.2 land cover classes and transitions (Hurt et al., 2011) and the forest cover from Hansen et al. (2013) and from Houghton et al. (2017).

The first major difficulty concerns the affectation of the shrub-land derived from the CCI-LC as a generic PFT into a current ORCHIDEE PFT. Indeed the main version of ORCHIDEE does not treat yet the shrubs explicitly. We thus had to affect the generic shrub PFT into one/several of the 13 PFTs of ORCHIDEE; we choose given the biogeochemical properties of shrub to consider them as tree, given that from a structure point of view shrubs can be viewed as small trees. However for

the comparison to the other forest products and LUH product, this is not optimal and has significant impact; we will indeed overestimate the ORCHIDEE tree cover compared to the others forest products that do not usually consider shrubs as trees.

Excluding Shrubs:

If we exclude the shrubs the CCI-LC derived forest, cropland and grassland PFTs are 30, 19 and 34 million km², respectively, in year 2000. Figure 4 compares these three broad land cover PFTs deduced from the CCI_LC maps with the other products.

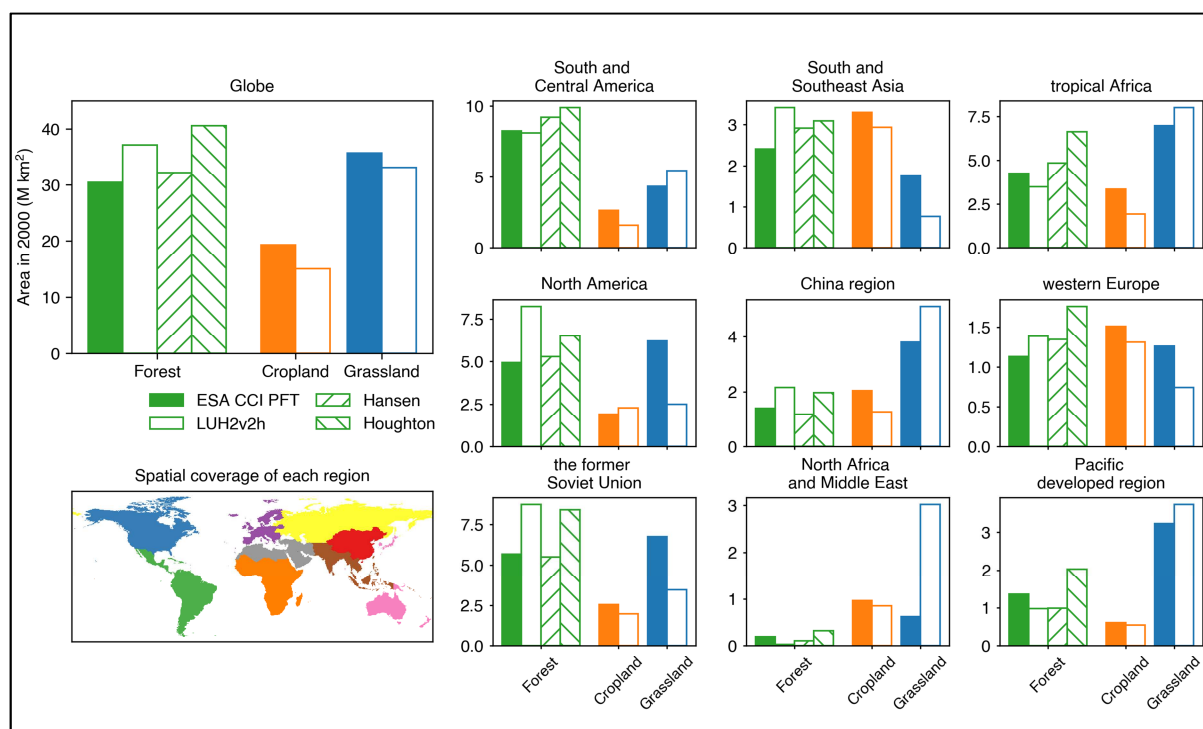


Figure 4: Comparison of forest, cropland and Grassland areas between the ESA-CCI derived product, the LUHv2.2 product, the Hansen et al. (2013) forest product and the Houghton et al. (2017) forest product, for 9 continental-scale regions.

Global forest area is around 8, 3 and 12 million km² lower than that from LUHv2.2, Hansen et al. (2013) and Houghton et al. (2017), respectively. Global cropland area from ESA CCI is still larger than that from LUHv2.2 (19 vs. 15 million km²), while the difference in global grassland area is slightly smaller. Figure 4 also compares for 9 continental-scale regions the total area of forest, cropland and grassland between the different products. Forest area from ESA CCI are slightly lower than that from Hansen et al. (2013) in the regions where most of forests are distributed, i.e. South and Central America, tropical Africa, North America and the former Soviet Union. Forest area from LUHv2h (Hurtt et al., 2011) is larger than that from ESA CCI in most regions except in South and Central America, tropical African and Pacific developed region. Forest area from Houghton et al. (2017), however, is systematically higher than that from ESA CCI in all regions. Cropland area from ESA CCI matches that from LUHv2h (Hurtt et al., 2011) in North America but is higher in all the other regions. Although the global grassland area is relatively similar between ESA CCI and LUHv2h (Hurtt et al., 2011), larger differences are shown at regional scale. Grassland area from ESA CCI was found to be much higher than that from LUHv2h (Hurtt et al., 2011) in North America and the former Soviet Union (4.0 and 3.5 million km² higher, respectively)

but much lower (2.4 million km²) in North Africa and Middle East. Such comparison will be summarized in an upcoming paper (Li et al., in prep).

Including Shrubs into Tree for the standard ORCHIDEE PFTs:

For the standard ORCHIDEE PFTs we include the shrub land cover types into the corresponding tree PFTs (i.e. depending on the phenology). The resulting PFTs distribution (Figure 5) shows significant differences with the LUHv2.2 product and differences that are exacerbated compared to the previous comparison. These results are also accessible under a dedicated web-site: https://orchidas.lsce.ipsl.fr/dev/LCCCI_luhmaps.php. Large spatial differences occurs with more forest cover in CCI-derived ORCHIDEE PFTs in the boreal zone of Siberia compared to LUH but lower forest cover in the 50°N-70°N latitudinal band. Below 50°N there is on average more forest cover in the ORCHIDEE map but with some regional patterns linked to shrub cover over “arid” regions. For the crop, Figure 5 displays the same feature as described above, wit more crop in most crop intensive regions.

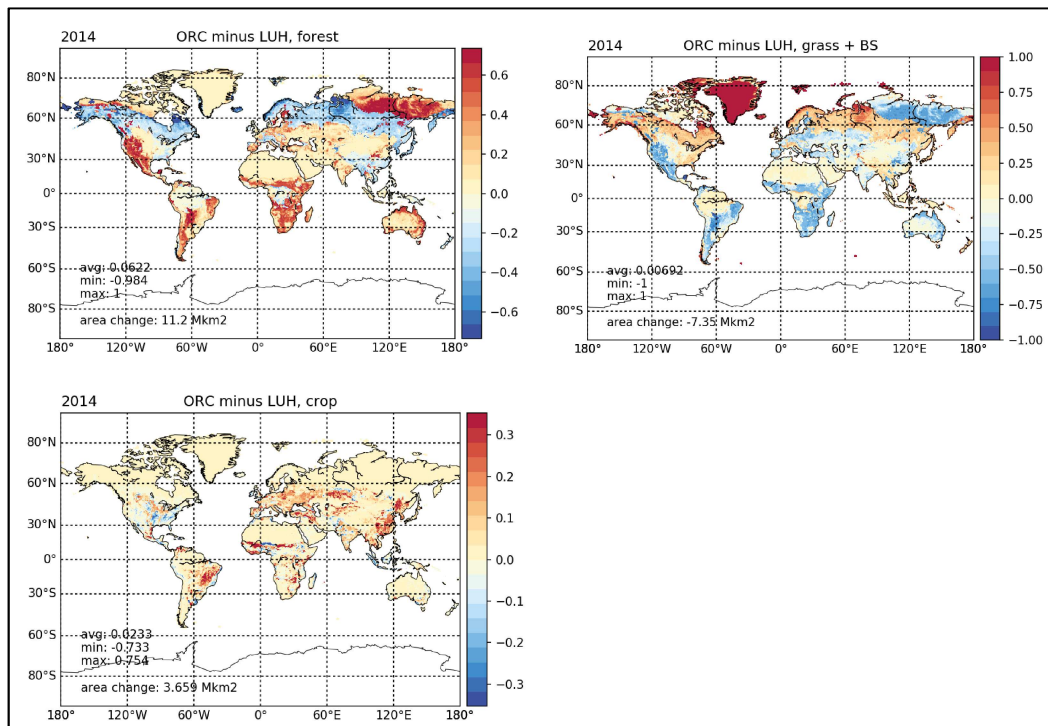


Figure 5: Differences of forest, grassland plus bare soil and cropland areas between the ORCHIDEE PFTs (derived from the CCI-LC) and the LUHv2.2 dataset from G. Hurtt.

Gross annual land cover changes are also under investigation at LSCE with the objective to compare the annual changes with those provided in the LUHv2.2 product. However, such analysis is left for section 4 of this report, the joint section between the three modeling groups. The paper Wei et al. (in preparation) will also compare these gross land cover changes.

	Ref	LC CCI Phase 2: Climate Assessment Report, Year 3		
	Issue	1.0	Date 2017-07-11	
	Page	19		

2.3 Impact of new CCI LC maps on the water, energy and carbon budgets simulated by ORCHIDEE

The objectives were to evaluate the contribution of the new ORCHIDEE PFT maps generated for the CMIP6 project, in terms of water, carbon and energy budgets and to analyze the added value of the yearly products compared to the use of a single year map.

As already mentioned in section 1, the definition of land cover for land surface modeling is crucial because the surface coverage determines the surface albedo and consequently the partition of incident shortwave radiation and the energy available for the evapotranspiration. Moreover, land cover influences the hydric processes by conditioning the amount of water that will not be intercepted by the vegetation and that will reach the ground. The type of vegetation impacts also the soil water processes, the evapotranspiration but also the infiltration, because the soil hydric properties may depend, like in ORCHIDEE, on the root profile description which is PFT dependent. Therefore, we expect land cover maps to impact significantly the water and energy budgets simulated by our model as well as the carbon budget of terrestrial ecosystems.

To evaluate these impacts, we have performed a number of simulations with ORCHIDEE, in forced and coupled modes, i.e. by prescribing the input meteorological forcing and by using the IPSL climate model to analyze also the land-atmosphere retroactions. In this report, we present only the results obtained in forced mode. Additionally, in order to better assess the importance of the PFT maps used, we have tested two different atmospheric forcing covering the same time period of the CCI-LC product. The analysis was performed both at global and regional scales, annually and seasonally, focusing on the regions presenting the largest land cover differences. In the following, the methodology and the datasets used in this work are first presented.

2.3.1 Method

3.1.2.1. Datasets

The WFDEI and CRU-NCEP atmospheric forcing have been used in this work. The PFT maps based on the new CWT described in section 2.2 were used to prescribe the vegetation cover. The CMIP5 historical PFT map used as reference is also presented.

CRU-NCEP version 5 climate forcing:

The CRU-NCEP climate forcing, aggregates the high spatial (0.5°) but coarse temporal (monthly) resolution of the CRU-TS dataset with the NCEP reanalysis, which has a high temporal interval (6-hourly) but is only available at 2.5°. The CRU-NCEP climate forcing depends on CRU-TS. NCEP reanalysis are used to reconstruct the variability within each month after bi-linear interpolation to 0.5° except for precipitation. For this variable the original NCEP values are interpolated to the CRU grid cells (0.5°) each month. The CRU-NCEP dataset is available from 1901 to 2015 at global scale and version 5 has been used in this work.

WFDEI-GPCC climate forcing:

The WFDEI atmospheric forcing was generated by applying the methodology of the WATCH Forcing Data (WFD) on the ERA-Interim reanalysis (weedon et al. 2014). The ERA-Interim blends GCM modeled variables and a suite of observations by a 4D-Var (4-dimensional variable analysis)

	Ref	LC CCI Phase 2: Climate Assessment Report, Year 3		
	Issue	1.0	Date 2017-07-11	
	Page	20		

data assimilation system. All variables are bias-corrected by using CRU data, except for precipitation (including rainfall and snowfall). There are two versions of bias-corrected precipitation, which are based on CRU and GPCC dataset, respectively. The climate forcing used in our simulation is the GPCC version. The spatial resolution of the WFDEI forcing is 0.5 and the dataset covers the period of 1979–2013 with 3-hour interval. Figure 6 shows the spatial variability of the annual precipitation and surface air temperature (at 2m height) averaged on the period 1992-2013, as given by the WFDEI-GPCC dataset.

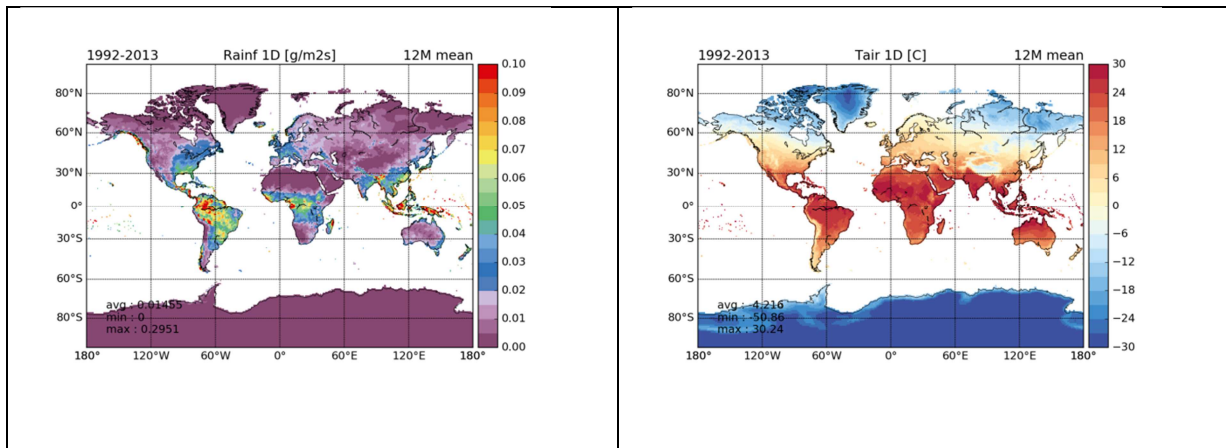


Figure 6: Annual precipitation and air temperature (at 2m) averaged over the 1992-2013 period, extracted from the WFDEI atmospheric dataset

CMIP5 PFT map:

The previous reference PFT maps for ORCHIDEE were derived from the Olson land cover classification, which contains 96 classes at a resolution of 5 km (Olson et al. 1983). A mapping to the ORCHIDEE PFTs was done at 0.72°, following Vérant et al. (2004) and a backward reconstruction of the historical land cover was performed with the previous version of LUH, similarly to the process described above for the derivation of the CMIP6 LC maps.

CMIP6 PFT map:

The generation of these new maps is described in section 2.2.

Comparison of CMIP5 vs CMIP6 PFT maps:

Figure 7 presents the differences between the two PFT maps for the year 2000 (i.e., the CMIP5 and CCI-derived CMIP6 products). The 13 PFT difference maps (CCI - CMIP5) show the spatial discrepancies and it also include the total area difference (in Mkm²) on the maps.

As highlighted in these maps, the main differences concern the bare soil and the grassland PFTs. The bare soil fraction is significantly larger in the CCI product compared to the CMIP5 one, in Arabia and Australia as well as in the boreal region. The total area of bare soil is larger by about 12Mkm², and this difference is mostly explained by the decrease of grasslands C3 (which decreased by about the same order of magnitude in these regions). The decrease of grasslands is in some regions like Sahel, compensated by the increase of croplands. Other transitions between the different types of forest can be seen, for example between evergreen's and raingreen's forests in Amazonia and Indonesia, or between broadleaf and evergreen forests in boreal regions. Note that the differences appearing in Greenland and Antarctic have no significance as they are due to ice-masking integrated in the CMIP5 product and not in the CCI-derived product (where iced pixels are currently merged with bare soil ones).

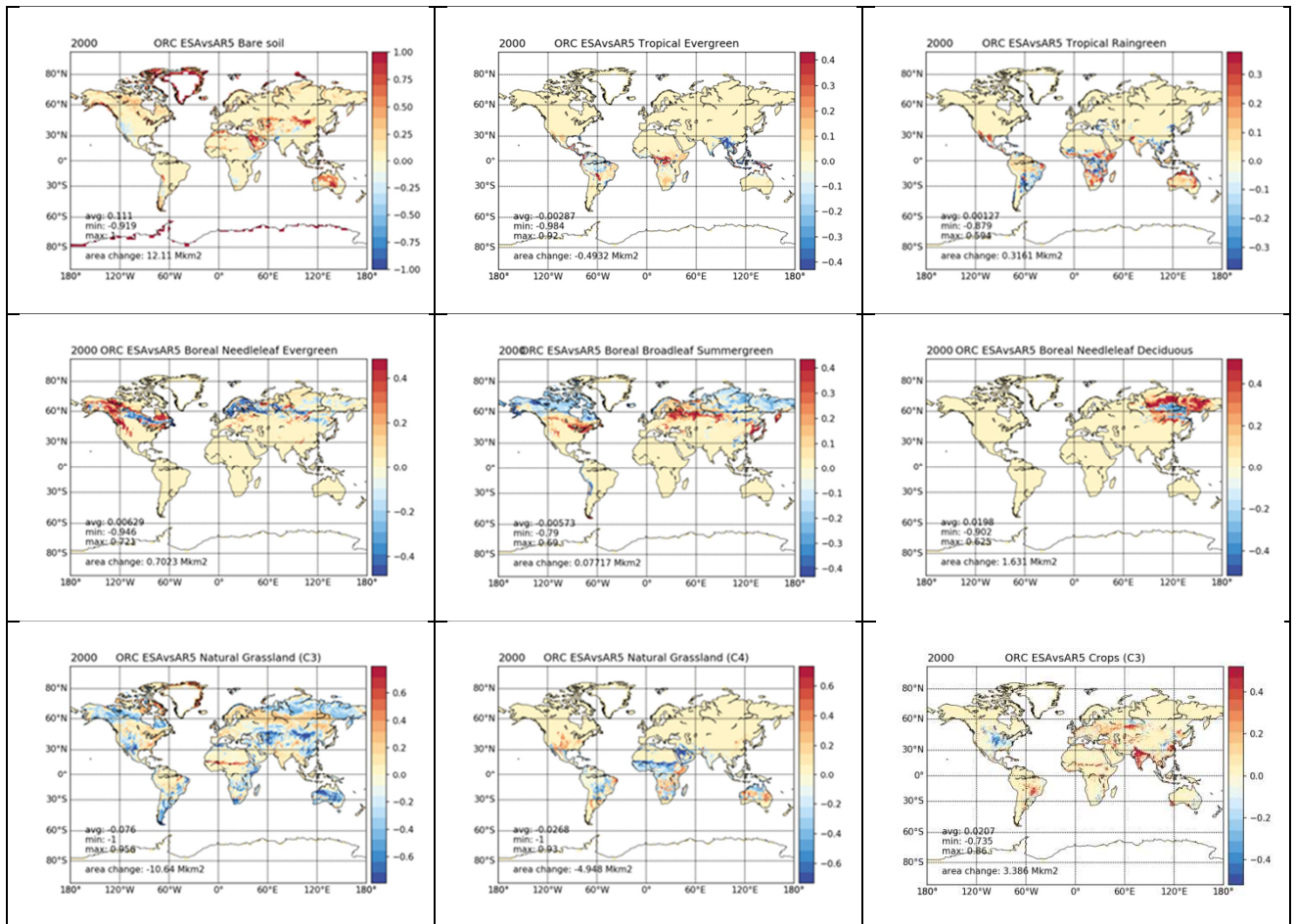


Figure 7: Maps of the differences between the ESA-CCI LC derived ORCHIDEE-PFTs and the old CMIP5 PFT map generated for Year 2000

3.1.2.2. Simulation protocol

To assess the added value of the new PFT map compared to the old CMIP5 maps, two simulations have been performed with the same atmospheric forcing (WFDEI). In the first one called "ORC-WFDEI-lcc", the new annual CCI-LC derived maps from 1992 to 2014 are used, the second one called "ORC-WFDEI-CMIP5" uses the annual CMIP5 LC maps generated for the previous CMIP5 exercise.

Three other simulations were performed with ORCHIDEE to analyze the relative impacts of the LC annual changes and of the atmospheric forcing. For the simulation "ORC-WFDEI-ref", the LC map of Year 1992 was used for the whole simulation. The two other simulations called "ORC-CRU-lcc" and "ORC-CRU-ref" use the annually varying and the 1992 CCI-LC maps, respectively, but they are forced with the CRU-NCEP atmospheric dataset.

The ORCHIDEE model version used for all these simulations is the new CMIP6 version which benefit from many recent developments of the IPSL team. For example, a new snow and soil freezing scheme allowing to better represent the high latitude processes, optimized values for the albedo and a calibration of the function controlling the impact of water stress on evapotranspiration/photosynthesis were implemented.

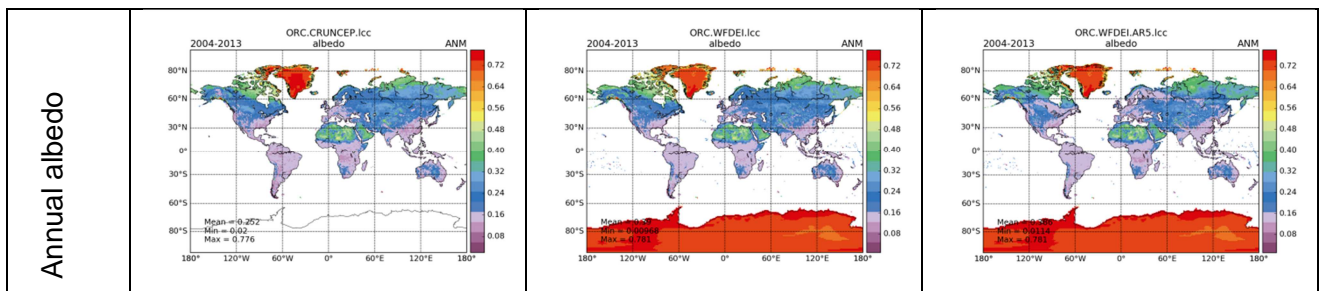
2.3.2 Analysis of LC versus meteorological forcing impacts

The five ORCHIDEE simulations described previously (section 2.3.1) have been analyzed to assess the contribution of the new CCI-LC maps. In this section, we focus on the comparison of the 2 LC products (CCI and CMIP5) and on the impact of the atmospheric forcing. The contribution of the annual LC maps compared to a static product will be discussed in the joint section where the 2 land surface model (ORCHIDEE and JSBACH) are compared (Section 5).

Therefore, the comparison was done for the 3 ORCHIDEE simulations (CRU-CCI, WFDEI-CCI and WFDEI-CMIP5) on the energy, carbon and water budgets terms at the global scale but also regionally in few particular regions where we identified differences between the 2 LC products, e.g., Australia and boreal regions as we will present below.

3.1.2.3. Global analysis

The surface energy variables are plotted at the global scale, in Figure 8. At first glance, we can see that the spatial patterns are very similar in the 3 simulations with evident larger differences due to the atmospheric forcing compared to the LC mapping. This result highlights the key role of precipitation (which is the variable which presents the largest discrepancies in the two atmospheric forcing) on the surface processes. A more careful comparison of the 2 simulations using the same forcing but different PFT maps, show clearly some differences linked to PFT mapping. For example, we note i) higher albedo values in boreal regions explained by the larger fraction of bare soils in the CCI product, ii) lower values of latent heat flux in the arid (Arabia, Australia) and boreal regions presenting a larger fraction of bare soil and in Sahel and Europe where the fraction of forested areas is lower in the CCI PFT map. We can see also that these changes have very little impacts on the average surface temperature, which is mainly driven (at these temporal scales) by the air temperature (forcing variable) identical in these two simulations.



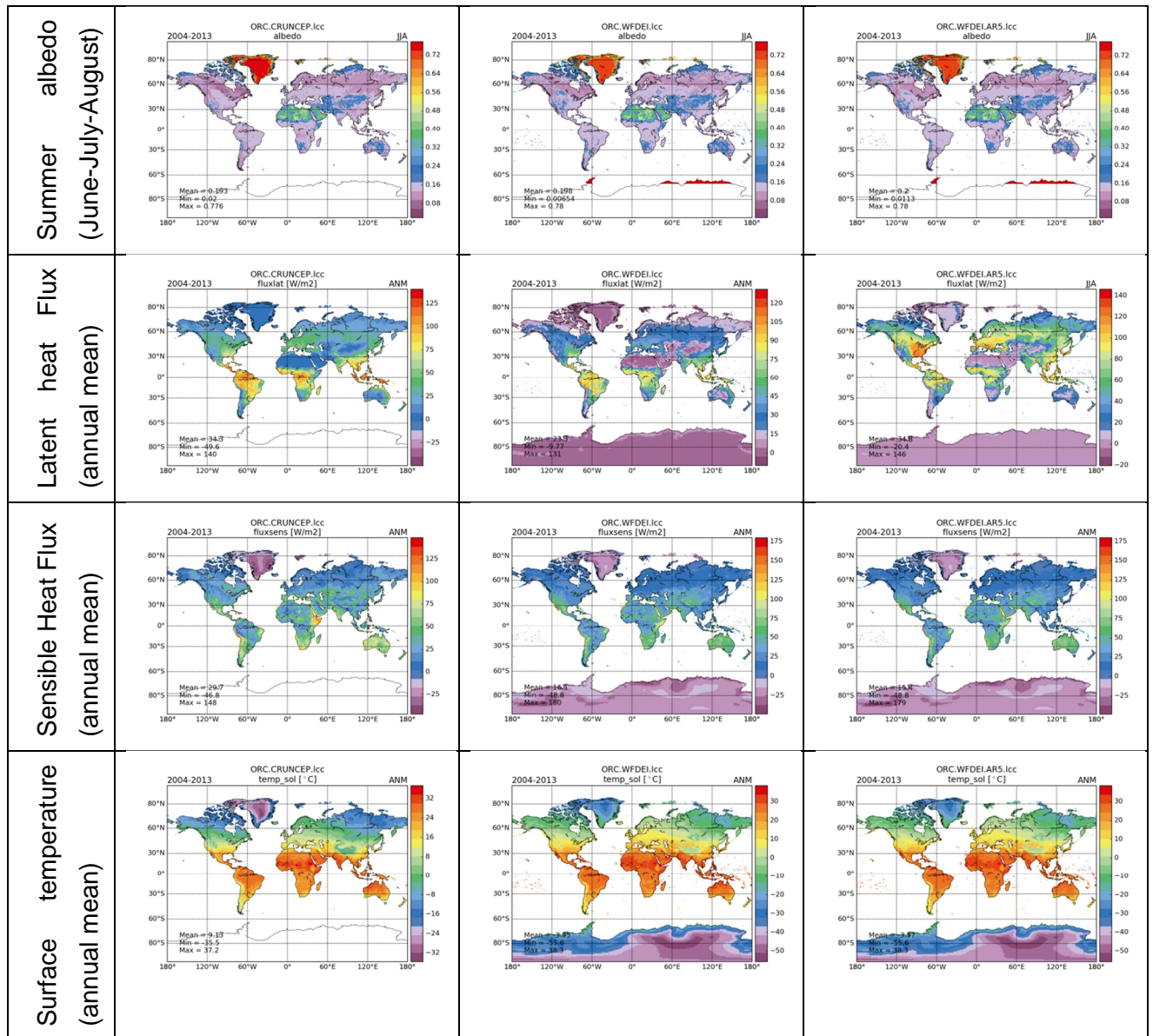


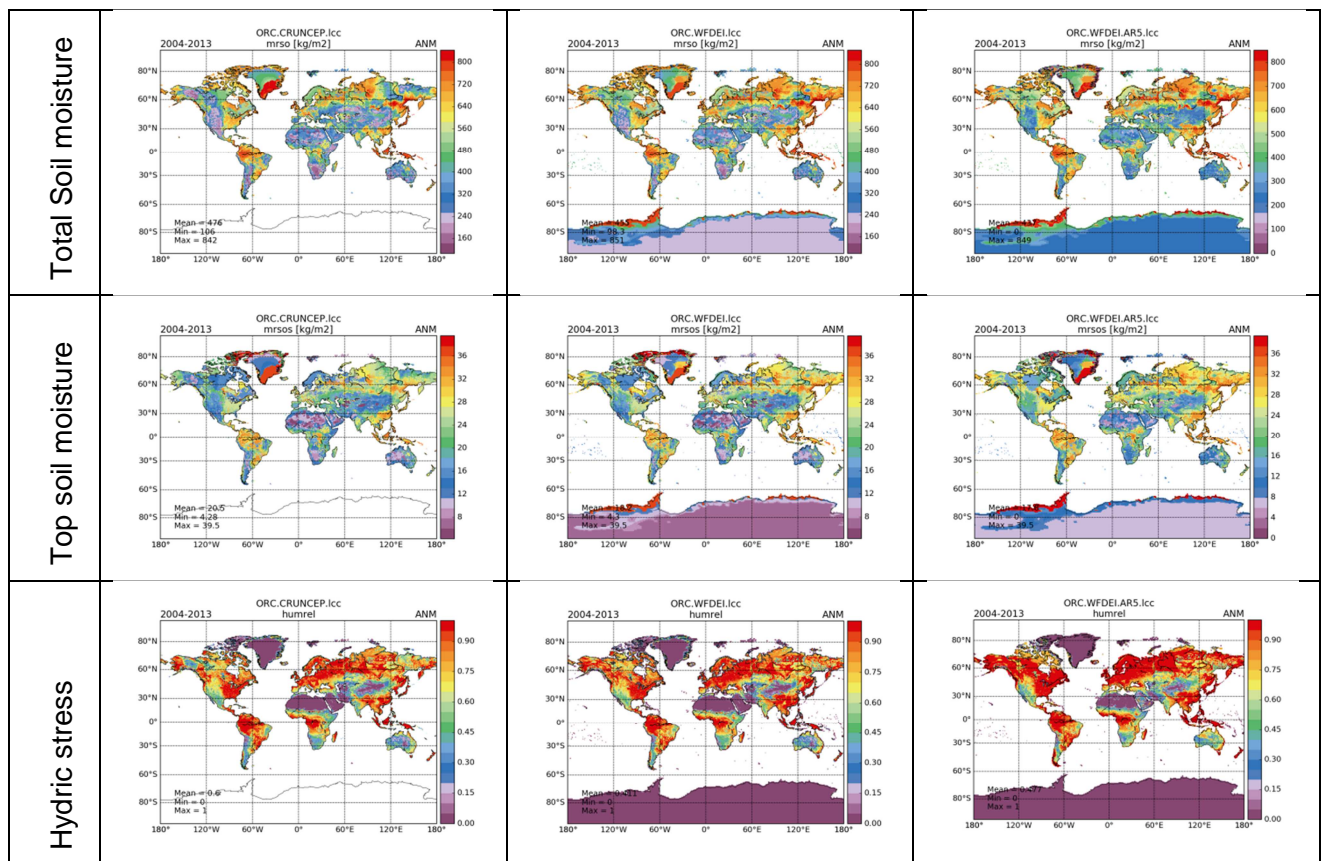
Figure 8: Comparison of some of the energy budget terms (albedo, latent and sensible heat fluxes and surface temperature) simulated by ORCHIDEE with CRU-NCEP (left column), WFDEI-GPCC (middle), both with the CCI-LC-PFT map and WFDEI-GPCC and the old CMIP5 PFT map (right column).

The water budgets terms displayed in Figure 9 as annual means, concern the total soil moisture (average across the 2m soil depth), the surface soil moisture (averaged on the first 10cms), the hydric stress for transpiration which is estimated by convolution of the soil water content and the vegetation root profiles, and the main two terms of the evapotranspiration which are the soil evaporation and the transpiration. It should be recalled that the ORCHIDEE stress factor is in fact a "no-stress" factor, being equal to 1 when the vegetation is completely fed by water, i.e., when the atmospheric demand is fully supported.

These plots show also that the main differences arise between the CRU and the WFDEI forcing but the two PFT maps also lead to significant differences in the soil water budget. For example, we

note dryer soils in Western North America in relation with higher water stress (lower values of the stress factor). We can see also that the surface soil moisture presents larger differences compared to the total one, highlighting that the type of vegetation influences the vertical distribution of the water in the soil. In the regions where the bare soil fraction is larger in the CCI map, the top soil moisture is lower (e.g., in the eastern and western part of the US and in Australia) because of a larger contribution of surface evaporation compared to transpiration. These features are also visible in the boreal regions presenting the same PFT changes.

The comparison of the 2 simulations with the same PFT map and different atmospheric forcing do not show the same results: the total and top soil moisture shows the same spatial variability because the forcing (at the global scale) present the same patterns even though the total amounts are different. This comparison highlights here the role of the land cover on the soil water vertical distribution and the partition of the different terms of the evapotranspiration. As an example, Figure 10 highlights the impact of the PFT distribution on summer transpiration in the northern latitudes. The lower fractions of forests in Europe in the CCI maps, associated to an increase of crops and grasslands, as well as the increase of bare soil in the northern latitudes lead to lower transpiration.



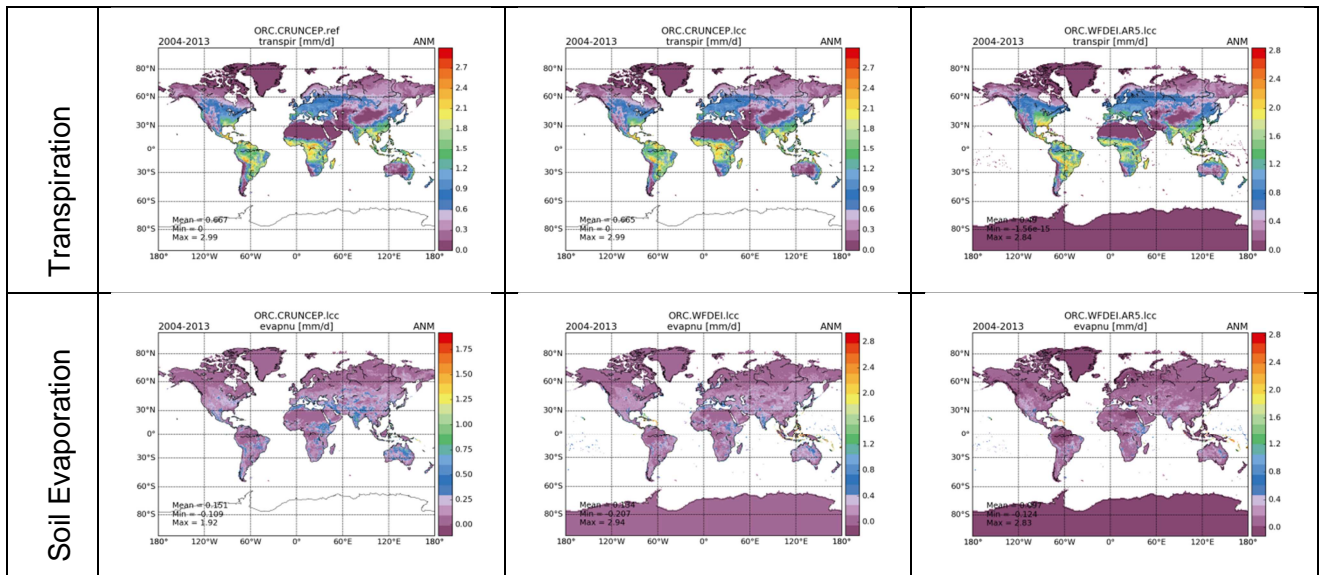


Figure 9: Comparison of some of the water budget terms (total and top (first 10 cms) soil moisture, hydric stress for transpiration, soil evaporation, transpiration) simulated by ORCHIDEE with CRU-NCEP (left column), WFDEI-GPCC (middle), both with the CCI-LC-PFT map and WFDEI-GPCC and the old CMIP5 PFT map (right column).

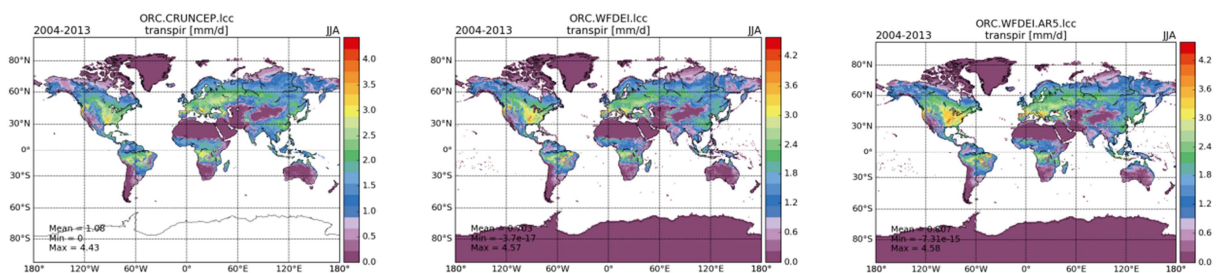


Figure 10: Highlight on summer transpiration, simulated by ORCHIDEE with CRU-NCEP (left column), WFDEI-GPCC (middle), both with the CCI-LC-PFT map and WFDEI-GPCC and the old CMIP5 PFT map (right column).

The variations of the evapotranspiration induced by the LC map changes impacted the other components of the surface water budget like drainage and runoff, which have slightly increased. The resulting river discharges are also as a consequence slightly higher. Figure 11 presents for the 14 largest river catchments of the world, the simulated discharges at the outlet of each basin. The observations as provided by the Global Research Data Center (GRDC database available at http://www.bafg.de/GRDC/EN/Home/homepage_node.html) are plotted at the monthly time scale. The results show larger stream flows in the river basins of the temperate and boreal regions and no significant impacts elsewhere. These variations are generally leading to larger discrepancies with the observations but we have seen in other studies that for these river basins, the flows are strongly dependent on the precipitation forcing especially on the snowfall/rainfall partition, and that the WFDEI-GPCC dataset presents some deficiencies for this variable. The use of other forcing like GSWP3 (Yoshimura and Kanamitsu, 2008) in which this ratio was more rigorously determined, allowed to simulate flows closer to the observed ones (Guimberteau et al., 2017). We expect therefore different conclusions with a more accurate precipitation forcing.

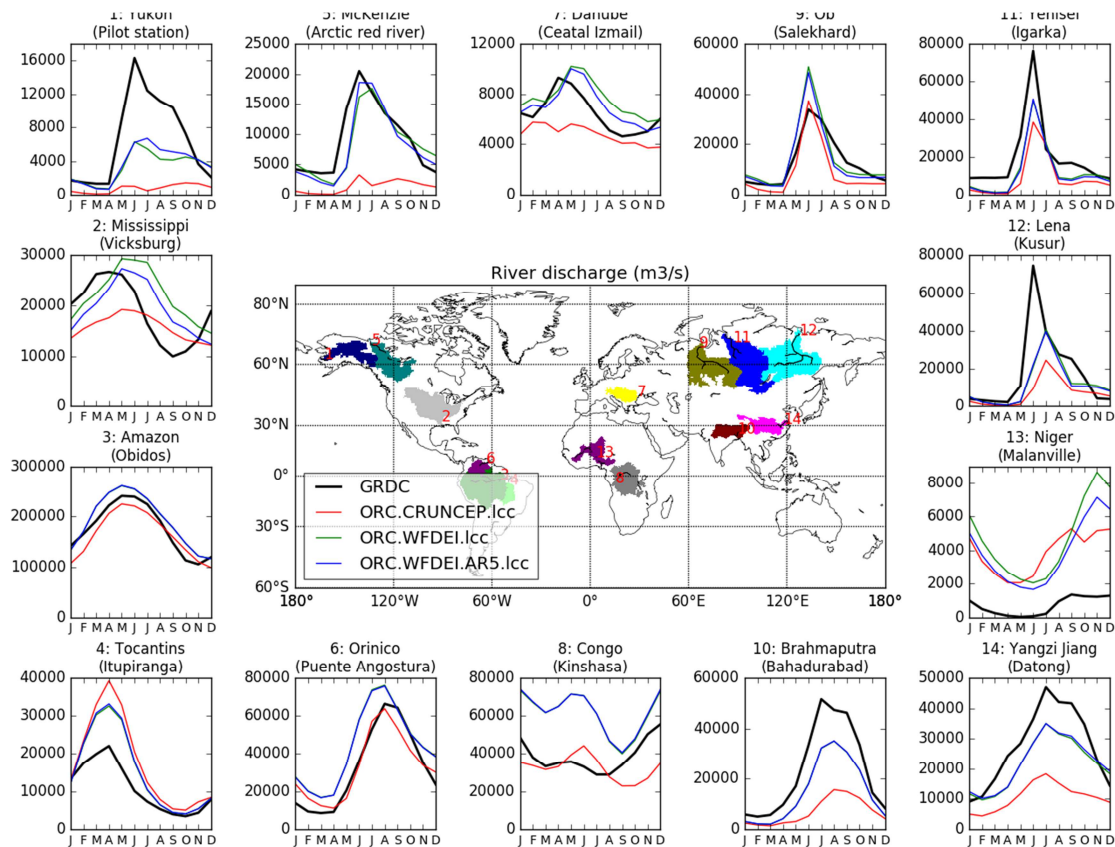
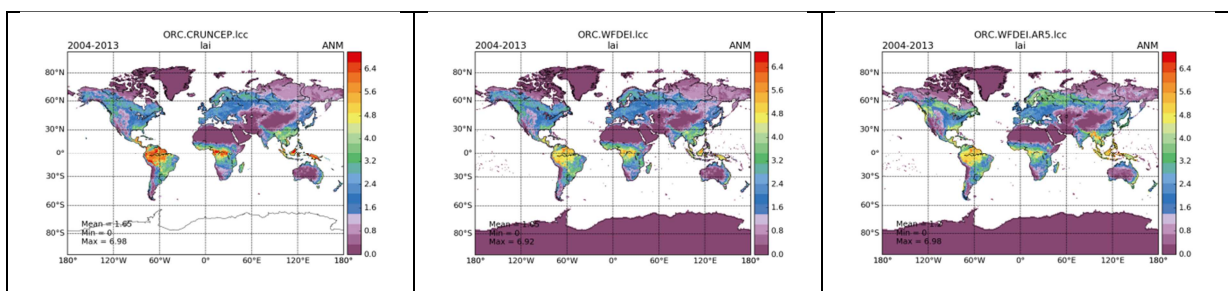


Figure 11: Monthly mean seasonal river discharge ($m^3 s^{-1}$) simulated with the two forcings (CRU-NCEP and WFDEI) and the two LC maps (CMIP5 and CCI-LCC) compared to observed non-naturalized (GRDC) averaged over the period 2004-2013.

If we consider now the carbon budget, we can see in Figure 12, that the PFT distribution has more impact on the spatial variability of the carbon budget in terms of photosynthesis (GPP) and LAI simulation than the atmospheric forcing (which impacts significantly the magnitude of these two variables), as expected. The simulated GPP and LAI values are in line with the PFT parameters prescribed in ORCHIDEE, i.e., lower values in the northern latitudes because of the larger fractions of bare soils and lower fractions of evergreen forests, especially in the north of Canada and Siberia.

All these plots as well as the diagnostics for other carbon/water/energy cycle variables are displayed under the web-site: https://orchidas.lscce.ipsl.fr/dev/LCCCI_orcsims.php



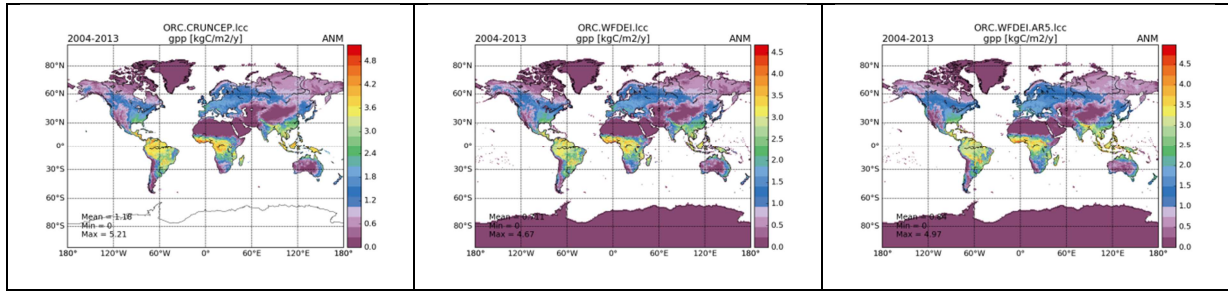


Figure 12: Comparison of some of the carbon budget terms (LAI and GPP) simulated by ORCHIDEE with CRU-NCEP (left column), WFDEI-GPCC (middle), both with the CCI-LC-PFT map and WFDEI-GPCC and the old CMIP5 PFT map (right column).

3.1.2.4. Regional analysis

To better assess the impact of the PFT mapping on the surface water, carbon and energy fluxes and the direction of the impacts compared to evaluation products, we focused on various regions of the globe where we identified changes and looked at the time series of the different components of the surface budgets. We present here only a zoom on south-western Australia (see Figure 13) where we noticed previously large PFT differences between the CCI and the CMIP5 maps, especially a decrease of grasslands in the CCI product at the benefit of bare soils. The time series (mean seasonal cycle over the simulation period) are plotted in Figure 14, along with reference products such as the GIMMS LAI product (Zhu et al., 2013) and the Jung et al., (2009) GPP product. These two reference products are used routinely as benchmark for the evaluation of land surface models.

In Figure 14 we see clearly how the PFT changes affect the albedo, soil moisture and surface fluxes. The larger fraction of bare soil lead to higher values for the albedo in the simulations using the CCI PFT maps by about 10%, lower latent heat flux and GPP which are now in better agreement with the observations. Soil water content is consequently larger and the simulated LAI values become lower also in better agreement with the satellite GIMMS observations, even though the seasonal cycle looks still too large. Overall, in this region, PFT changes seem to improve the simulations.

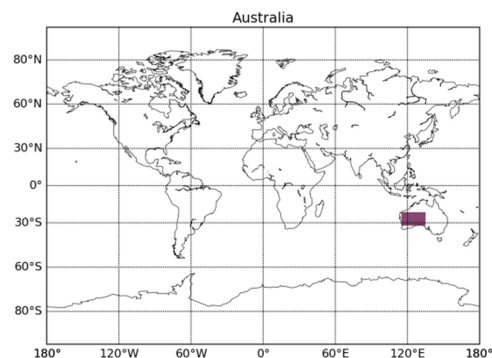


Figure 13: Region in Australia used for the following model analysis

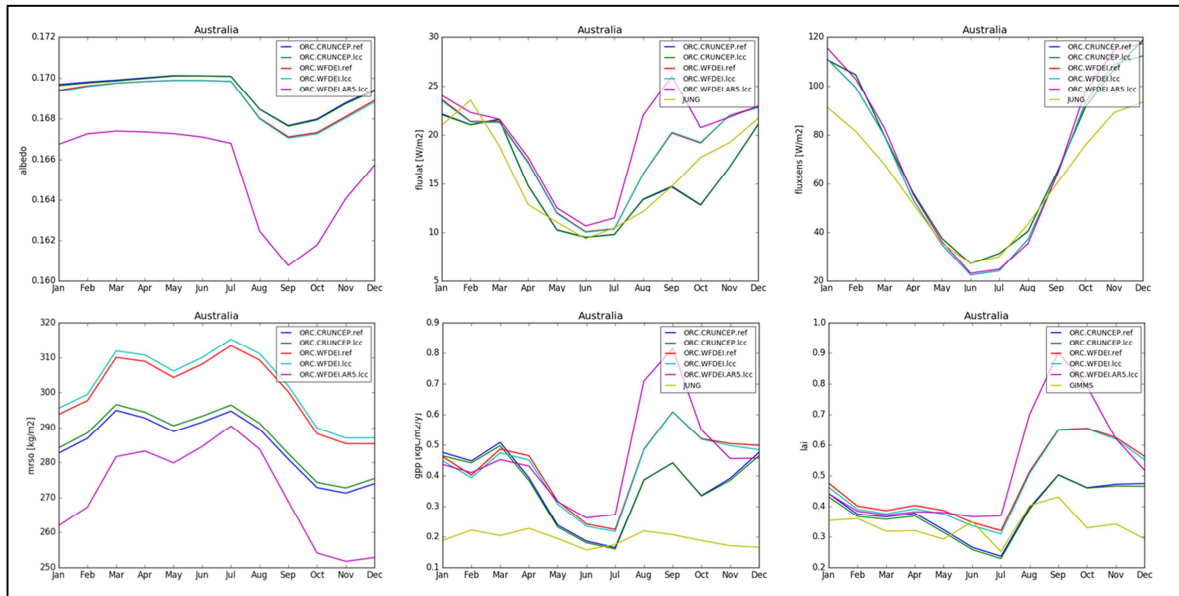


Figure 14: Highlight on South-western Australia: time series of the ORCHIDEE simulations with CRU-NCEP (blue line), WFDEI-GPCC (green), both with the CCI-LC-PFT map and WFDEI-GPCC and the old CMIP5 PFT map (purple). The reference of Jung et al., 2009 product for fluxes and of GIMMS (Zhu et al., 2013) for the LAI are plotted in brown color. The variables displayed are: Albedo, Latent and Sensible heat fluxes, total soil moisture, GPP, LAI.

These regional analysis are still under investigation and many more regional diagnostics can be found at: https://orchidas.lscce.ipsl.fr/dev/LCCCI_orcsims.php under the time series pages. Note that you can select different types of temporal average to view the mean seasonal cycle or the monthly/annual raw values. Although on average the flux/stocks differences induced by different land cover products or by the annual land cover changes (see section 5 for joint experiment) are smaller compared to differences induced by climate forcing, the results need further investigation at local/pixel scale. We also expect that with increasing model complexity the impacts of land cover mapping may increase.

	Ref	LC CCI Phase 2: Climate Assessment Report, Year 3		
	Issue	1.0	Date 2017-07-11	
	Page	29		

3 MPI-M: ASSESSMENT OF THE IMPACT OF THE NEW LAND COVER MAPS WITHIN THE MPI-ESM MODEL

Authors: **Goran Georgievski¹, Stefan Hagemann¹**

Contributors: **Stiig Wilkenskjeld¹, Giovanni Forzieri²**

¹Max Planck Institute for Meteorology, Hamburg, Germany

²European Commission Joint Research Centre, Ispra, Italy

3.1 Sensitivity of the MPI-ESM to the uncertainty in ESA-CCI Land Cover observation

3.1.1 Introduction

Uncertainty in the results of climate simulations is an inherent feature in climate modelling. Uncertainties may originate from various sources such as (1) natural climate variability; (2) each climate model uses different techniques to discretize physics and dynamics and to parameterize sub-grid effects and, hence, has different model errors, (3) uncertainty in the prescribed boundary conditions, e.g. of land surface characteristics at the land - atmosphere interface or greenhouse gas and aerosol concentrations, especially if future scenarios are considered. Parts of the latter two sources are related to the lack of empirical investigations or limitations of observational techniques. These uncertainties can lead to insufficient understanding of the climate processes and controversial interpretations of climate research (Curry (2011), IPCC (2014), and Maslin (2013)). Understanding them is crucial to determine the reliability of climate models to simulate present day climate as well as to determine the range of possible climate states in future projections. Therefore, it is of paramount importance to reduce uncertainty and to improve our understanding of processes that contribute to uncertainty in the climate model results. One of the key sources of uncertainty in numerical simulations of carbon, energy and momentum exchange between land and atmosphere is the uncertainty in the observed land surface properties. Land surface properties in climate models are either prescribed with static maps of vegetation or they can change in dynamic interaction with other components of climate models. In both cases, the initial vegetation distribution in the model is usually derived from remote sensing products supplemented with ground observations – global Land Cover (LC) maps. LC represents different properties of the Earth's surface and controls water and energy exchange, photosynthesis rates, nutrient levels and surface roughness at the land-atmosphere interface (Sellers et al, 1997). It is identified as one of the essential climate variables needed to understand changes in carbon cycle and climate change (Feddema et al, 2005). Numerous studies within the recent decade focused on the quantification of the impact of LC change on climate (see Mahmood et al (2014) and reference therein for a comprehensive review). There is a growing body of evidence that vegetation, especially tree cover, has an impact on terrestrial water cycle, energy balance and carbon cycle.

	Ref	LC CCI Phase 2: Climate Assessment Report, Year 3		
	Issue	1.0	Date 2017-07-11	
	Page	30		

However, understanding the impact of LC change on climate remains controversial and is still work in progress (e.g. for the effect of LC change on precipitation, the largest component of the terrestrial water cycle, see Bonan (2008), Ellison et al (2012), Mahmood et al (2014), Sheil and Murdiyarso (2009)). At the core of the controversy lies the uncertainty in the observation of climate parameters such as precipitation (see, e.g., Herold et al 2017), as well as in the remote sensing derived LC maps. Comparing several global LC maps, Congalton et al (2014) found that the main reasons for uncertainties and inconsistencies are due to (1) different data acquisition methods (i.e. missions and sensors); (2) the maps are produced by different methodologies; and (3) they used different classification schemes. All these factors contributed to the estimate that the total accuracy of the LC maps is below 70%.

The impact of LC uncertainties on terrestrial carbon fluxes has been investigated by Quaife et al (2008). They found that the main uncertainty in carbon flux calculations is due to (1) incorrect conversion of LC classes to Plant Functional Types (PFTs), which are commonly used as another vegetation classification system in climate and land surface models; (2) information loss due to aggregation of high resolution LC data to coarser resolution used in numerical models; (3) accuracy of the LC map, i.e. difficulty in discriminating some vegetation types from satellite data. These uncertainties resulted in a 254 gC/(m² y) range of uncertainty for gross primary production (GPP) averaged over Great Britain. Vegetation GPP is also the largest source of terrestrial CO₂ and, hence, the vegetation distribution comprises the largest source of uncertainty in GPP estimates. In particular due to the overestimated coverage rate (area fraction of the grid) of forests in global eco-system datasets, the forest gross carbon dioxide uptake globally as well overestimated with a value of 5.12 ± 0.23 Pg C yr⁻¹ according to Ma et al (2015). Evaluating components of the global carbon cycle by the CMIP5 models, Anav et al (2013) reported a general overestimation of photosynthesis and leaf area index and, therefore, an overestimated terrestrial carbon uptake for most of the models. Le Quere et al (2016) in their annual report of the global carbon budget for the last decade (2006-2015) estimated an annual uncertainty due to land use change in carbon emission of about ±0.5 PgC/year, while the uncertainty of terrestrial carbon uptake is ±0.9 PgC/year.

Despite of a clear impact of LC change, including but not limited to urbanization, adoption of agriculture, irrigation, deforestation and afforestation, very little research has been done to investigate the range of uncertainty in observed LC and its impact on the near surface climate. Recently, Hartley et al (2017) have investigated the range of uncertainty of a recently published satellite-derived LC map and its impact on the sensitivity of energy balance, hydrological and carbon cycle with three land surface models (LSM). According to their definition of uncertainty, they found that the maximum plausible range of LC uncertainty is about the same order of magnitude, or even larger than the range of the recent historical LC change. Therefore, the impact on LSM state variables due to the uncertainty is about the same order of magnitude as the impact of LC change. In this study, the impact of LC uncertainty on the near surface climate is investigated with the Earth System Model of the Max Planck Institute for Meteorology (MPI-ESM) using prescribed sea surface temperature and sea-ice. In order to estimate this impact, the range of LC uncertainty is considered and sensitivity of various climate components is examined that include the terrestrial water cycle (precipitation and evapotranspiration), energy cycle (albedo and 2m temperatures), circulation (wind and pressure) patterns, and GPP.

3.1.2 Data and Methods

Earth System Models (ESMs) are tools to study complex interaction between major components of the climate system (i.e. atmosphere, hydrosphere, cryosphere, biosphere, and land surface) driven

	Ref	LC CCI Phase 2: Climate Assessment Report, Year 3		
	Issue	1.0	Date 2017-07-11	
	Page	31		

by solar radiation (see Flato 2011 for a comprehensive overview of ESMs). The aim of ESMs is to simulate the climate state of our world by solving equations representing physical and bio-geo-chemical processes in the discrete numerical space. To solve these equations various datasets representing initial and boundary conditions are needed. One such dataset representing conditions of the Earth's surface, a new global land cover (LC) has been recently published in the frame of the European Space Agency (ESA) Climate Change Initiative (CCI). The dataset is described in the project documentation and its application for LSMs modelling is described by Hartley et al (2017). The conversion of LC into PFTs used in climate models is described in Poulter et al (2011, 2015). The estimate of the maximum plausible uncertainty range of LC observation is described by Hartley et al (2017) and briefly summarized in section 0 and 0 with an emphasis on the application with MPI-ESM. In section 0, the land surface component – JSBACH3.1, and the atmospheric component – ECHAM6.3 of MPI-ESM1.2 are briefly described. In the section 0 conversion of LC into PFTs, particular for JSBACH is described.

3.1.2.1. ESA-CCI Land Cover Data

The ESA-CCI-LC product is derived combining remotely sensed surface reflectance and ground-truth observations at 300 m resolution. The map examined in this study is the LC map for the epoch 2010, which is an average LC map based on the satellite data acquisition during the period 2008-2012. For each grid-box at 300 m resolution, an estimate of confidence that the LC class is identified correctly is provided. This confidence can be also interpreted as a source of uncertainty (see Hartley et al (2017) for details). The LC product complies with the United Nations Land Cover Classification Scheme (UNLCCS) and it is not directly suitable for climate modelling. Therefore, ESA-CCI-LC categorical classes need to be converted to model specific vegetation types. The vegetation distribution in ESMs is commonly described by plant functional types (PFT) which is the classification system used to simplify the vegetation representation and group them according to their biophysical characteristics. The method of LC classes' conversion into PFTs is also called "cross-walking" (CW) procedure and it is described in section 0.

3.1.2.2. MPI-ESM

MPI-ESM couples the atmospheric, ocean and land surface processes through the exchange of energy, momentum, water, carbon and other trace gasses. In this study, the atmosphere and land components of MPI-ESM 1.2 are utilized that consist of the atmospheric general circulation model GCM ECHAM6.3 (Stevens et al., 2013) and its land surface scheme JSBACH 3.1 (Raddatz et al., 2007, Brovkin et al., 2009). Both models have undergone several further developments since the version (ECHAM6.1/JSBACH 2.0) used for the Coupled Model Intercomparison Project 5 (CMIP5; Taylor et al., 2012). Several bug fixes in the ECHAM physical parameterizations led to energy conservation in the total parameterized physics and a re-calibration of the cloud processes resulted in a medium range climate sensitivity of about 3 K. JSBACH 3.1 comprises several bug fixes, a new soil carbon model (Goll et al., 2015) and a five layer soil hydrology scheme (Hagemann and Stacke, 2015) replaced the previous bucket scheme. These five layers correspond directly to the structure used for soil temperatures and they are defined with increasing thickness (0.065, 0.254, 0.913, 2.902, and 5.7 m) down to a lower boundary at almost 10 m depth. Vegetation is represented by several PFTs in each model grid cell using a tiling approach. Here, the bare soil area fraction of a grid cell is defined implicitly as a residuum from all vegetation cover fractions, i.e. $1 - \text{sum of area fractions of all vegetation types}$. Various aspects of vegetation dynamics are simulated on a broad range of temporal scales, including photosynthesis / stomatal conductance, leaf phenology, carbon allocation and decomposition, nitrogen cycling, and the redistribution of PFTs and deserts (Brovkin et al., 2009).

	Ref	LC CCI Phase 2: Climate Assessment Report, Year 3		
	Issue	1.0	Date 2017-07-11	
	Page	32		

Five ECHAM6.3/JSBACH simulations were conducted at T63 horizontal resolution (about 1.85° or 200 km) with 47 vertical layers in the atmosphere. They were forced by observed sea surface temperature (SST) and sea ice from the AMIP2 (Atmospheric Model Intercomparison Project 2) dataset during 1979-2009 (Taylor et al., 2000). 1979 is regarded as spin-up, so that only the period 1980-2009 is considered for the analyses. Five simulations have been performed with five different PFT maps as prescribed in Hartley et al (2017). Note that Hartley et al. (2017) performed their offline-experiments at 2° resolution, which slightly differs from the T63 spectral resolution utilized in the present study. The creation of maps is described in the section.

3.1.2.3. Cross-walking procedure

In the frame of the ESA-CCI-LC project, an user tool and CW table were released to support the conversion of LC classes into PFTs. However, due to the different design and processes implemented in various climate models, differences occur in the treatment of artificial, water bodies, ice, bare or vegetated surfaces. Therefore, expert knowledge and additional datasets are needed to take into account associated climate model processes and the required input information for their computations. In particular, for the vegetation delineation due to climate zones and photosynthetic pathways, auxiliary datasets are needed to adapt ESA-CCI-LC for the use in climate models. For that purpose, an updated world map of the Köppen-Geiger (KG) climate classification adopted from Peel et al (2007) is used. The photosynthetic pathway, i.e. the C4 vegetation percentage, is taken from International Satellite Land Surface Climatology Project (ISLSCP) Initiative II (Still et al 2009) data. The rules for conversion are adopted from Poulter et al (2011) as follows: KG classes 1, 2, 3, 4, 6 are tropical, 5 and 7-28 are extra-tropical classes. The polar classes 29 and 30 are not used here. Abundant vegetation is defined as C4 where photosynthetic pathways are larger than 50%, and as C3 elsewhere. The JSBACH land surface scheme can be set to distinguish various numbers of PFTs. However, in this study 12 vegetation types are defined that were also used in CMIP5: tropical evergreen tree (TrET), tropical deciduous tree (TrDT), extra-tropical evergreen tree (ExET), extra-tropical deciduous tree (ExDT), raingreen shrub (RgSh), deciduous shrub (DeSh), C3 grass (C3Gr), C4 grass (C4Gr), C3 pasture (C3Pa), C4 pasture (C4Pa), C3 crop (C3Cr), C4 crop (C4Cr). Shrubs distributions derived from ESA-CCI-LC seem to largely differ from the PFT distribution used in CMIP5 studies (figure not shown here). However, this type of uncertainty depending on how many types of vegetation are present in the model is rather out of the scope of this paper and will be a subject of another study. Here, an attempt is made to adopt ESA-CCI-LC to the JSBACH PFTs as derived for the purpose of CMIP5 simulations. Figure 15 shows PFT distributions aggregated into major vegetation types used in JSBACH derived from ESA-CCI-LC.

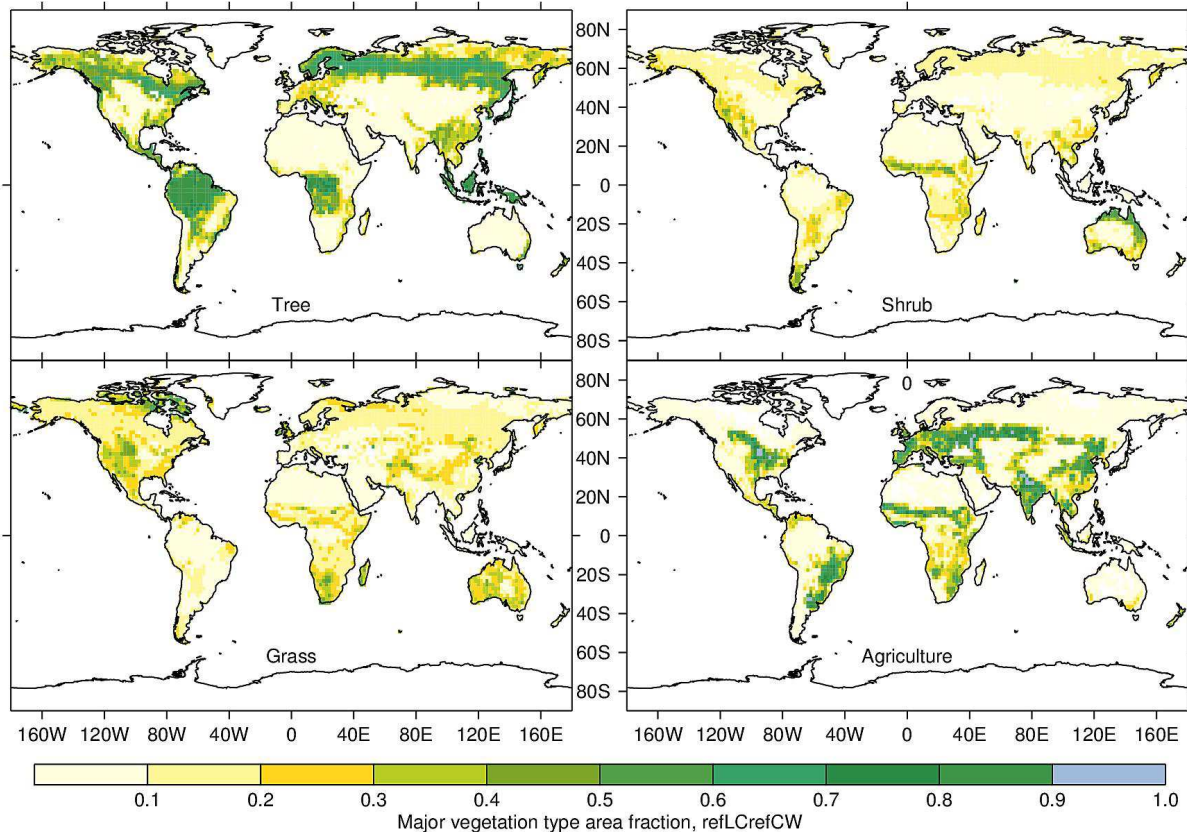


Figure 15: Area fraction of major vegetation types in JSBACH derived from ESA-CCI LC. Tree consists of tropical and extra-tropical evergreen trees, and tropical and extra-tropical deciduous trees. Shrub comprises deciduous and raingreen phenotypes. Grasses are diversified according to their photosynthetic pathways. There are C3 and C4 grasses according to that criterion. Agriculture includes crops and pasture, which are also divided into C3 and C4 depending on their photosynthesis processes.

3.1.3. Results

The focus here is on two sources of uncertainty: (i) algorithm (described in ESA-CCI-LC project documentation) of converting surface reflectance into LC classes (LC mapping), and (ii) CW procedure into PFT. The range of uncertainties will be quantified and it will be investigated how they propagate into land surface parametrization scheme and make an impact on sensitivity of climate simulations. Another major source of uncertainty depends on model design and processes implemented in climate models and therefore PFTs present in the model. This type of uncertainty and its impact on MPI climate models will be subject of another study.

Hartley et al (2017) demonstrated that prescribed vegetation distribution in models is a key source of uncertainty that is comparable to the spread between models for key model state variables indicators of energy, water and carbon cycle. Here, this analysis is expanded on AMIP type (prescribed SST and sea-ice) climate simulations with MPI-ESM. Detailed analysis of the range of uncertainty in ESA-CCI-LC maps is described in Hartley et al (2017). This section comprises two subsections with the focus on PFT uncertainty used in JSBACH and its impact on near surface climate simulated by MPI-ESM.

3.1.3.1. The range of PFT uncertainty

The maps and experiments are listed in Table 1 and their nomenclature is inherited from the study by Hartley et al (2017) and kept here for consistency.

Table 1: Experiment names and description

Experiment	Amount of vegetation used in experiment
minLCminCW	Vegetation is minimized with respect to LC mapping and CW procedure.
minLCrefCW	Vegetation is minimized with respect to LC mapping only.
mefLCrefCW	Reference vegetation from ESA-CCI LC epoch 2010 (see Sect. 2.1)
maxLCrefCW	Vegetation is maximized with respect to LC mapping only.
maxLCmaxCW	Vegetation is maximized with respect to LC mapping and CW procedure.

Figure 16 shows the amount of area covered with various JSBACH vegetation types and permanent ice. Table 2 sums the amount of the area covered with major vegetation types, units are Mha. Comparing these areas with the area of historical LC change estimated in the literature, it turns out that the range of uncertainty is about the same order of magnitude as the historical LC change. Ramankutty and Foley (1999) estimated that approximately 1200 Mha of trees have been removed globally since 1700 up to 1992. In the simulations that minimise vegetation cover, there is 721 Mha (minLC_refCW) and 1740 Mha (minLC_minCW) less trees than in the reference experiment (refLC_refCW). In the simulations that maximise vegetation there is 633 Mha (maxLC_refCW) and 1229 Mha (maxLC_maxCW) more trees than in the reference simulation. According to ESA-CCI-LC data for epoch 2010 used as reference LC, the area currently under farming is 2365 Mha, while Ramankutty and Foley (1999) estimated that there was 1800 Mha under farming in the year 1992.

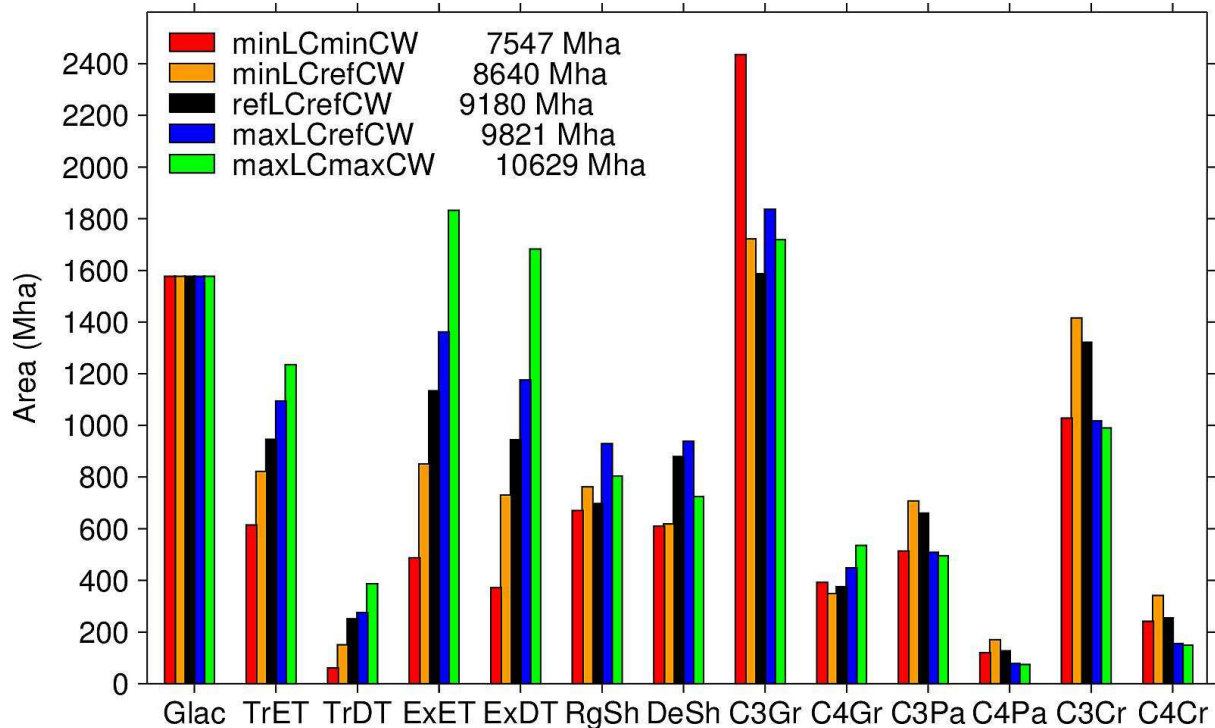


Figure 16: Area of PFT coverage in JSBACH for various experiments. The abbreviations are as follows: Glac – permanent ice, TrET – Tropical Evergreen Tree, TrDT – Tropical Deciduous Tree, ExET – Extra-Tropical Evergreen Tree, ExDT – Extra-Tropical Deciduous Tree, RgSh – Raingreen Shrub, DeSh – Deciduous Shrub, C3Gr – C3 Grass, C4Gr – C4 Grass, C3Pa – C3 Pasture, C4Pa – C4 Pasture, C3Cr – C3 Crop, C4Cr – C4 Crop

Here is also interesting to note non-uniform distribution of farming area in our experiments, so that minLC_refCW simulation has the largest farming area 2635 Mha, while maxLC_minCW has the smallest farming area (1709 Mha). Figure 17 identifies regions where the changes in JSBACH PFT distribution occur due to the uncertainty in LC mapping algorithm (minLCrefCW and maxLCrefCW) and CW procedure (minLCminCW and maxLCmaxCW) as defined by Hartley et al (2017). As already noted by Hartley et al (2017), these changes are stronger pronounced for CW uncertainty than for LC mapping uncertainty. The largest changes in geospatial distribution of PFTs occur in Northern North America and Canada, Scandinavia, Northern Russia (from Baltic to Ural) and Southeastern China for extra-tropical evergreen trees. For the extra-tropical deciduous trees, the largest changes due to uncertainty are located in Northern Russia ranging from the West Siberian Plain to the Bering Strait, in Zambezi river basin and in the South American Pampas. The most notable changes in the distribution of tropical trees are in Amazon and Congo River basins. Other notable changes appear for shrubs and herbaceous types. For example, maxLC_maxCW is characterised by the decrease in shrubs from approximately 40N to 70N latitude, as well as along the north-western border of Parana River basin in South America and in the area between the Indochina peninsula and the Yangtze River basin. This experiment is also characterised by the increase of shrubs especially along the southern and eastern coast of Australia and in some parts of Sub-Saharan Africa (see green line for Shrub in Figure 17). The global increase in the area of grasses, in particular of the C3 type, characterises all experiments. However, the most notable increase is for minLC_minCW that minimise vegetation due to CW uncertainty (see Table 2 and red line for Grass in Figure 17). The most dramatic changes in farming are in Sub-Saharan area,

between 10N and 50N of Eurasian continent, along the eastern coast of South America, in Central America and to the north of Gulf of Mexico. Crops have a productivity comparable to trees but albedo and transpiration properties like grasses. Thus, changes in crops are expected to have a nonlinear feedback to the across the five experiments. Therefore, note that the largest increase in crops appears in minLCrefCW, in particular on the Southern hemisphere (cf. Agriculture panels in Figure 15 and Figure 17).

Table 2. Area covered with various major vegetation types in Mha. In brackets deviations from the reference setup (refLCrefCW) are given in percentage. Herb is the sum of Grass and Farm types. Farm includes pasture and crop types.

	minLCminC W	minLCrefC W	refLCrefC W	maxLCminC W	maxLCmaxC W
Tree	1535(-53)	2554(-22)	3275	3908(19)	5137(57)
Shrub	1280(-19)	1380(-12)	1576	1867(18)	1528(-3)
Herb	4732(9)	4706(9)	4328	4046(-7)	3963(-8)
Grass	2827(44)	2070(5)	1964	2286(16)	2254(15)
Farm	1904(-19)	2635(11)	2365	1760(-26)	1709(-28)

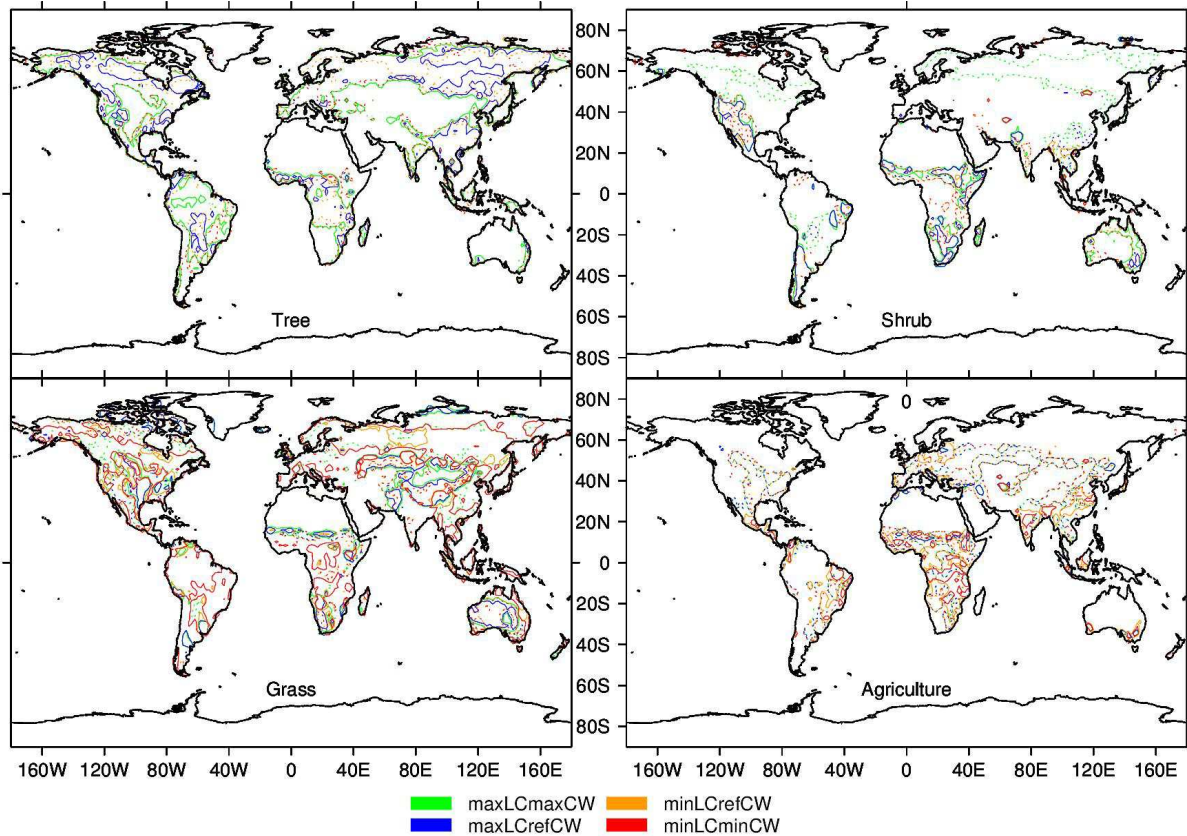


Figure 17: Area deviations from the reference (refLCrefCW) simulation of major vegetation types for the 4 uncertainty experiments. Contours are showing absolute area changes of 10%, dashed lines indicate negative values, full lines indicate positive values.

3.1.3.2. MPI-ESM sensitivity to the PFT uncertainty

The impact of the LC uncertainty and the range of the MPI-ESM response of annual mean climate are summarized in Figure 18 and table 3. Table 3 indicates that the range of climate response is about the same order of magnitude as the estimated climate change due to LC change due to land use. For example, changes in evapotranspiration are about the same order of magnitude (~2000 km³) as the estimated decrease in terrestrial evapotranspiration due to deforestation (~3500 km³, Sterling et al 2013). Figure 18 shows normalized scores for annual means of various climate variables for the 5 experiments conducted with MPI-ESM and JSBACH offline, where the latter were taken from Hartley et al. (2017). Similar as figure 6 in Hartley et al. (2017), the normalized scores for MPI-ESM simulations convey the same message as offline simulations. Albedo is the most impacted, equally affected by LC and CW uncertainty. It follows the law of negative linear regression i.e. with an increase in vegetation, albedo is decreasing. The differences in albedo between the JSBACH offline and MPI-ESM simulations are due to differences in the prescribed WFDEI precipitation and MPI-ESM computed precipitation which results in different snow cover in both types of simulations.

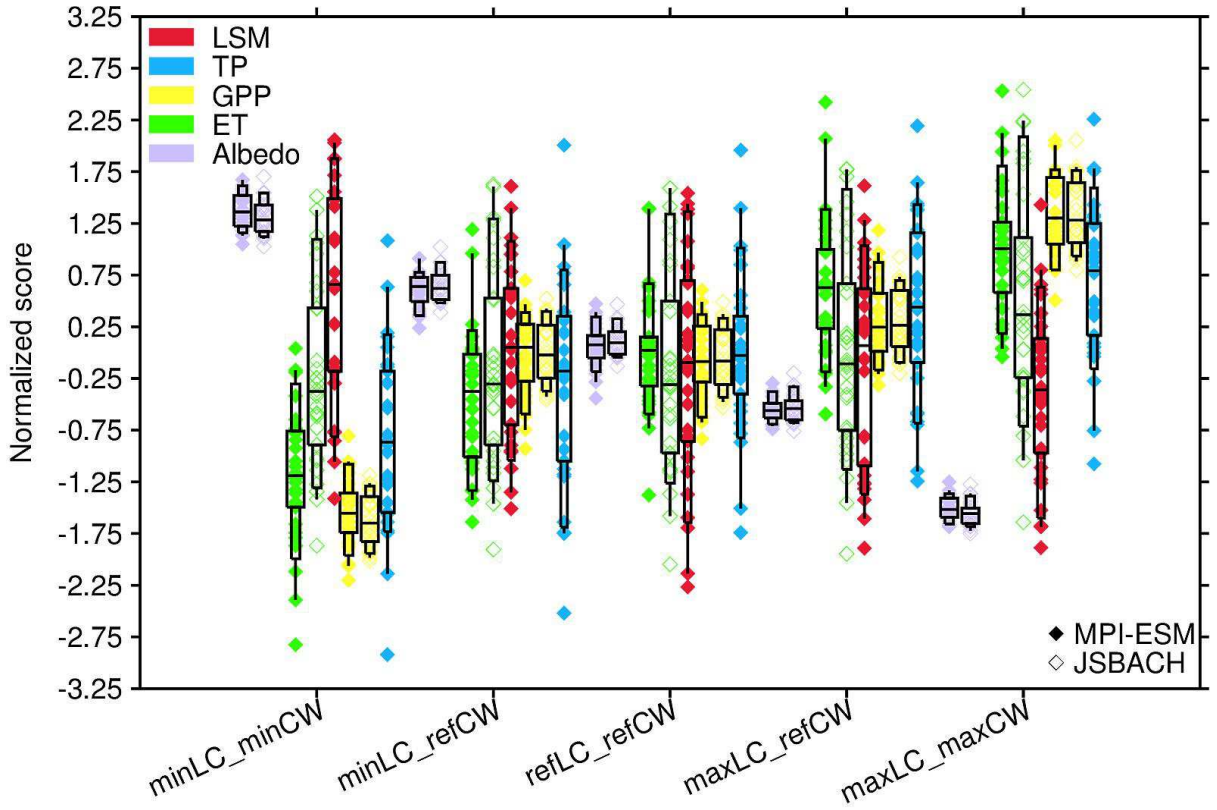


Figure 18: MPI-ESM and JSBACH response of annual mean climate variables over land to the PFT uncertainty expressed by normalized scores of annual means for GPP, ET, Albedo, and Total Precipitation (TP) and 2m temperature (T2M) for MPI-ESM (filled rhombi) and offline JSBACH simulations (empty style rhombi). Overlaid boxplot shows 0.05, 0.10, 0.25, 0.5, 0.75, 0.90 and 0.95 percentiles.

Table 3. Annual means for selected JSBACH and MPI-ESM variables over land for the period 1980-2009. Observations are taken from the following sources: albedo is calculated from GlobAlbedo (Muller (2013), He et al (2014)), GPP is taken from various sources in literature summarized in Anav et al (2015), review of ET estimates is provided by Zhang et al (2016), terrestrial precipitation is obtained from Trenberth et al (2007).

Variable	minLCminC W		minLCrefC W		refLCrefCW		maxLCminC W		maxLCmaxC W		Observations
	JSB	ESM	JSB	ESM	JSB	ESM	JSB	ESM	JSB	ESM	
Albedo (/)	0.304	0.298	0.299	0.291	0.294	0.287	0.289	0.282	0.280	0.274	0.248
GPP (PgC/yr)	135.9 17	134.9 90	156.4 18	152.0 24	155.6 77	151.4 09	160.2 40	1155.7 78	173.2 53	167.4 92	119-175
ET (10 ³ km ³)	60.04 3	72.74 8	60.12 8	74.20 5	60.09 6	75.07 8	60.26 8	76.290	60.74 0	77.01 7	65
Precipitation (10 ³ km ³)	-	103.9 25	-	105.6 15	-	106.6 36	-	107.94 3	-	108.7 38	107
2m temperature (°C)	-	9.931	-	9.838	-	9.842	-	9.882	-	9.855	8.5

The response of GPP to the PFT uncertainty is similar for both setups, except that MPI-ESM simulations show stronger inter-annual variability. In both cases, GPP is much stronger affected by the CW uncertainty than by the LC mapping uncertainty. This is probably because the biggest change in tree cover occurs for this uncertainty and trees are the largest primary producers. However, minimizing vegetation due to LC mapping uncertainty (minLC_refCW) shows a similar anomaly as in Hartley et al. (2017), i.e. it shows an increase of GPP with a reduction of vegetation. This is caused by the fact that although the global vegetation is decreased, the farming area characterised with high productivity is increased. The used version of JSBACH-offline does not show a sensitivity of ET to changes in PFTs, except some small increase in maxLC_maxCW case, which is likely related to a recently discovered bug in the JSBACH offline version. However, this

bug is not present in the coupled JSBACH version within MPI-ESM so that the ET behaviour is improved in the MPI-ESM simulations, which show a linear increase in ET with increase of vegetation. As total precipitation (TP) over land and 2m air temperature (T2M) over land are prescribed in the offline simulations, they are only available for the MPI-ESM simulations. Here, TP increases linearly with the increase of vegetation, while T2M does not show a systematic dependence on vegetation globally but rather regionally. Box plots overlaid over annual means scores provide an interesting insight in the distribution of frequencies and how climate depends on uncertainty in vegetation. For example, the amount of precipitation that is identified as the median year for minLC_minCW lies inside the 5th percentile for maxLC_maxCW, i.e. the amount of precipitation that appears to be a median value for the minLC_minCW experiment appears to be the amount of precipitation for a very dry year in maxLC_maxCW experiment. For ET, this difference is even more pronounced, leading to the conclusion that a median year for the very low vegetation (minLC_minCW) in respect of the annual terrestrial water balance (TP – ET) would be a dry year in the reference (refLC_refCW) simulation, and an extremely dry in maxLC_maxCW. Positive extremes show a similar behaviour. The median amount of precipitation for maxLC_maxCW lies above the 95th percentile of minLC_minCW, i.e. it has a similar amount of precipitation as the wettest year in minLC_minCW. This implies that PFT uncertainty should also have a considerable impact on large scale phenomena, such as NAO and ENSO, and their regional implications such as monsoons and weather regimes simulated by an ESM. In the study with offline LSMs, Hartley et al (2017) show that the most important impact of vegetation uncertainties is changes in albedo, e.g. more trees in high northern latitudes result in a lower albedo. In the present study, we are not only able to consider effects at the land surface, but we can also focus on atmospheric variables.

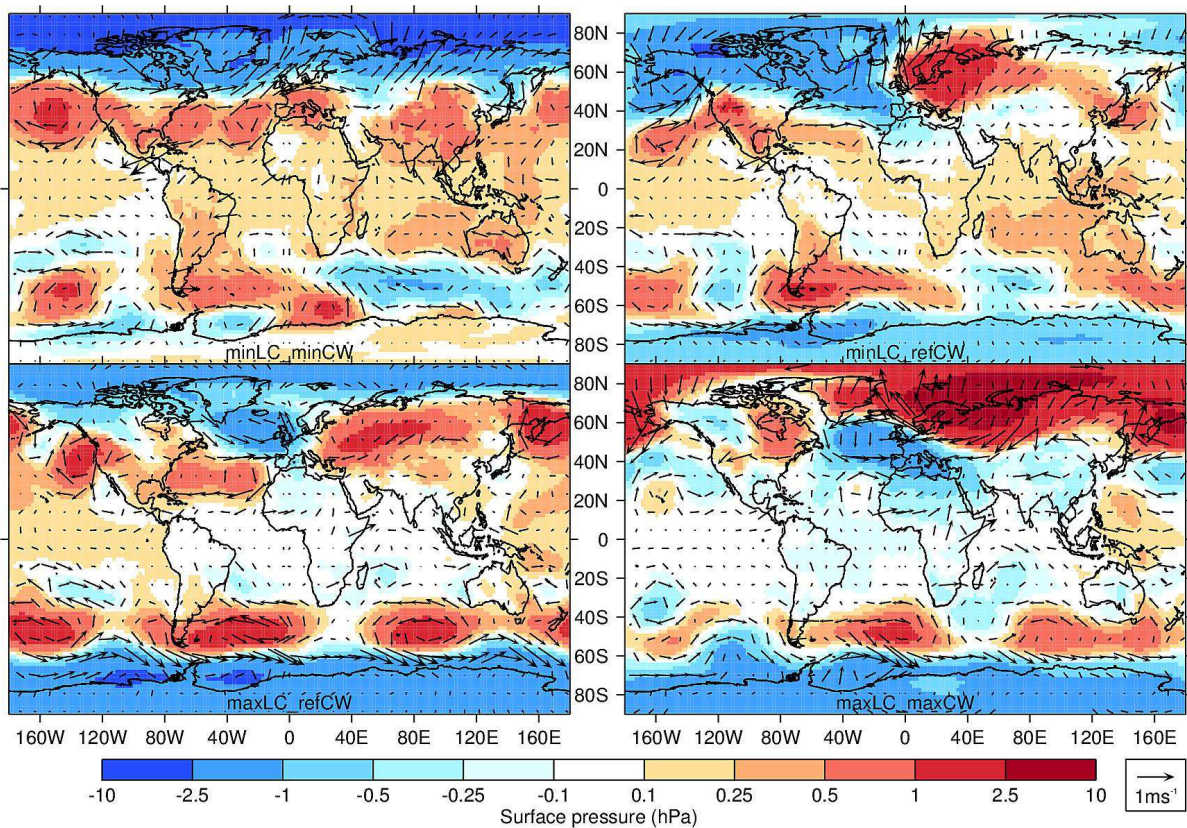


Figure 19: Boreal winter (DJF) mean sea level pressure and 10 m winds differences from reference simulation (refLCrefCW) for the 4 sensitivity experiments (minLCminCW, minLCrefCW, maxLCminCW and maxLCmaxCW).

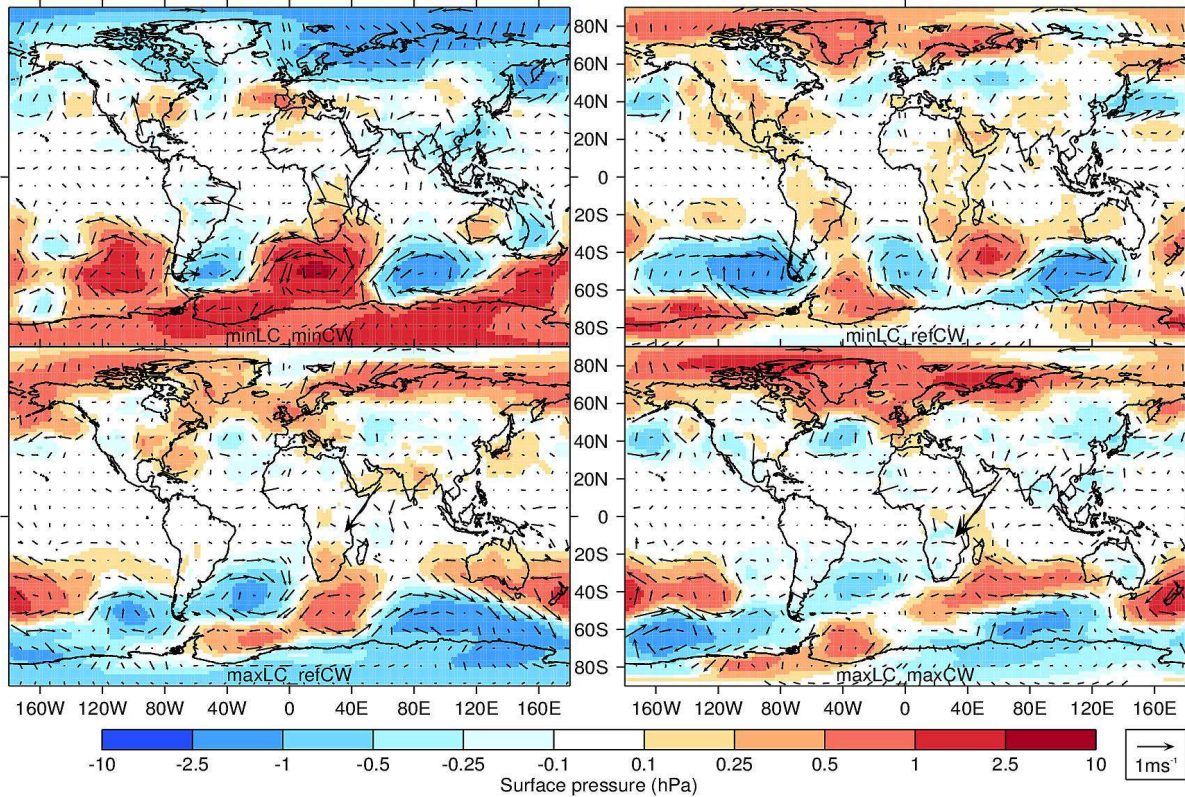


Figure 20: Boreal summer (JJA) mean sea level pressure and 10 m winds differences from reference simulation (refLCrefCW) for the 4 sensitivity experiments (see Table 1)

Figure 19 shows boreal winter (DJF) deviations of mean sea level pressure and 10 m winds for the uncertainty experiments from the reference. During the boreal winter (DJF), experiments that either minimise or maximise vegetation due to CW uncertainty (minLC_minCW and maxLC_maxCW) show a clear impact on westerlies. In the former, westerlies are strengthening while in the latter, they are weakening. Experiments that either minimize (minLC_refCW) or maximize (maxLC_refCW) vegetation due to LC uncertainty both contribute to the formation of blocking like feature, the former above the Atlantic Ocean to the north of the Great Britain, and the latter above the Central Europe. Both of them seem to have impact on increasing the Azores and Siberian high and deepening the Icelandic depression during the boreal winter. This results in intensified westerlies over the Atlantic Ocean. It is more pronounced by maxLC_refCW case. These changes in circulation pattern can be explained by an increase of surface roughness with an increase of vegetation. In addition, there are changes in the atmospheric water vapour distribution that impact the atmospheric pressure patterns and, hence, the circulation. Figure 20 shows changes in circulation during the boreal summer (JJA). On the northern hemisphere, only minLC_minCW shows some amplification of westerlies over the Eurasian mid-latitudes while the other simulations show negligible changes in wind speed for that area. The southern hemisphere also features perturbations in circulation pattern during both seasons (Figure 19 and Figure 20). It is interesting to note the strengthening of the high pressure field to the south of the African continent during the JJA season, in particular for minLC_minCW and minLC_refCW. This high

pressure field brings moist oceanic air to the Indian subcontinent and it may intensify the Indian monsoon. Hence, this implies that vegetation's uncertainties might have a noticeable impact on the large scale atmospheric circulation.

Figure 21 and Figure 22 show changes in 2m temperature due to vegetation uncertainty as well as changes in albedo and evapotranspiration. During the winter (DJF, Figure 21), changes in northern hemisphere temperature are controlled by albedo feedback and probably by changes in advection. Changes in southern hemisphere 2m temperature during winter, in particular for cases with increased vegetation (maxLC_maxCW and maxLC_refCW), are predominantly controlled by evaporative cooling. Experiments that decrease vegetation (minLC_minCW and minLC_refCW) show impact of albedo feedback and evaporative cooling on temperature. During the summer (JJA, Figure 22), evaporative cooling takes a predominant control over 2m temperature changes, especially over North America. The albedo feedback seems to be more important for the cases that minimize vegetation (minLC_minCW and minLC_refCW).

The impact of vegetation uncertainty on annual mean TP and T2M over the land is shown in Figure 23 and Figure 24, respectively. The major changes in precipitation occur in the Amazon, Congo and Indonesian rainforest. The feedback is positive, i.e. less vegetation - less precipitation. T2M shows the most significant warming with increasing vegetation along the north-eastern coast of the Eurasian continent. Seasonal changes (not shown) can be even stronger. During the boreal spring (MAM) maxLC_maxCW shows a warming up to 3 K along the north-eastern coast of the Eurasian continent and the north-western part of North America.

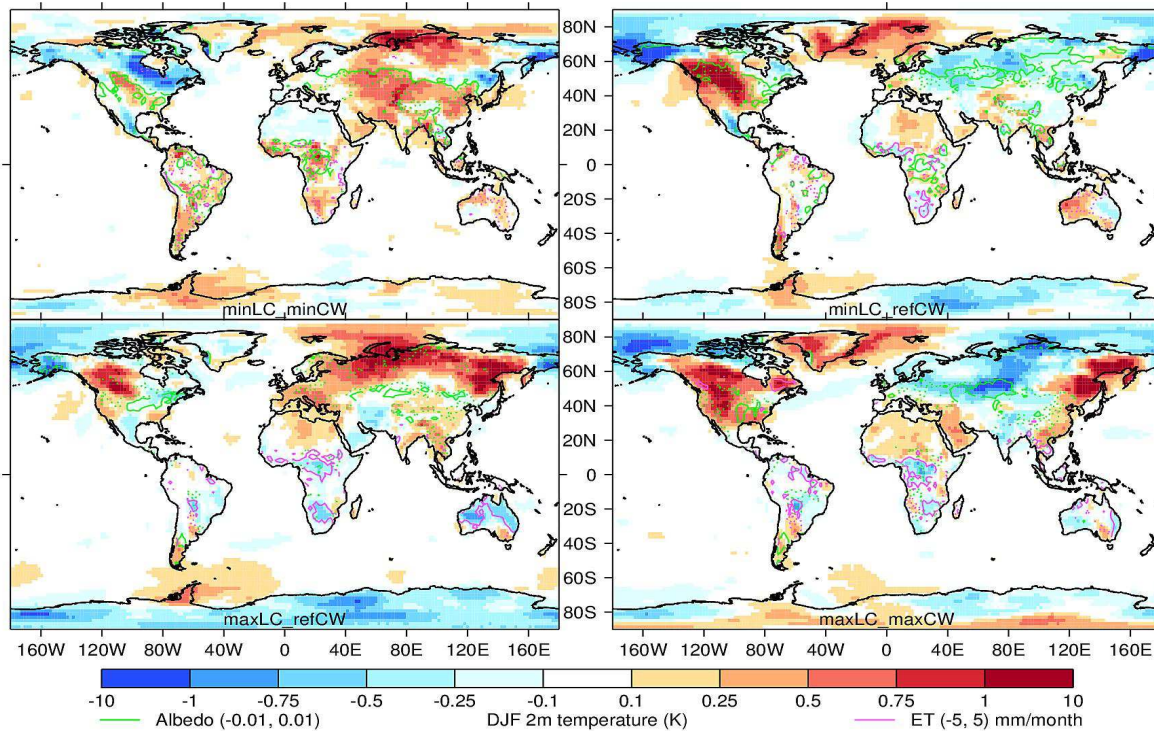


Figure 21: Boreal winter (DJF) mean 2m temperature differences from the reference simulation (refLCrefCW) for the 4 sensitivity experiments (Table 1). Overlaid contours show changes in albedo (green: -0.01 dashed line, and 0.01 full line) and evapotranspiration (magenta: -5 mm/month dashed line, and 5 mm/month full line).

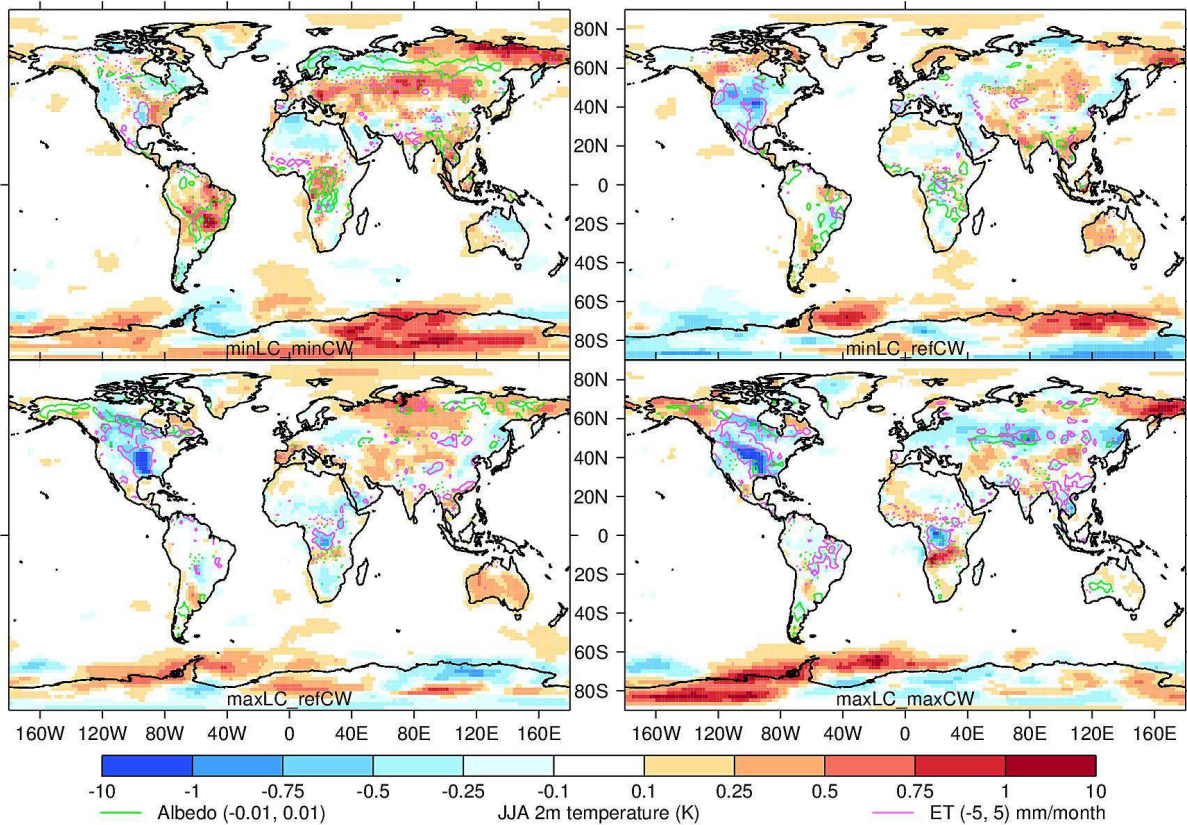


Figure 22: Boreal summer (JJA) mean 2m temperature differences from the reference simulation (refLCrefCW) for the 4 sensitivity experiments (Table 1). Overlaid contours showing changes in albedo (green: -0.01 dashed line, and 0.01 full line) and evapotranspiration (magenta: -5 mm/month dashed line, and 5 mm/month full line).

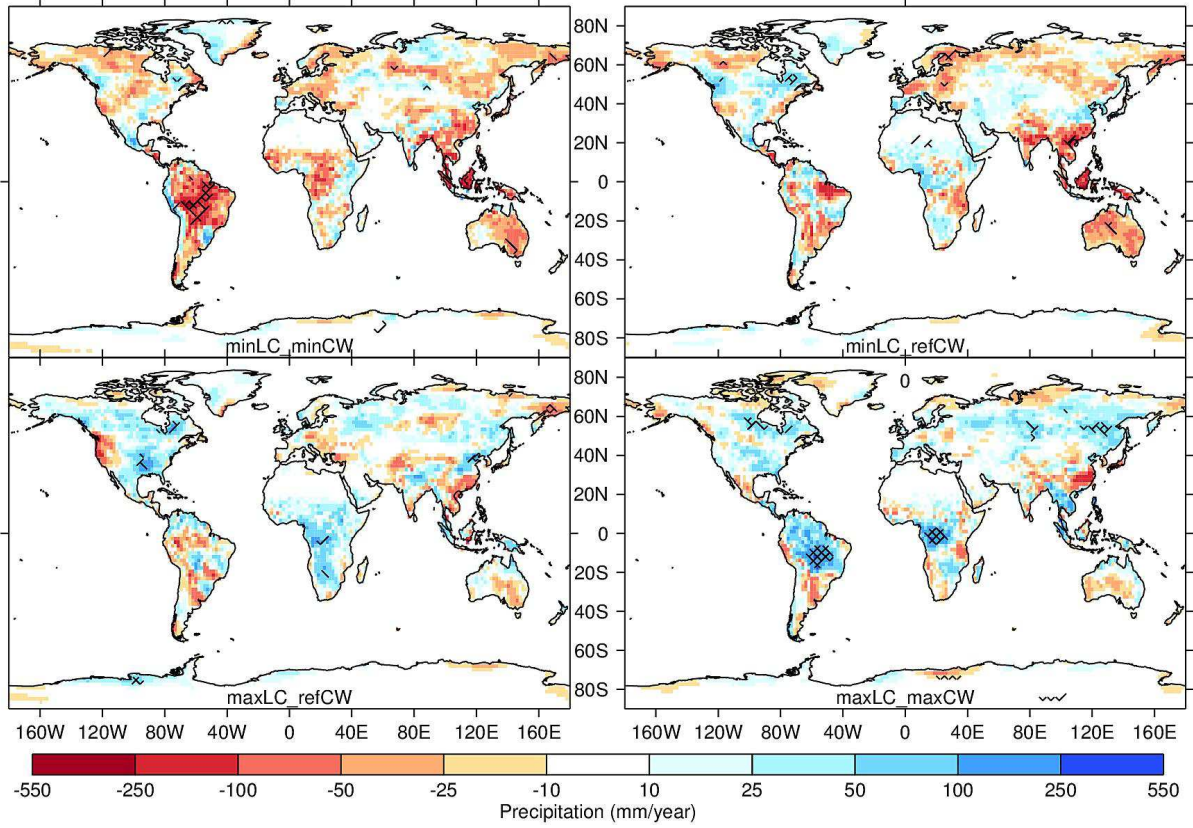


Figure 23: Annual total land precipitation deviations from the refLC_refCW simulation for the four sensitivity experiments (Table 1). Hatches indicate changes at 95% significance level according to t-test

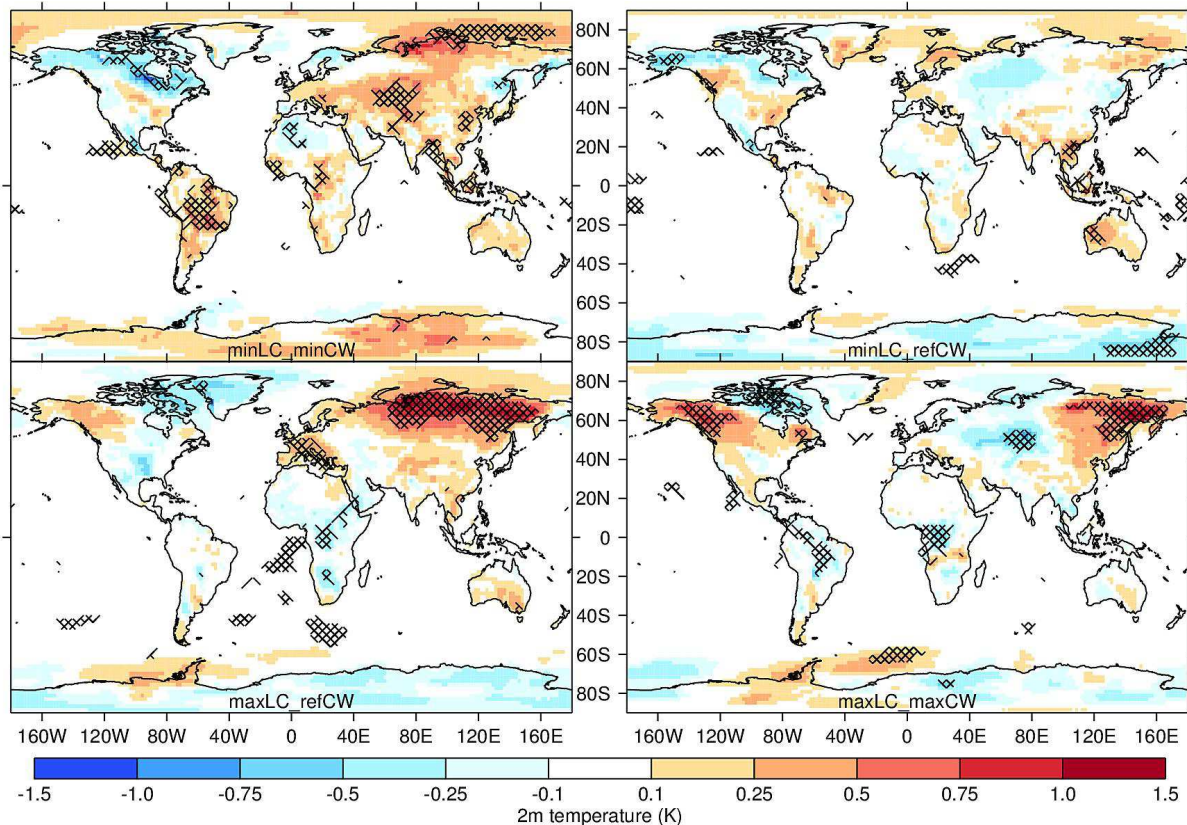


Figure 24: Annual 2m temperature deviations from the reference simulation for the four sensitivity experiments (Table 1). Hatches indicate changes at 95% significance level according to t-test.

3.1.4. Conclusions

The impact of land cover (LC) uncertainty on climate simulations with MPI-ESM has been investigated. The sensitivity of global climate has been quantified by focusing on variables that shape the global energy, water and carbon cycle. Though the range of uncertainty derived from the ESA remote sensing data and the conversion into PFT might seem exaggerated, this is the largest possible range of uncertainty. The estimated range of vegetation differences to the reference in either direction due to uncertainty is about the same order of magnitude as the observed LC change due to land use since 1700. Consequently, changes in the simulated climate appear to be about the same order of magnitude as the observed climate change due to land use. Furthermore, confirming the fact that vegetation impacts the terrestrial hydrological cycle (Sterling et al, 2013), but that even the uncertainty may be about the same order of magnitude as the observed recent change due to changing land use. For example, precipitation (P) is the largest component of the hydrological cycle, but understanding of its response to the LC change remains controversial and is still work in progress (Bonan (2008), Ellison et al (2012), Mahmood et al (2014), Sheil and Murdiyarso (2009)). Rainfall and its pattern change are strongly connected to winds and their circulation pattern. Combined satellite observations of precipitation and Leaf Area Index (LAI) have been investigated by Spracklen et al (2012). They found that the air transport over area bestowed with a larger LAI (e.g. forest rather than grass), results in increased tropical rainfall due to the increased moisture from the land surface that is transpired by trees, which in turn leads to an increased atmospheric humidity. Makarieva et al (2014) argued about methodological inconsistencies in the analysis conducted by Spracklen et al (2012) and provided

	Ref	LC CCI Phase 2: Climate Assessment Report, Year 3		
	Issue	1.0	Date 2017-07-11	
	Page	46		

an extended analysis that also includes the impact of forest on circulation pattern. Their analysis showed that the area covered with large forest favours the development of a low-pressure system which brings rainfall to the adjacent area, while sparse vegetated areas are associated with a high-pressure system, subsidence and low precipitation. These results are partially in agreement with our findings. We do find that precipitation increases with the increase of vegetation and the large scale circulation patterns are modified, but the evidence that LC induced changes in pressure and circulation pattern substantially contribute to changes in seasonal precipitation amount over the tropical rainforest is lacking in our experiments. This might be either due to misrepresented subgrid scale convective precipitation in MPI-ESMs or we should adopt the alternative hypothesis of Spracklen et al (2012) that precipitation increases rather due to increased rate of transpiration by the higher order vegetation type (trees) and, therefore, an increased amount of precipitable water is available in the atmosphere. However, except on plant type, the rate of transpiration depends on several factors including atmospheric conditions (temperature, relative humidity, circulation and atmospheric pressure) as well as soil moisture availability. Therefore, understanding the complex interactions among these factors and how much of precipitation could be attributed to each of them remains challenge due to subgrid scale processes. The application of global models with the possibility of high resolution local nesting over selected region of interest might help to resolve this issue. One such a tool is currently under development at MPI-M. Simulations performed with MPI-ESM2 based on ICON (ICOsahedral Non-hydrostatic, Zängl et al 2015) might help to progress understanding the response of rainfall and wind pattern change due to LC change. To explore the impact of vegetation uncertainty on the large scale circulation as well as their regional impact (e.g. NAO, ENSO, Indian summer monsoon), an ESM with a dynamic ocean needs to be employed.

3.2. Assessing Carbon Emissions from Wildfires using observed data from ESA-CCI-Fire and the JSBACH vegetation model

The ESA-CCI-LC data has been combined with the ESA-CCI-Fire v.4. data set and used in a study assessing carbon emissions from wildfires. The different ways of interpreting the conversion matrix from land cover classes to generic vegetation types have been used to access uncertainty ranges. In this study the JSBACH vegetation model and its build-in carbon model CBALONE have been forced with the CRU-NCEP v.5 atmospheric data and spun-up to carbon equilibrium followed by a transient run from 1901 to 2011.

The ESA-CCI-Fire v.4 covers the years 2005-2011 which are the only years used for the detailed analysis - for the spin-up and earlier transient period a climatological fire constructed from the ESA-CCI-Fire v.4. data set following the approach of van der Werf et al. (2010) has been applied. The fire data are given on the same vegetation classes as the ESA-CCI-LC data. These were mapped to the JSBACH PFTs using the same approach applied by Hartley et al. (2017) with the minor exception that all managed grass has been treated as pasture, since crops are not allowed to burn in JSBACH.

It seems, that even the LC version giving the minimal vegetation provides sufficient vegetated area to fulfil the burning requirements of the ESA-CCI-Fire v.4. and thus even this experiment gives the same carbon emissions as the reference experiments. On the other hand changing the relation between forest and grass or increasing the vegetated area leads to up to 34% higher emissions than in the reference experiment (2.38 Pg(C)/yr vs. 1.78 Pg(C)/yr). This is discussed in more detail in manuscript in preparation for Biogeosciences by Wilkenskeld et al. (2017).

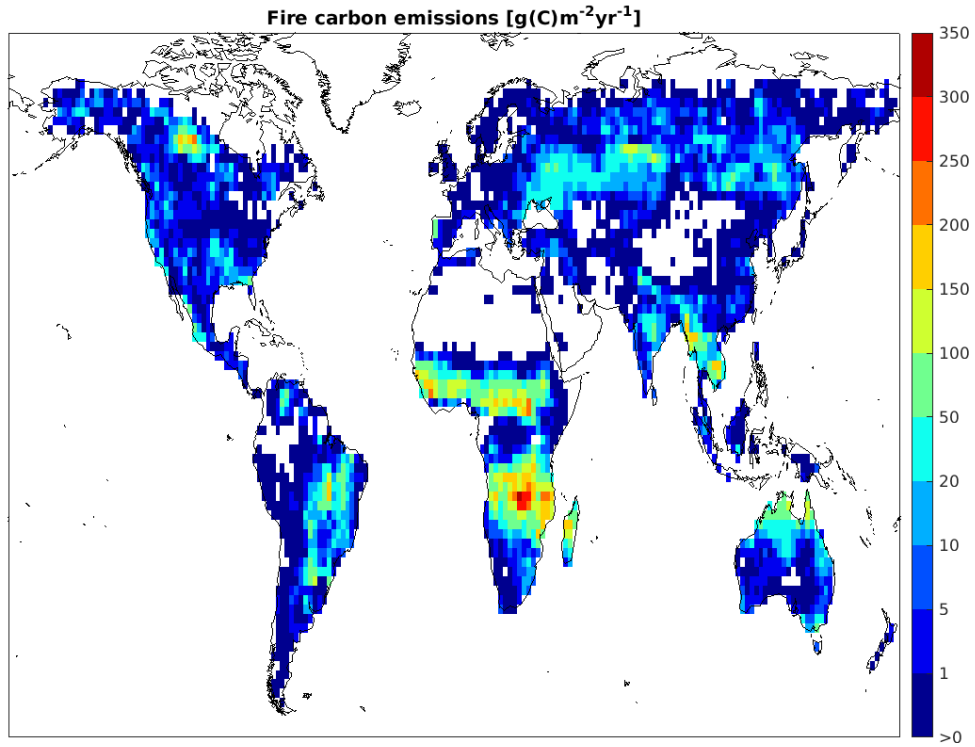


Figure 25: Geographical distribution of average wildfire carbon emissions [g(C)/(m² yr)] for the reference experiment (ESA-Ref land cover).

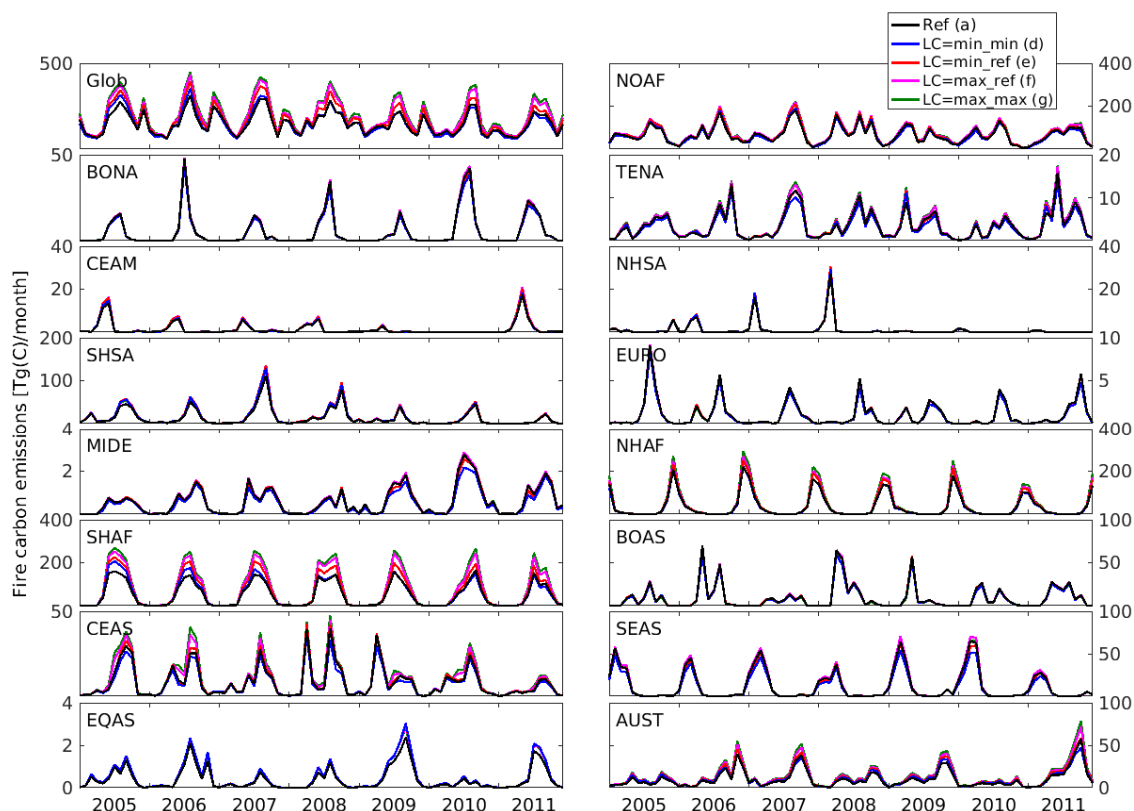


Figure 26: Time series of carbon emissions [Tg(C)/month] for different geographical regions (following van der Werf et al. (2010)) and the different land covers created from the ESA-CCI-LC data.

3.3. Benchmarking sensitivity of biophysical processes to leaf area changes in land surface models

A novel benchmarking system to assess model capacity in reproducing land surface–atmosphere energy exchanges modulated by vegetation density for different plant functional types comprising trees and grasses, is presented in the manuscript (Forzieri et al, 2017) submitted to the Journal of Advances in Modeling Earth Systems. Here a brief summary is provided. A consistent set of land surface energy fluxes and Leaf Area Index (LAI) dynamics has been generated from multiple Land Surface Models (LSMs), including JSBACH, JULES, ORCHIDEE, CLM and LPJ-GUESS. Sensitivities, that is relationships of interannual variations of modelled surface fluxes to LAI changes have been analysed at global scale across climatological gradients and compared with those obtained from satellite-based observation products of LAI, net radiation, latent heat and sensible heat, the latter deduced from the other fluxes to close the local energy budget. The observation products used to derive verification datasets are listed in the Table 4. ESA-CCI-LC is used to derive Plant Functional Types (PFT). Default cross-walking procedure is described in Poulter et al. (2015). A further aggregation to two broad PFT classes based on physiognomy alone has been used to synthesize results: grasses (including crops) and trees (Figure 27). Finally, the Global Map of Irrigation Areas, GMIA (<http://www.fao.org/nr/water/aquastat/irrigationmap/index.stm>) has been used to identify areas

	Ref	LC CCI Phase 2: Climate Assessment Report, Year 3		
	Issue	1.0	Date 2017-07-11	
	Page	49		

affected by irrigation. This map was derived from statistical census data and provides the percentage of irrigated area per grid cell in 2005. LSM are driven with historic climatic CRU-NCEP data (version 6, http://dods.extra.cea.fr/data/p529viov/cruncep/V6_1901_2014/) and CO₂ concentrations consistent with the TRENDY project (Sitch et al. 2015) for the period 2000-2014.

Scoring metrics quantify the agreement between observed and modelled sensitivities of energy fluxes to variation in LAI across the different climates. They integrate the model-data displacement over the whole climatological space and the full spectrum of LAI variability and allow identifying overall model performances.

Single LSMs show comparable performances across T and P gradients, whereas a larger variability emerges across different scoring metrics, energy budget terms and vegetation covers (Figure 28). There is no systematic bias across the considered ensemble of LSMs in the observed year-to-year fluctuations in annual surface heat fluxes (PBIAS ranging between ~-60% and ~200%). Trees show larger biases on turbulent fluxes compared to net radiation while grasses present comparable patterns (Figure 28 a,b). Overall, larger PBIAS values appear in modelled fluxes with higher explained variance by LAI compared to satellite-derived estimates. Deviations in interannual variability of turbulent fluxes are up to two fold bigger than those on net radiation (RMSE ~7 Wm⁻² in Δ LE and Δ (H+G) versus ~3.5 Wm⁻² in Δ RN, Figure 28 c,d), except for ORCHIDEE that shows the contrary. Simulated bioclimatic spaces of grasses appear well reproduced and strongly correlated with observations (~ ρ >0.8, Figure 28 e,f). A lower agreement emerges for trees that may even present negative correlations for certain models/energy terms (e.g., notably for sensible and ground heat fluxes), thus suggesting a reversed LAI-control on simulated biophysical processes compared to observations (discussed in detail in the manuscript Forzieri et al, 2017).

Results are rather contrasting between trees and grasses. Grasses appear to be reasonably well represented in models with respect to observation-based interannual sensitivity of turbulent fluxes to LAI, increasing the confidence on how the LAI-dependent partition of net radiation into latent and sensible heat are simulated in LSMs for this biome. On the contrary, trees are characterized by an underestimation of year-to-year variability of LAI in cold climates, ultimately affecting the amount of absorbed radiation due to the misrepresentation of LAI effects on surface albedo. In addition for trees, the sensitivity relationships between LAI and turbulent fluxes appear to contradict those extracted from the observational dataset. Such systematic errors shed light on limitations of our current understanding of the mechanisms controlling the surface energy balance.

There is no overall best performing LSM resulting from the inter-comparison, models may outperform limitedly to specific metrics, surface heat fluxes, vegetation covers and climate drivers. For instance, JSBACH and ORCHIDEE show generally higher capacity to reproduce the spatial patterns of the observed bioclimatic spaces (high correlation values); JULES and CLM provide lower deviations in absolute terms (low RMSE values); and LPJ-GUESS generates minor systematic biases (low PBIAS values, limitedly to latent fluxes) compared to the other LSMs. In contrast, ORCHIDEE shows lower performances in terms of RMSE; JSBACH and CLM have generally higher systematic biases (overestimating and underestimating benchmarks, respectively); JULES and LPJ-GUESS are poorly correlated with observations compared to the other LSMs.

Variable	Product	Temporal resolution	Temporal coverage	Domain	Spatial resolution
Net radiation	CERES	3-hourly	2000–2015	Global	1°
Evapotranspiration	GLEAM	daily	2000–2015	50°S–50°N	0.25°
Leaf area index	GIMMS3g	15-day	1982–2011	Global	1/12°
Precipitation	CRU	monthly	1901–2014	Global	0.5°
Air temperature	CRU	monthly	1901–2014	Global	0.5°
Plant functional type	ESA-CCI	static	2000–2010	Global	1° (derived from 300m)
Global Map of Irrigated Area	GMIA	static	2005	Global	5 min

Table 4 Observation-based products used to derive benchmark diagnostics.

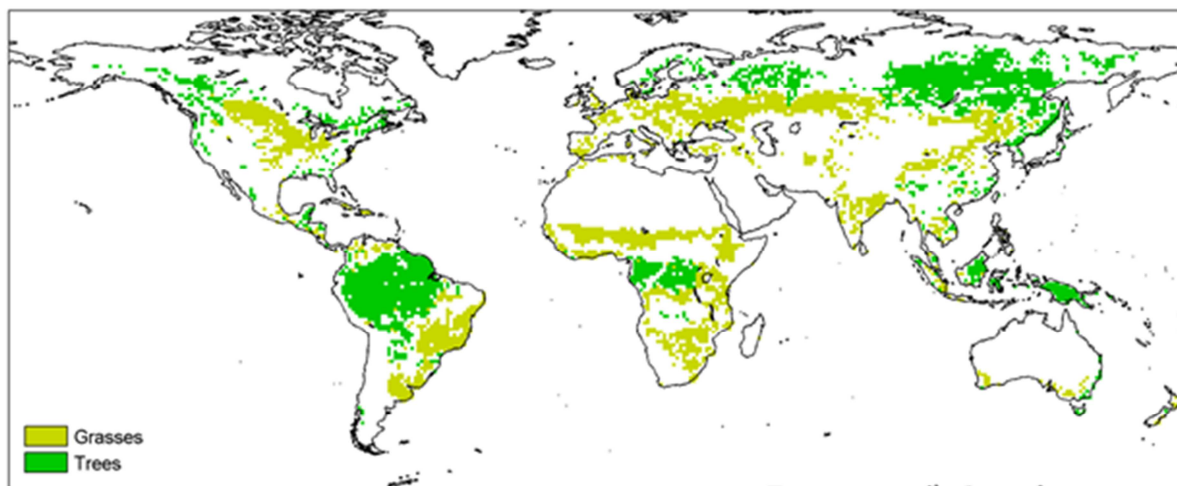


Figure 27: Selection of pixels used in this work, which have a cover fraction ≥ 0.6 for the broad PFT classes ‘grasses’ and ‘trees’ derived from the ESA-CCI land cover map of 2010 at the 1° resolution and with < 0.1 of irrigated area derived from the GMIA product

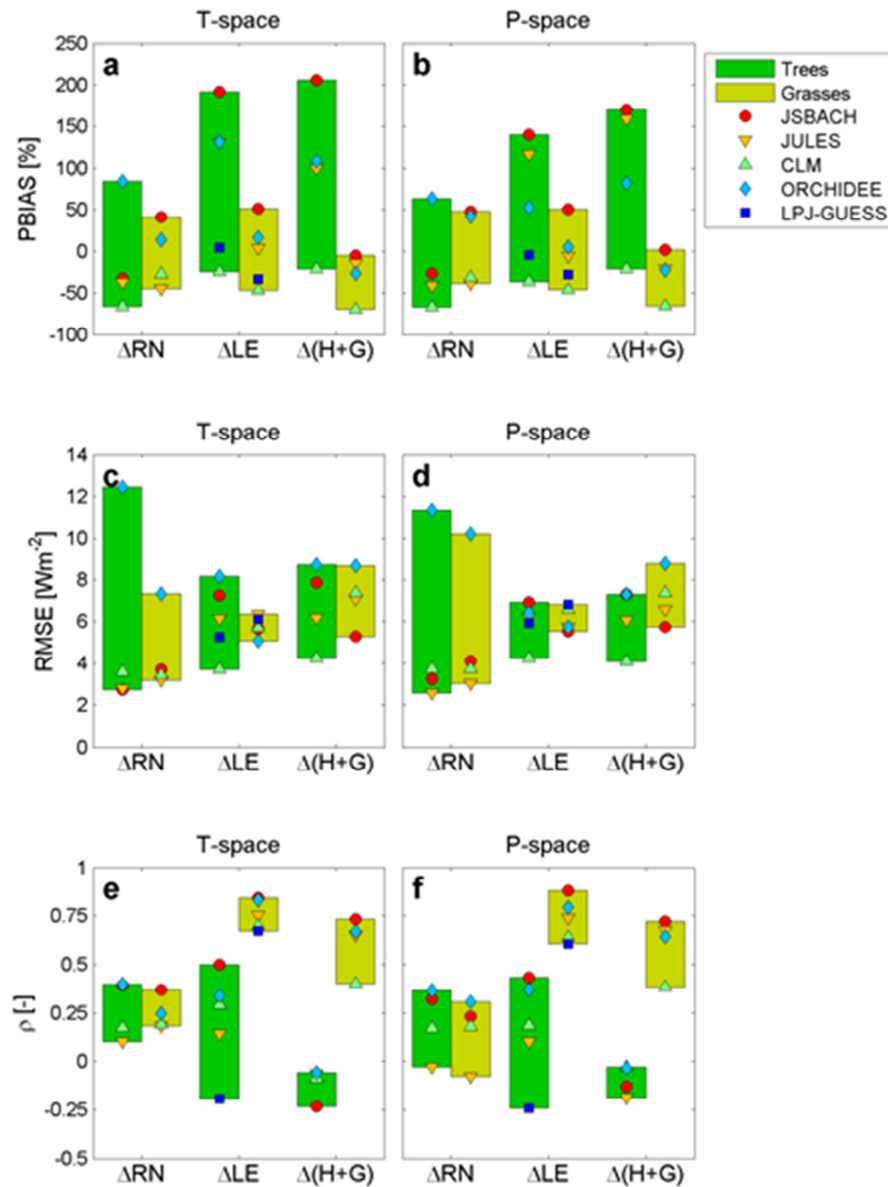


Figure 28 : Overall model performances in reproducing the interplay between interannual variations in annual average leaf area index and net radiation (ΔRN), latent heat (ΔLE) and soil and ground heat ($\Delta(H+G)$) over the climatological medians of temperature and precipitation gradients (on the left and right column respectively). Performances are quantified in terms of percent bias (PBIAS, upper row), Root Mean Square Error (RMSE, middle row) and Spearman rank (ρ , bottom row). Model-specific performances are visualized with different symbols accordingly to the legend. Inter-model spreads on tree and grass coverages are shown in light and dark green, respectively. Scoring metrics quantified over the climatological median of air temperature and precipitation gradient are shown on the left (T-space) and right (P-space) columns, respectively.

	Ref	LC CCI Phase 2: Climate Assessment Report, Year 3		
	Issue	1.0	Date 2017-07-11	
	Page	52		

3.4 Recommendation

In order to support climate community and analysis, data of the ESA-CCI-LC package is still missing straightforward technique for the separation of inland water from ocean water. This is necessary for the generation of a continental land sea mask that comprises a land area fraction. This should be defined as: $Land_area_fraction = (1 - Water) + Inland_water_fraction$.

This is necessary for land surface models that take into account all cover fractions over land including inland water. At 0.5 degree resolution, MPI-M derived such a land_area_fraction with coarse approximation. This approximation neglects most of the inland water close to the coast (it is counted as ocean water) and may misidentify parts of ocean water as inland water in areas of complex land - sea water distributions, in particular:

- In areas where ocean water intrudes deeply into land or is surrounded by a lot of land areas like island, ocean water may be erroneously identified as inland water, e.g. Northern Canada, Canadian Archipelago;
- Inland water close to the coast will be erroneously identified as ocean water;
- Inland water in manual regional corrections will be erroneously identified as ocean water e.g. Canadian Archipelago.

	Ref	LC CCI Phase 2: Climate Assessment Report, Year 3		
	Issue	1.0	Date 2017-07-11	
	Page	53		

4. MOHC ASSESSMENT OF SR AND NDVI CONDITION PRODUCTS FOR EVALUATING THE GROWING SEASON IN JULES

Authors: **Andrew Hartley, Deborah Hemming, Neil Kaye, Hamish Steptoe**
Met Office Hadley Centre, Fitzroy Road, Exeter. Devon. UK.

The aim of this report is to evaluate the usefulness of the LC-CCI surface reflectance and Normalised Difference Vegetation Index (NDVI) condition products for evaluation of phenology in the JULES land surface model. This builds on year 2 work by having a particular focus on indicators of vegetation seasonality that may allow for a more effective comparison between satellite-based radiance observations and modelled Leaf Area Index (LAI).

4.1. Introduction

The research summarised in this report builds on work, conducted in year 2 of the project, which provided an assessment of the usefulness of the LC-CCI NDVI condition product for applications in Land Surface Model (LSM) evaluation, with a particular focus on the phenology of LAI (LC_CCI CAR, 2016). This assessment showed general agreement with results comparing NDVI and LAI that are available in the literature, highlighting that significant relationships between LAI and NDVI exist, and can be explained by the link between vegetation structure and reflectance characteristics. However, it is clear that there is no simple, global relationship between NDVI and LAI, instead the relationships are spatially and temporally complex, relying on biome-specific calibrations, compensating biophysical processes, and variations in canopy traits including phenology and structure. These differences can provide useful information to better understand the particular processes and/or vegetation types under observation.

For further work to make better use of satellite observations in ESM evaluation, our year 2 report made the following suggestions:

- In view of the general agreement noted in results presented in this study with previous studies in the literature, further consideration of the reasons for the spatial and temporal relationships between NDVI and LAI (and other vegetation metrics) would be useful to develop greater understanding of their underlying processes.
- Further research is needed to understand how best to relate satellite retrievals of vegetation spectral characteristics and their derived metrics, e.g. NDVI, to canopy-scale modelled outputs, such as LAI. This could include assessment of the influence of inconsistent assumptions between satellite data processing and LSMs, e.g. the assumption of leaf angle distributions, and consideration of the newer enhanced vegetation indices.
- Further work is also needed to produce diagnostics from LSMs that more closely match satellite retrievals. For example, spectral albedo is already a common output from LSMs, and there is no reason why reflectances from vegetation cover cannot also be estimated in LSMs in order to more closely simulate the satellite retrievals.

© UCL-Geomatics 2017

This document is the property of the LAND_COVER_CCI partnership, no part of it shall be reproduced or transmitted without the express prior written authorization of UCL-Geomatics (Belgium)

	Ref	LC CCI Phase 2: Climate Assessment Report, Year 3		
	Issue	1.0	Date 2017-07-11	
	Page	54		

The work conducted this year, and summarised in this report, goes some way to addressing these suggestions. Specifically, we focus on:

- i) Improving the characterisation on phenological events using established methods to derive 10 key phenology indicators using established methods.
- ii) Deriving a LSM estimate of NDVI from surface reflectance properties modelled in JULES. This modelled NDVI diagnostic provides a closer comparison to NDVI products estimated from satellite retrievals than other modelled diagnostics.
- iii) Providing more detailed assessment of spatial, temporal and biome-specific relationships between JULES-NDVI-derived and satellite-NDVI-derived phenology indicators. This will improve understanding of the underlying processes regulating phenological changes, and uncertainties in their interpretation using satellite and LSM estimates.

4.2. Method

4.2.2. Datasets

The following datasets are used for these analyses:

4.2.2.1. Copernicus NDVI v1.3 (Copernicus-NDVI)

- 1km spatial resolution based on SPOT VGT 1&2
- 10-day time-series (dekads)
- Covers the period 1999-2014 (PROBA-V sensor from 2014 onwards...)
- Cloud masking and processing not as strict as the SR dataset, but better coverage

4.2.2.2. MERIS Surface Reflectance (SR-NDVI)

- 1km spatial resolution, based on 300m MERIS data
- 7-day time-series
- Covering the period Jan 2003 – March 2012
- NDVI has been calculated from the full spectral product
- Clouds and haze have been masked out, but means that coverage is sparse

4.2.2.3. NDVI Condition Product (NDVI Condition)

- 1km spatial resolution based on SPOT-VGT 1&2
- 7-day time-series of climatology
- Based on the period 1999-2012
- Very few data gaps due to 14 years contributing to 1 value

4.2.2.4. JULES NDVI Simulations (JULES-NDVI)

- Reference simulation from the PFT uncertainty experiment (Hartley *et al.*, 2016)
- 2x2 degree spatial resolution
- Forced by WFDEI driving data for 1979 to 2010
- Daily outgoing SW and NIR radiation used to calculate NDVI
- Aggregated to 7 day periods to match satellite condition product

4.2.3. Obtaining the data

SR-NDVI data from MERIS was downloaded from Brockman consulting via FTP. Copernicus data was obtained through the Copernicus web site (<http://land.copernicus.eu/global/products/ndvi>). Scripts have been written in Python and Shell to download, extract from Zip and Mosaic the continental datasets into global ones.

4.2.4. Giorgi regions

For much of the report, data is aggregated to Giorgi regions to as a means to compare high resolution satellite data and low resolution climate models. Figure 29 shows the location of the Giorgi regions.

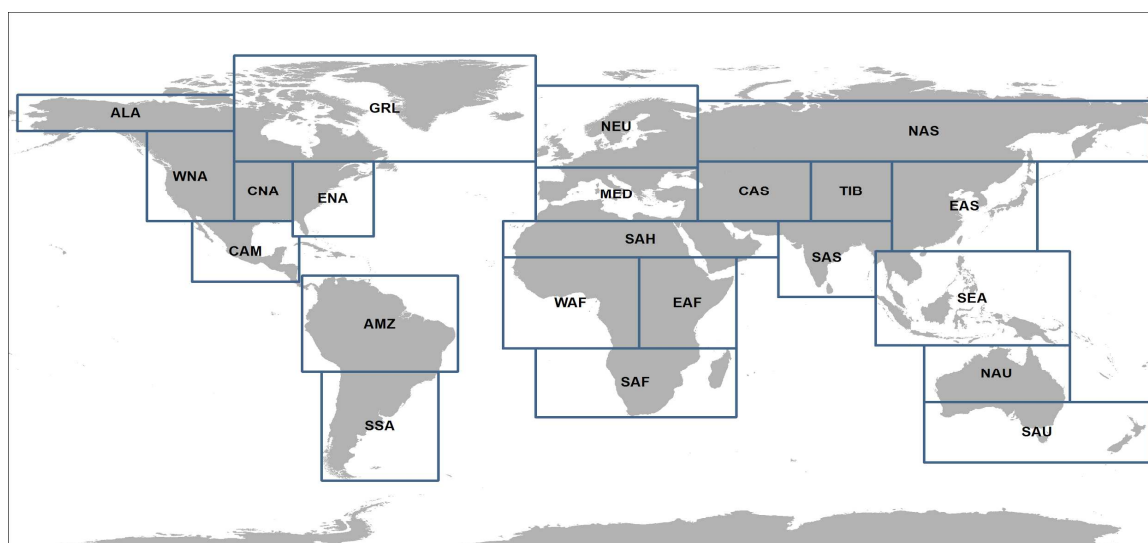
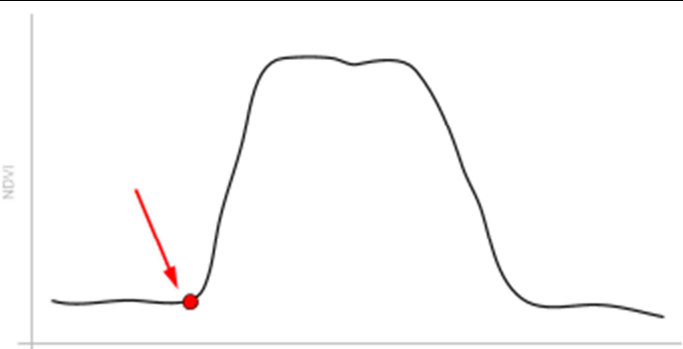
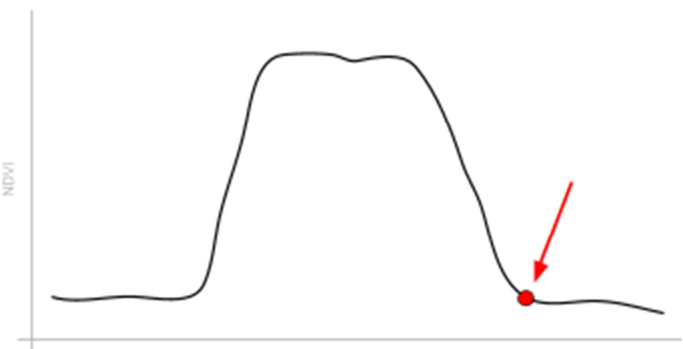
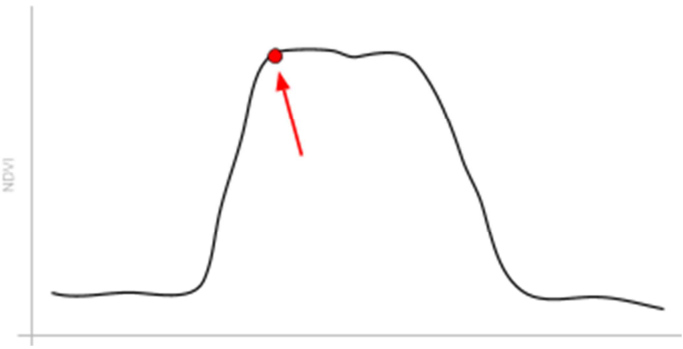
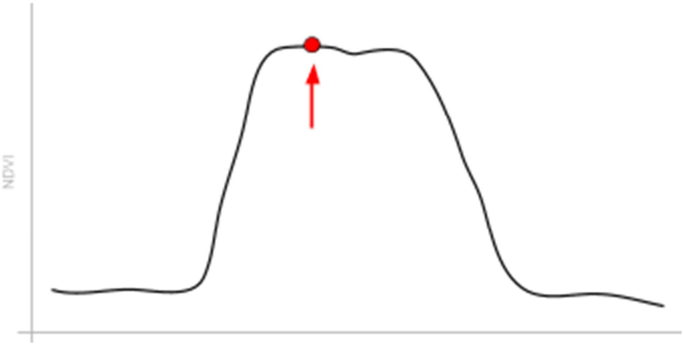
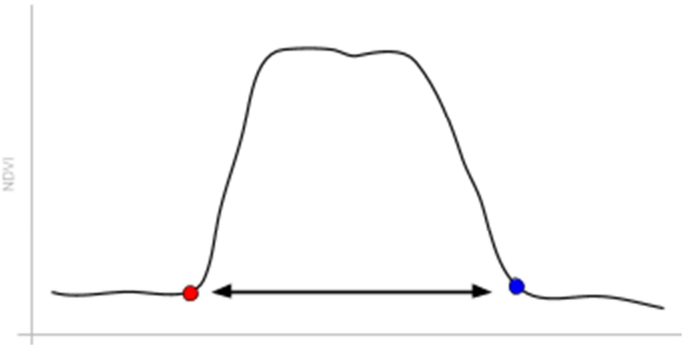
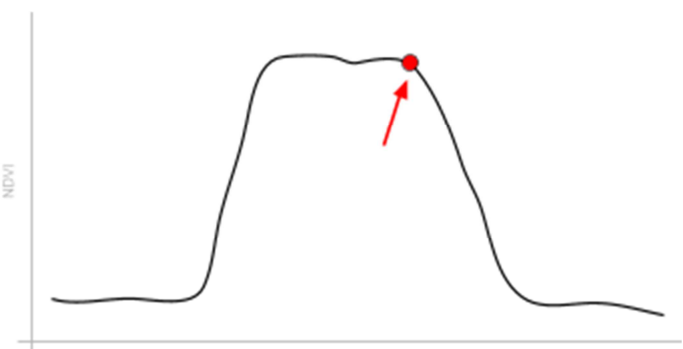
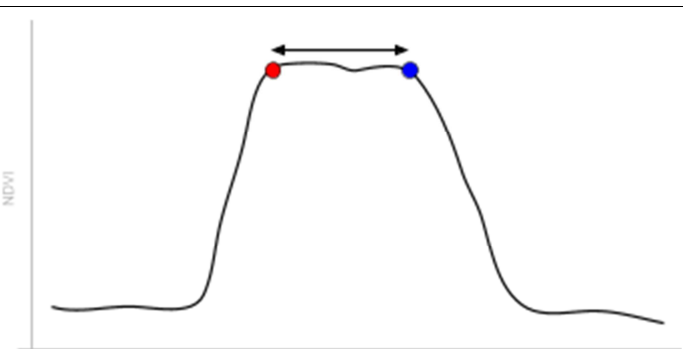


Figure 29: Location and abbreviation of Giorgi regions used in this report.

4.2.5. Phenology Indicators

Ten key phenological phases (Figure 30) can be defined using the following indicators (adapted from Clerici et al., 2012; Zhang et al., 2003):

Name	Description	
Start-of-Season (SOS)	Onset of photosynthetic activity	
End-of-Season (EOS)	Physiological activity becomes near zero	
Maturity (Ma)	Date at which plant green leaf area is maximum	
Peak-of-Season (POS)	Max NDVI in an annual time-series	

Base-of-Season (BOS)	Min NDVI in an annual time-series	
Length-of-Season (LOS)	Difference in time between EOS - SOS	
Senescence (Se)	Date at which photosynthetic activity and green leaf area rapidly declines	
Length-of-Greenness (LOG)	Difference in time between Senescence - Maturity	

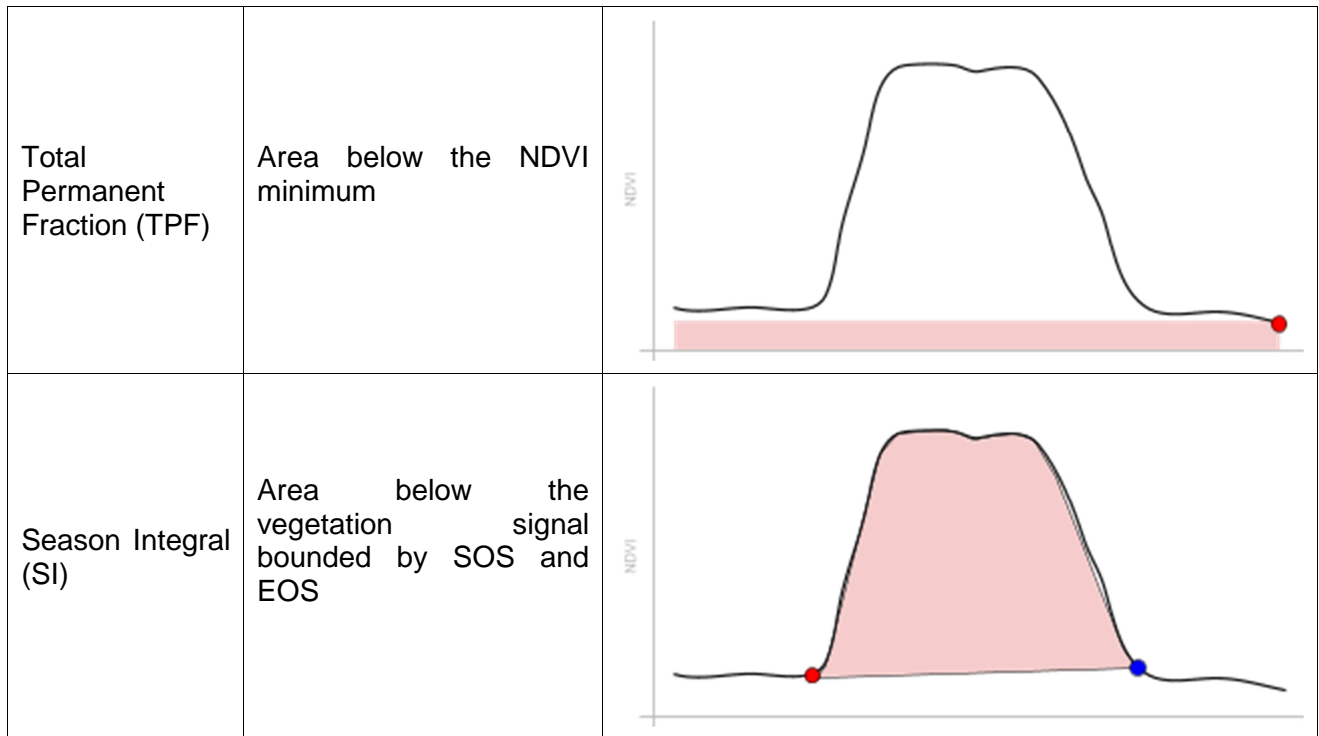


Figure 30: Graphical representation of seasonal indicators used in this report

4.2.6. Approach

The assessment of the value of satellite-derived NDVI products for the evaluation of modelled phenology involved 4 different investigations:

1. Assessed data coverage of each satellite product, in terms of 1km spatial resolution monthly maps, and the mean seasonal cycle by Giorgi region
2. Assessed the impact of spatial scale of aggregation on the completeness of the NDVI time-series
3. For mean seasonal cycle, compared the simulated JULES-NDVI to satellite NDVI products
4. For key phenology indicators, compared the simulated JULES-NDVI to Condition-NDVI product.

The following sections explain in more detail the steps taken, and the results found at each stage of the analysis.

4.3. Assessment

4.3.2. Data Coverage

In order to understand constraints on data coverage in both SR-NDVI and Copernicus-NDVI time-series products, spatial coverage of NDVI was calculated for each month. Data was extracted from both products for the overlapping time period (January 2003 through to March 2012), and the following method was applied to both SR-NDVI and Copernicus-NDVI:

- For each month select all satellite files that occur in that month. For example all January files between 2003 and 2012.

- For each 1km pixel within each of the files calculate whether it has a data value. Taking a grid cell over London as an example, if in the thirty Copernicus-NDVI files for March, twelve of them have a value (and the rest are no data) assign a proportion of coverage of 40%. This is repeated for every land pixel in the world.

Generally, it was found that the data coverage of NDVI is far greater in the Copernicus-NDVI compared to the SR-NDVI.

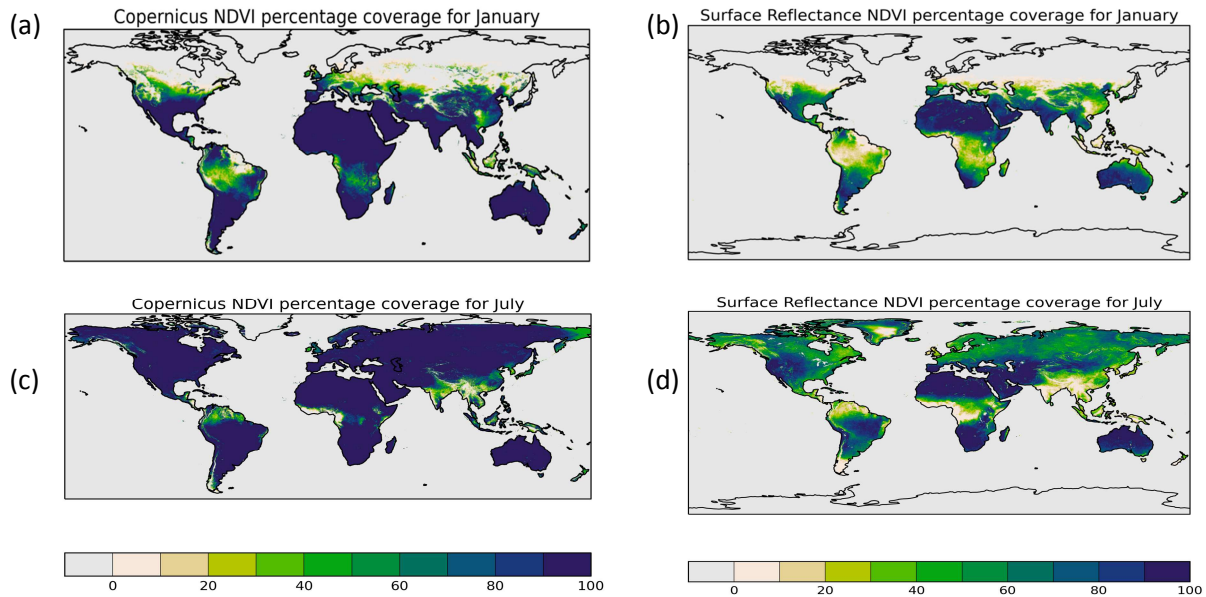


Figure 31: Comparison of (a) Copernicus-NDVI and (b) SR-NDVI average data coverage for January (c) Copernicus-NDVI and (d) SR-NDVI average data coverage for July.

Figure 31 shows the result of these calculations for January and July (Appendices for MOHC model results Appendix MOHC – 1 has all months).

For both of the products the coverage is clearly smaller in January, however it varies considerably between the products; the SR-NDVI product only goes to about 45° north compared to about 60° north for the Copernicus-NDVI. Looking at July (c and d) it is clear that Copernicus-NDVI has a far higher coverage >90% for most of the world. This high level of coverage is only seen in arid areas for the SR-NDVI product.

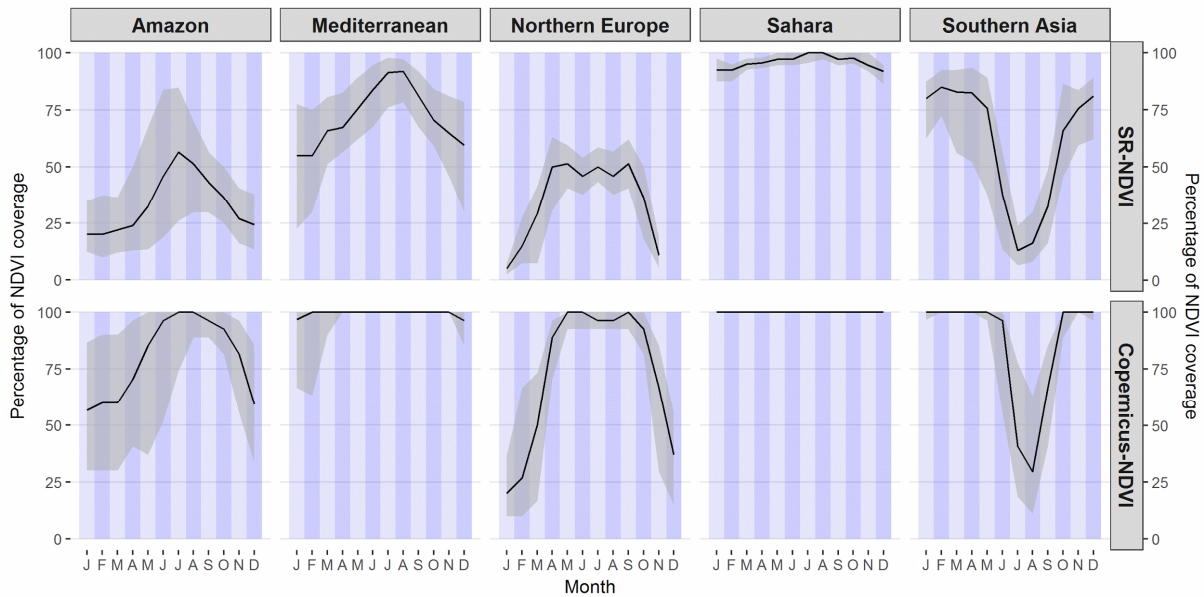


Figure 32: Monthly coverage of NDVI for selected Giorgi regions, black line is 50th percentile and grey band is 25th to 75th percentile.

Figure 32 plots monthly coverage of NDVI for 5 contrasting Giorgi regions. It is clear that overall there is far higher coverage for the Copernicus dataset for all 5 regions. Looking at the Northern Europe region for SR-NDVI the Median value varies from about 5 to 10% coverage in January and February to about 50% coverage between April and August. The Copernicus-NDVI product shows a similar seasonal pattern but values vary from around 25% in January and February to plateau at around 95% for April to September. In Southern Asia, coverage reflects the peak of the Indian monsoon with the dramatic drop in July and August coinciding with cloudy conditions. In this region, Copernicus-NDVI has 20% more coverage throughout the year. The cloudless Sahara region unsurprisingly has very high coverage all year. The Amazon shows greatest coverage in the months from June to October although overall Copernicus-NDVI has twice the coverage of the SR-NDVI product. The Mediterranean region has almost complete coverage for the Copernicus-NDVI product but for the SR-NDVI product there is a seasonal cycle with more coverage in the summer months.

4.3.3. Spatial Scale of aggregation

As shown above, for certain locations there is limited coverage of NDVI data at different times of year. In order to assess the best resolution to create seasonal time-series, an analysis of the effect of scale on data completeness was performed. Northern Europe was chosen as an example area (see Figure 5) because it is particularly deficient in NDVI data. A central location over the northern Europe region was chosen at 60°N and 15°E. Seven different resolutions (shown in Figure 33 and Figure 34) were examined from a single pixel location to increasingly sized boxes of 3km, 10km, 35km, 140km, 550km and 1100km (light blue in Figure 33) as well as the whole northern European Giorgi region.

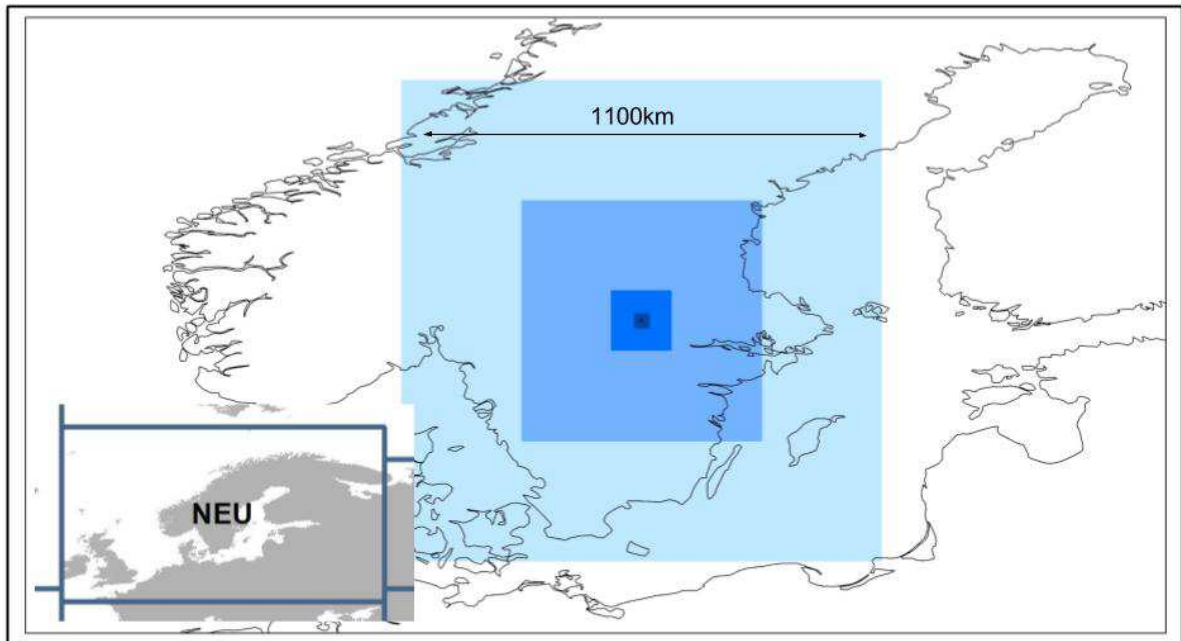


Figure 33: Boxes used to examine impact of resolution on completeness of a time-series.



Figure 34: The impact of varying spatial resolution on production of time-series of NDVI (for 2006, 2007 and 2008). The Condition-NDVI product is plotted with repeating annual cycle because it does not contain year-to-year variability.

Figure 34 shows very clearly that the size of the averaging box has a major impact on the completeness of the time series. For a single location, all datasets have missing data in the winter months, due to snow cover and/or cloudiness. For Copernicus-NDVI, the data is much sparser with no data between December and March, and some apparently spurious low values towards the end of the growing season. For SR-NDVI there are massive gaps in the data at the single pixel resolution, due to there being little data available in the winter as well as cloud cover for the rest of the year.

	Ref	LC CCI Phase 2: Climate Assessment Report, Year 3		
	Issue	1.0	Date 2017-07-11	
	Page	62		

As the size of the averaging box increases, the time series is increasingly filled in, this is especially obvious for the SR-NDVI product. For SR-NDVI at a 140km box size there is a continuous time series between March and October. At this scale, Copernicus-NDVI has an almost complete time series although it is still quite erratic in shape. Increasing the size of the spatial box to 1100km keeps improving the consistency of the time-series for both SR-NDVI and Copernicus-NDVI. However even at this scale the time-series are quite erratic and spiky.

A significant improvement is seen when aggregated to the North European Giorgi region. This produces a smoother and less spiky time-series with far fewer gaps. This is clearly because more grid cells are incorporated into the average due to the region including land further south and therefore encompassing more grid cells in the winter months. An advantage of aggregating to this resolution is that it makes it far easier and more meaningful to compare to the far lower resolution climate model data as will be shown in later sections.

4.3.4. Mean seasonal cycle

Given clear data gaps in the multi-year time series, it was decided to continue the analysis by aggregating the time series data to produce multi-year means for a given week or 10-day period. Additionally, this data was aggregated to Giorgi region by plant functional type (PFT) to compare to JULES-NDVI. This allowed a more consistent time-series to be used that could be compared directly to model output. The following steps were taken to produce time-series of the satellite data:

- Aggregate 300m land cover ESA CCI Land Cover dataset (v 1.6.1 for 2005) to the resolution of SR-NDVI (~0.011 degrees) and Copernicus-NDVI (~0.0089285 degrees) satellite products.
- For each version of aggregated data create a binary mask where Grass, broadleaved forest, needleleaf forest and shrub are the dominant class i.e. greater than 0.5 of the proportion for the pixel.
- For each Giorgi region find the 25th, 50th and 75th percentile of the NDVI values occurring in each of the dominant PFTs for every week from January 2003 to March 2012.
- Create 10-year averages for each week (SR-NDVI) or dekad (Copernicus-NDVI) of the year to create a seasonal time-series.

To produce the time-series for the JULES model data the following steps were performed:

- For each 2x2 degree grid cell in the model data create a weighting layer for Grass, Shrub, broadleaved and needleleaf forest. This is created by multiplying the area of the grid cell in square km and the proportion of a particular PFT in the grid cell. This means if there is none of the PFT in that grid cell the weighting is zero.
- For each grid cell and each PFT create a weighted grid cell value over the globe
- Create a weekly time-series of mean and standard deviation across each Giorgi region.
- Create a 10-year average for each week in the model time-series.

When averaged across Giorgi regions, the 3 different satellite products (Condition-NDVI, Copernicus-NDVI and SR-NDVI) show similar seasonal profiles across all PFTs and for all Giorgi regions (see Appendix MOHC - 3 for all regions). In magnitude SR-NDVI has consistently higher values than Copernicus-NDVI which are in turn higher than Condition-NDVI. The shapes of the seasonal pattern are similar, although exact onset of greening and browning varies slightly.

For all Giorgi regions where there is a strong temperature-based seasonal cycle, there appears be reasonable consistency between JULES and satellite observations (e.g. Figure 35 Northern

Europe). Although, the Mediterranean region shows major inconsistencies in the amplitude and phase of the seasonal cycle for Needleleaf, Grass and Shrub PFTs (Figure 36 Mediterranean).

In tropical areas, there is no seasonal cycle in the JULES-NDVI for all PFTs, even when the satellite observations show a clear seasonal cycle (e.g. Figure 37 and Figure 38 of Southern Asia and Amazon).

For JULES-NDVI there is an upper limit for each PFT, which is 0.74 for Broadleaf forest, 0.59 for Needleleaf forest, 0.79 for Grass and 0.8 for Shrub. This causes a plateau in the data when this limit is reached. Looking at Figure 35 for Needleleaf forest in Northern Europe, while the Copernicus-NDVI and SR-NDVI satellite products peak around 0.75 JULES-NDVI flatlines between March and October at 0.59, this masks seasonal cycle.

In temperate regions the Broadleaf tree PFT compares best to satellite observations, although the seasonal cycle of JULES-NDVI has a slower onset and decline than the satellite data. In tropical regions there is a flat profile for Broadleaf tree and this always seems to be set to the upper limit of around 0.74.

For the temperate regions Needleleaf tree is consistent within the Satellite products albeit with a flatter profile for SR-NDVI. The magnitude of NDVI is consistently lower for the condition product peaking at about 0.5. For SR-NDVI the values are usually highest with values around 0.7.

The profile for Grass is very consistent across all the Satellite products although the magnitude varies slightly. For JULES-NDVI in the tropical regions values flatline all year around the maximum for the product. The season is far flatter in JULES-NDVI than the satellite products and is not captured. Shrub is quite consistent for the Satellite products but is mostly much higher for JULES-NDVI and often plateaus around 0.8.

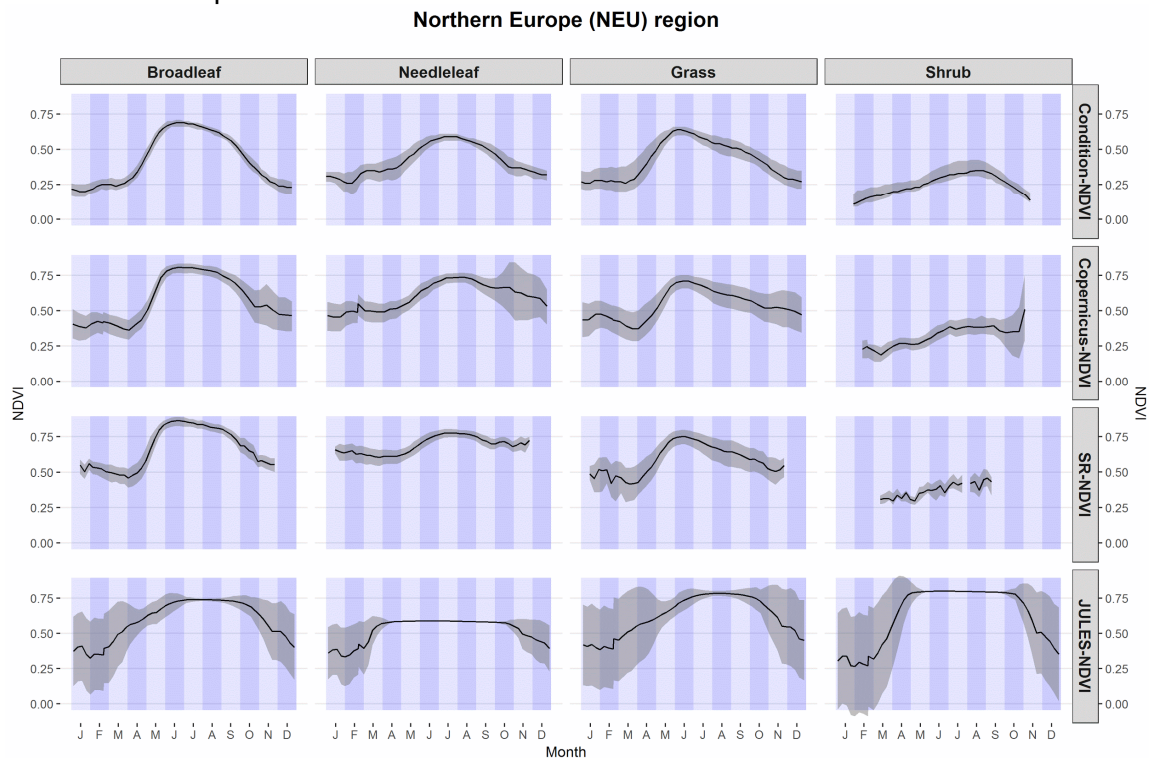


Figure 35: Northern Europe seasonal cycle for 4 plant functional types and 4 NDVI products

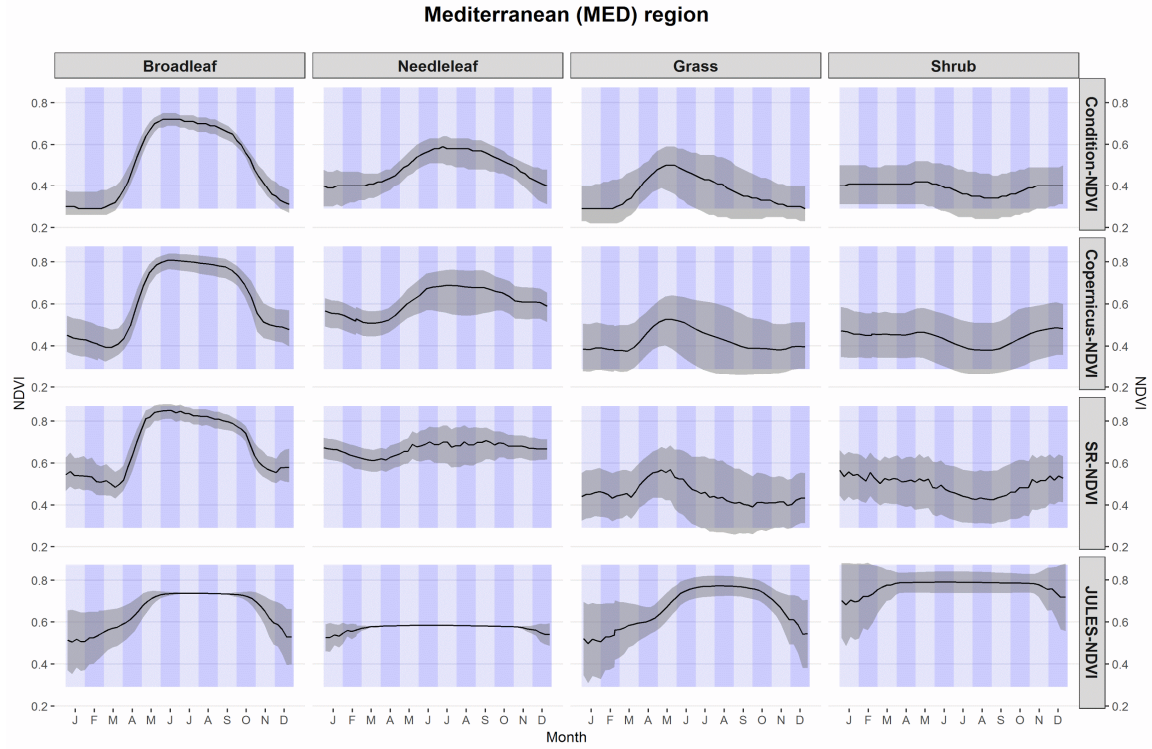


Figure 36: Mediterranean seasonal cycle for 4 plant functional types and 4 NDVI products

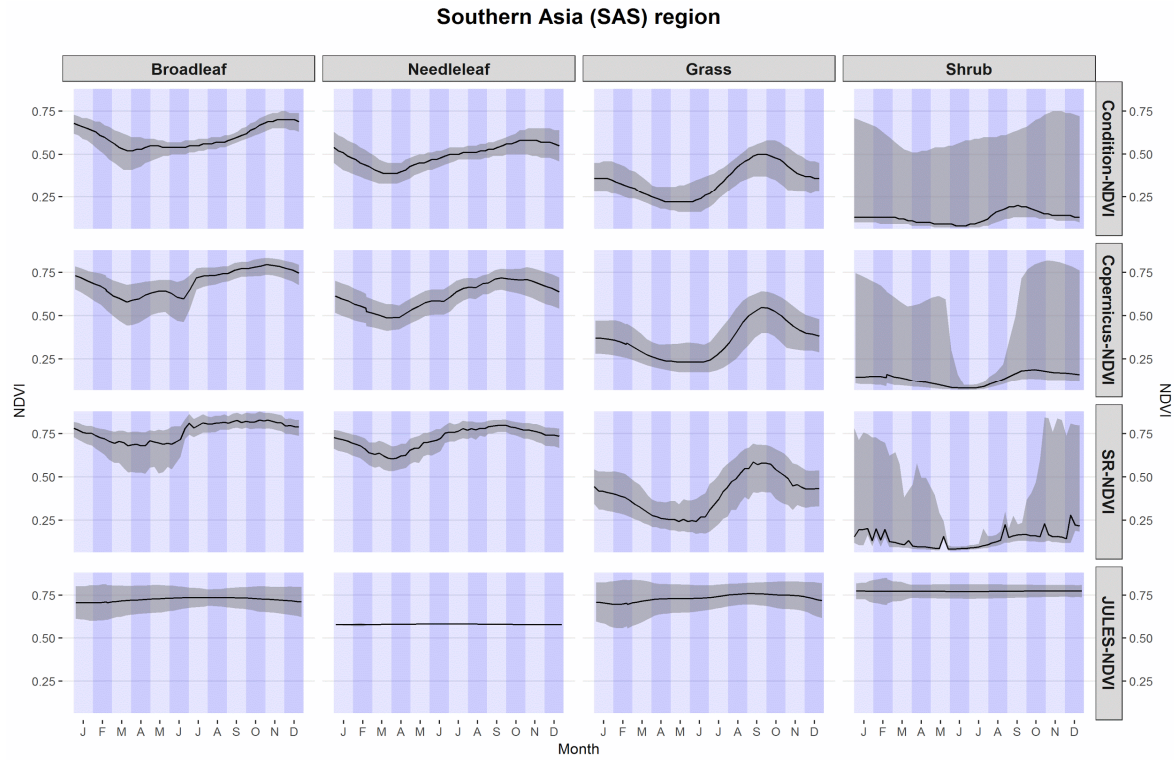


Figure 37: Southern Asian seasonal cycle for 4 plant functional types and 4 NDVI products

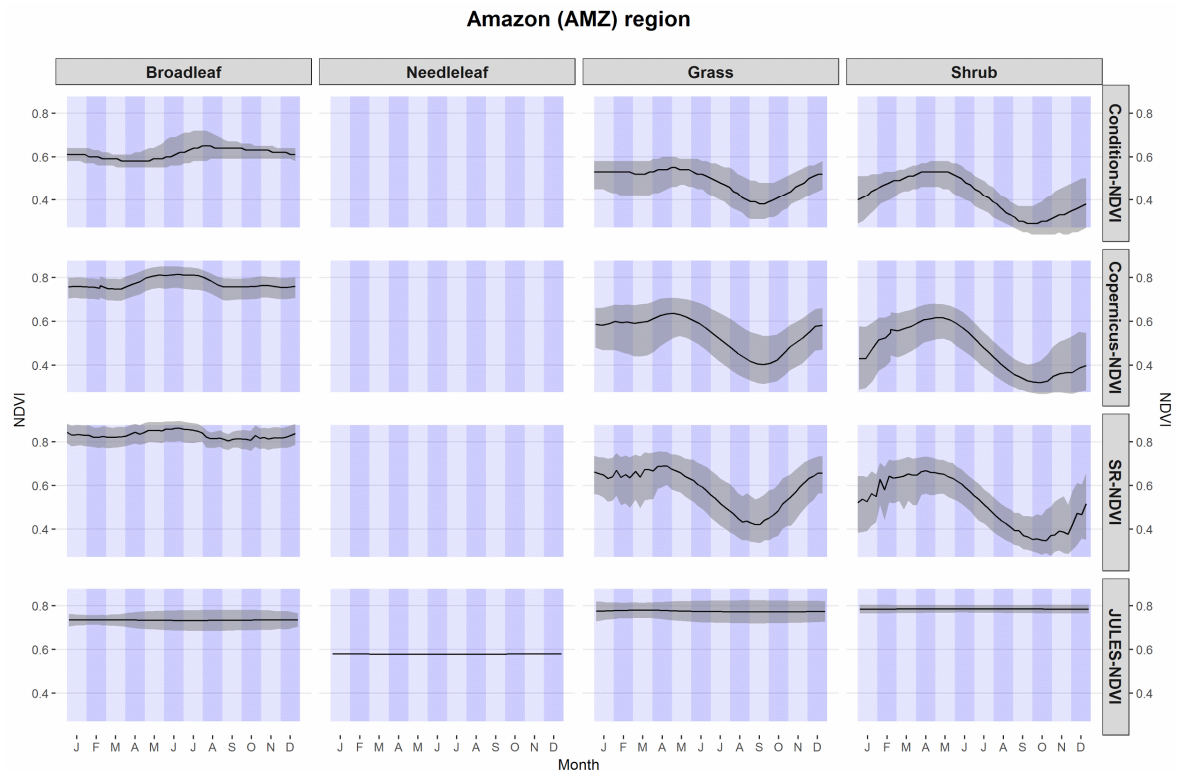


Figure 38: Amazonian seasonal cycle for 4 plant functional types and 4 NDVI products

4.3.5. Phenology Indicators

The key features highlighted in the previous section are consistent with the mapped phenological events for the Condition-NDVI and for JULES-NDVI. Due to observed caveats in the detection of seasonal indicators, this section will focus on indicators related to total permanent fraction of vegetation and the start, peak and base of season. The additional indicators (maturity, senescence, end of season, season integral, length of season and length of greenness) can be seen in Appendix MOHC - 2.

The Total Permanent Fraction (TPF) index, which reflects the minimum underlying greenness of the grid cell, is consistently higher across the tropics and southern mid-latitudes in JULES-NDVI compared to the Condition-NDVI (Figure 39). However, in the Boreal zone, JULES-NDVI is lower than Condition-NDVI.

(a)

(b)

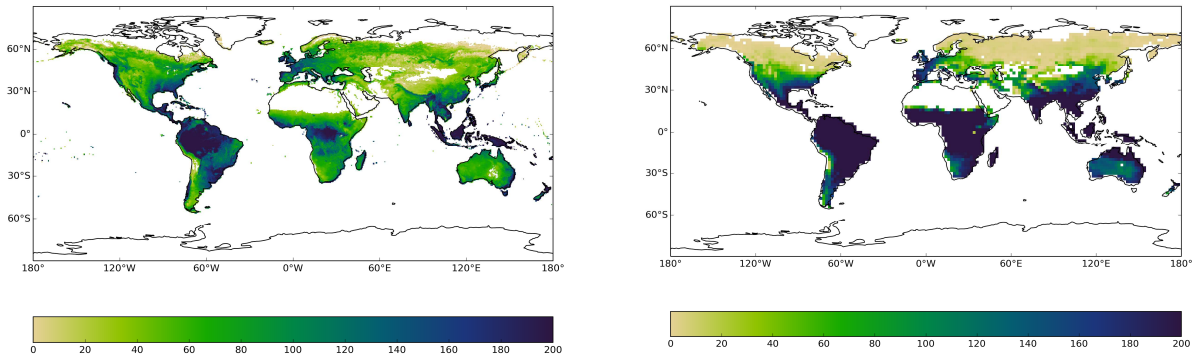


Figure 39: Comparison of (a) Condition-NDVI and (b) JULES-NDVI for TPF. Note that TPF represents integrated NDVI values over the year.

The date of Base of Season (BOS), which reflects the date of minimum NDVI (Figure 40), are broadly consistent between JULES-NDVI and Condition-NDVI across northern Europe, the USA and other Boreal regions. JULES-NDVI fails to capture the Mediterranean region Aug-Sep BOS seen in the Condition-NDVI. In other area, BOS timings in Australia appear to late in the north and too early in the south of the country in JULES. In the Amazon river basin, JULES-NDVI suggest BOS is reached approximately 1-2 months late compared to Condition-NDVI.

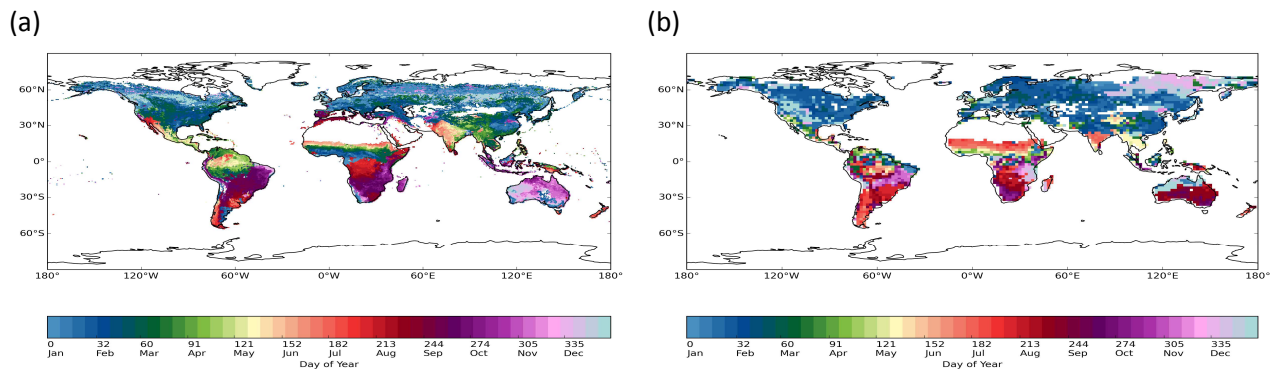


Figure 40: Comparison of (a) Condition-NDVI and (b) JULES-NDVI for Base of Season (BOS)

Start of Season (SOS), which reflects the start of vegetation green-up (Figure 41), shows reasonable large-scale consistency between JULES-NDVI and Condition-NDVI. In temperate regions (such as Europe and southern Australia) JULES-NDVI seems to be approximately 1-2 months earlier than the Condition-NDVI. Areas that show considerable disagreement in the timing of SOS between JULES-NDVI and Condition-NDVI are similar to those seen for BOS (Fig R3). In particular, this can be seen in the Mediterranean region (as with BOS), and Southwestern North America, where the SOS occurs between August-October in the Condition-NDVI, but between February to March in the JULES-NDVI.

(a) (b)

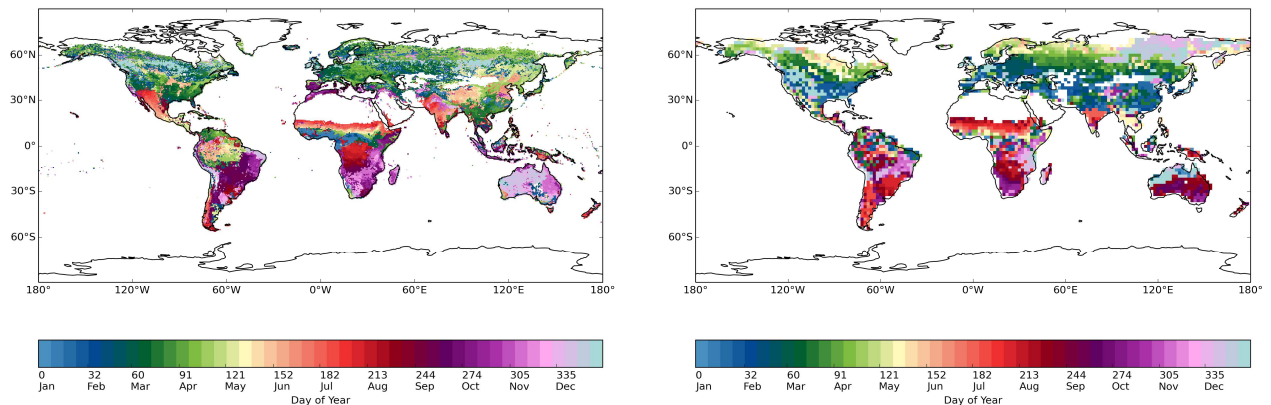


Figure 41. Comparison of (a) Condition-NDVI and (b) JULES-NDVI for Start of Season (SOS)

Peak of Season (POS), reflecting the date of maximum NDVI (Figure 42), shows broad consistency between Condition-NDVI and JULES-NDVI in terms of seasonal timing in the northern and southern hemispheres. Again, an exception to this is found to be in Mediterranean climates in locations such as Spain, California, Southern Australia and South Africa. In these locations, the peak of season in the Condition-NDVI occurs much earlier (by 4-6 months) than in JULES-NDVI; this likely reflects the effect of moisture stress limiting growth in these regions which is not captured in JULES. Tropical regions appear to have a poor consistency between Condition-NDVI and JULES-NDVI. Across the temperate and boreal zones in the Northern Hemisphere, POS in JULES-NDVI is 1-2 months later than in the Condition-NDVI. In these locations, Condition-NDVI also exhibits a stronger South-North gradient in the date of POS than in JULES-NDVI.

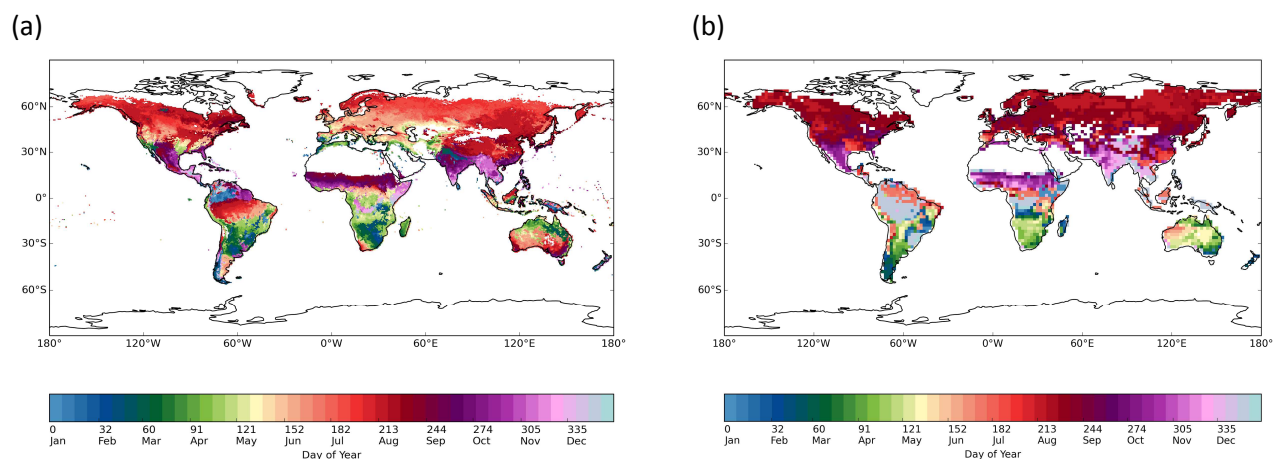


Figure 42. Comparison of (a) Condition-NDVI and (b) JULES-NDVI for Peak of Season (POS).

4.3.6. Caveats to the detection of indicators

Several issues with the algorithms for detecting seasonal indicators have been observed. In particular, some regions, especially in agricultural areas, multiple peaks are found within the growing season that confuse the algorithm for detection of senescence (Se) and end of season (EOS) (for an example over East Anglia, see Figure 43). Such behaviour is not observed with

JULES-NDVI, and may indicate that different cropping regimes affect the satellite observations, while JULES does not capture these complexities.

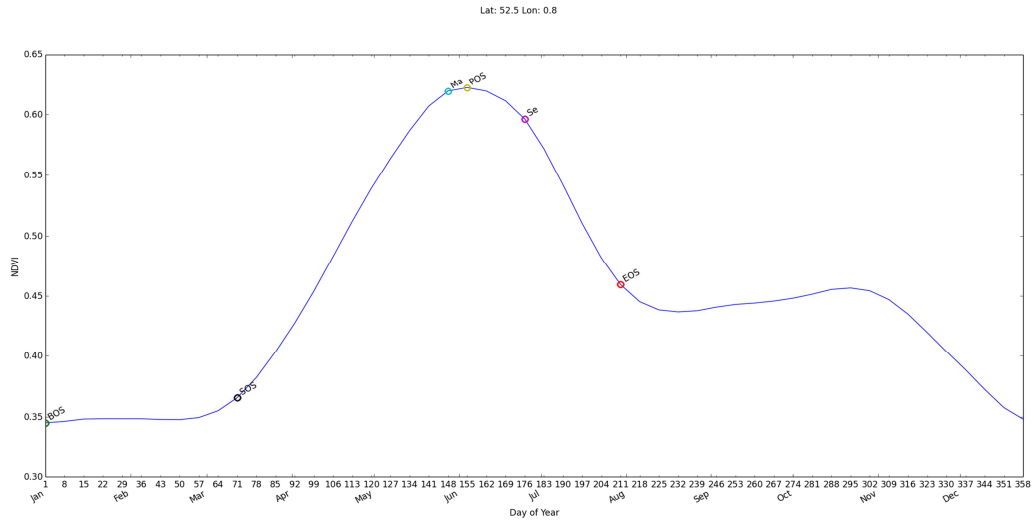


Figure 43. Example phenological series for the Condition-NDVI from a rural location in East Anglia (52.5N 0.8W) showing incorrect identification of senescence (Se) and end-of-season (EOS) dates. Dates of each of the indicators are indicated by a coloured circle.

In other instances, JULES significantly underestimates the range of NDVI values and produces a phenology series with an unclear or non-existent seasonal cycle. Figure 44 shows a comparison between JULES-NDVI and Condition-NDVI for a location on the edge of the Amazon basin. In this case, the JULES simulated NDVI has a range of < 0.001.

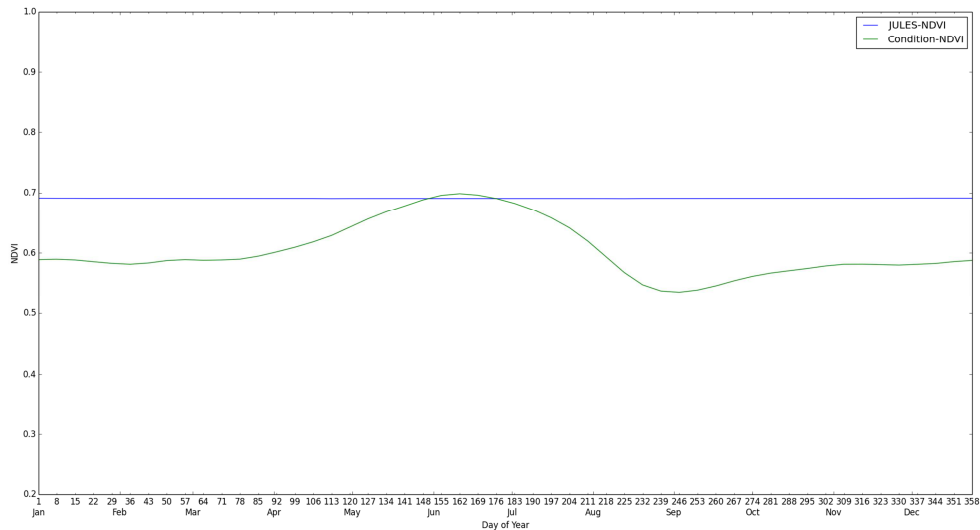


Figure 44. Comparison of JULES-NDVI (blue line) and Condition-NDVI (green line) for a location on the edge of the amazon basin (-9.69N, -63.24W).

	Ref	LC CCI Phase 2: Climate Assessment Report, Year 3		
	Issue	1.0	Date 2017-07-11	
	Page	69		

4.4. Significance of results

The results highlight some serious deficiencies in modelling vegetation seasonality in JULES for some locations. While these deficiencies were previously known, the scale of the problem has not previously been described in such detail. Although JULES seems to perform quite well when there is a clear temperature based seasonal cycle, no phenological variation is seen at all in the tropics. The radiation scheme of JULES has user-defined upper limits for the amount of radiation a particular PFT can reflect in the shortwave, which clearly affects the modelled NDVI values. This causes a plateau in many of the time-series that would give an artificial early onset of peak of season and late onset of season decline.

We also found large uncertainty in the satellite-derived NDVI, although this is still not on the same magnitude as found in JULES. The principle driver of the observation-based uncertainty was due to large data gaps, particularly in the SR-NDVI. This means that it is not feasible to use the SR-NDVI for ESM evaluation in many parts of the world. However, the potential for using gap filling methods to examine model performance at large spatial scales (see Figure 33 and Figure 34) revealed some potential. From the example of Northern Europe, it appears that even the SR-NDVI still exhibits useful characteristics when aggregated over a region of 140km or greater. In contrast, the Copernicus-NDVI has less data gaps even for 3km aggregation areas, but crucially, there appears to be more noise in the time series. Given the differences between the observations at higher resolutions, and the much coarser spatial resolution of the model data, it would therefore appear that further evaluation work should focus on aggregation of PFTs at the scale of Giorgi regions. This would ensure a consistent time series with limited data gaps, whilst still allowing for variations in the seasonal cycle of different PFTs.

We found that seasonal indicators are useful measures to extract from the NDVI Condition because it doesn't have the same problems of data gaps, but it does appear to underestimate peak NDVI compared to the SR-NDVI and Copernicus NDVI products. This is perhaps due to the spatial and temporal averaging that is used in the preparation of the NDVI Condition product.

This work has also shown the value of using seasonal indicators to evaluate models. A common problem in the evaluation of land surface models with satellite data is the potential lack of consistency between products that are based on remotely sensed radiances, and modelled output that typically is based on simulations of plant physiology. We have shown that using the simulated shortwave reflectance to calculate simulated NDVI has potential to identify areas where models should be improved. The advantages of such an approach is that the evaluation is apparently less influenced by differences between LAI from the model and NDVI from satellite, although further work should be done to understand the limitations of simulated NDVI. One such area for further investigation would be to understand why the simulated NDVI shows no seasonal variation in the tropics (e.g. Figure 37 and Figure 38).

4.5. Conclusions and recommendations

We have shown that observed values of NDVI vary between datasets depending on the satellite sensor and differing methods of atmospheric corrections. We recommend that these data are used to compare relative changes and seasonal timings relative to each PFT used in JULES. Specifically, following this report, we recommend the following actions:

	Ref	LC CCI Phase 2: Climate Assessment Report, Year 3		
	Issue	1.0	Date 2017-07-11	
	Page	70		

- Multiple satellite datasets need to be used to evaluate earth system or land surface model performance.
- Spatial aggregation of satellite time series should be explored for different parts of the world, and compared to the results presented here for Northern Europe.
- Analysing the seasonal cycle of vegetation by PFT by Giorgi region seems to be a reasonable compromise between observational uncertainties, and model resolution.
- Evaluation of models using seasonal indicators is an approach that can be used to evaluate the key seasonal characteristics of models.
- Further work is recommended to understand large discrepancies between JULES and NDVI observations, notably in the Tropics and Mediterranean regions.

	Ref	LC CCI Phase 2: Climate Assessment Report, Year 3		
	Issue	1.0	Date 2017-07-11	
	Page	71		

5. INTERCOMPARISON OF CLIMATE MODELLERS' PRODUCT ASSESSMENT

Authors: **Goran Georgievski, Stefan Hagemann, Catherine Ottlé, Philippe Peylin, Vladislav Bastrikov, Andrew Hartley**

5.1. Introduction

Given large differences between land surface models in terms of both the number and nature of the processes that are encapsulated and the parameter values, their response to land cover changes are substantially different. Moreover the internal variability of climate models in addition to well-known biases in precipitation and climate variability affect our ability to interpret the impacts of land use change in coupled land-atmosphere climate models. In this context we have continue our effort to assess the potential of the new ESA-CCI land cover product, and in particular the potential of the annual land cover changes recently produced.

Hartley et al (2017) during the previous phase of the project investigated the impact of the range of uncertainty due to satellite derived LC mapping and its impact on the sensitivity of energy balance, hydrological and carbon cycle with the 3 land surface models (ORCHIDEE, JSBACH, JULES). According to their definition of uncertainty they found that the maximal plausible range of LC uncertainty is about the same order of magnitude, or even larger than the range of the recent LC change. For example, according to Ramankutty and Foley (1999) approximately 1200 Mha of trees have been removed globally since 1700 up to 1992 and based on ESA-CCI-LC map for epoch 2010, Hartley et al (2017), estimated that in the case of extremely large uncertainty there could be 1740 Mha fewer trees than in their reference case. In this joint study (between the 3 climate modeling groups) the sensitivity of energy, water and carbon cycle as represented by three LSM (JSBACH, JULES, ORCHIDEE) to the satellite-borne LC change maps (for period 1992-2013) has been investigated. In the first section the newly derived dataset in the frame of the project ESA-CCI-LC project representing LC change from 1992-2015 is described, as well as the experimental protocol used. We then discuss the results in terms of energy, water and carbon fluxes and we then draw some perspectives to this first investigation.

5.2. Protocol for the model inter-comparison

5.2.2. Initial data - LCC maps

In the frame of the ESA-CCI-LC project maps showing annual change of Land Cover (LC) are derived. This is to our best knowledge the first product based on the remote sensing imagery at 300 m resolution. At the time of preparing this report ESA-CCI-LC change maps were available for period 1992-2014. However, climatological forcing was available up to year 2013. Therefore, our

analysis of spatial pattern changes are made for period 1992 – 2013, but we also analyzed the annual time series for the period 1992 – 2014. The LC maps are aggregated at 0.5 degree resolution. Figure 45, shows the differences in area fraction between year 2013 and 1992, and Figure 46 shows the global annual change of the major vegetation and land cover types for the period 1992 – 2014. The major vegetation types are trees, shrubs, grass and crops. Both, trees and shrubs comprising of the following phenology types: evergreen broadleaf, deciduous broadleaf, evergreen broadleaf and deciduous needleleaf.

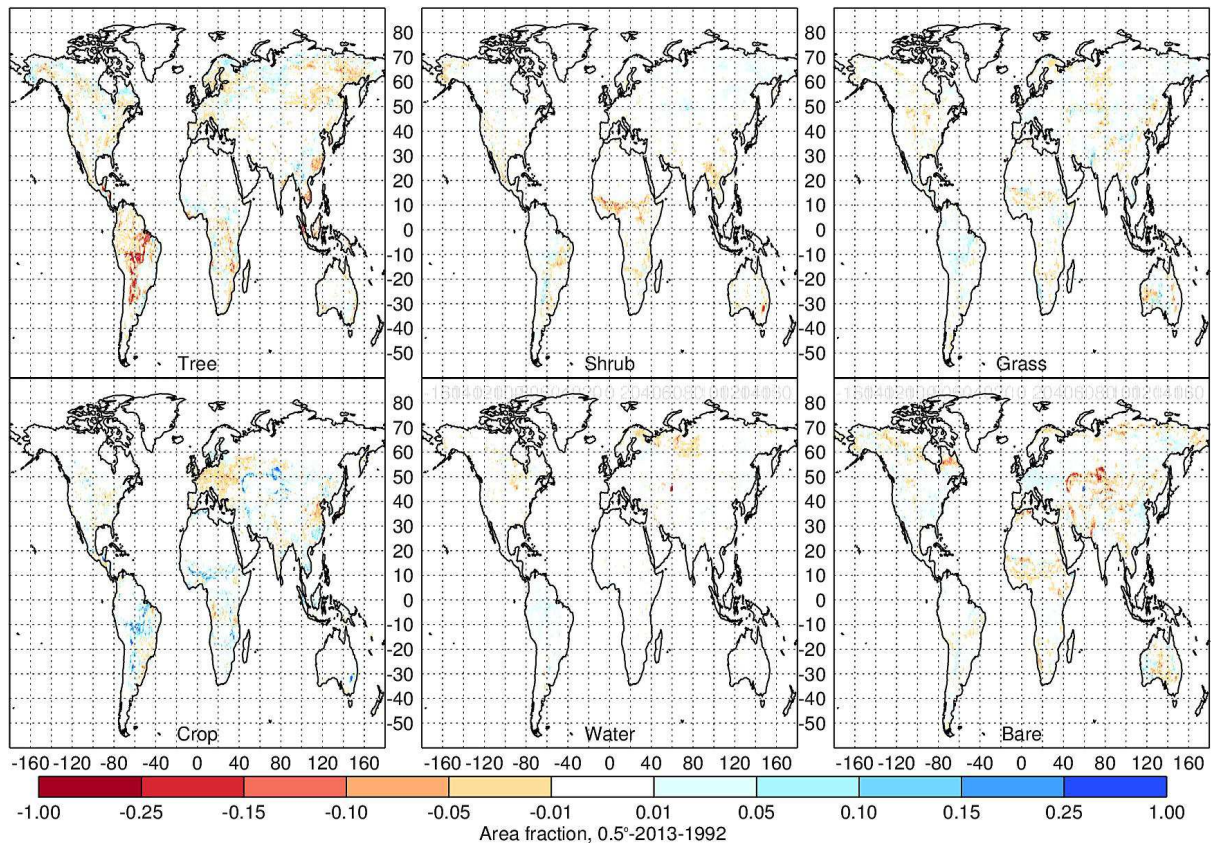


Figure 45: Differences in area fraction between year 2013 and 1992, for the major vegetation and land cover types.

Figure 46 clearly shows that dominant change on the Earth's LC is the forest replacement with agriculture, but also increase of the grass covered area and decreases of shrubs and bare areas. The global forest area is decreased for about 62 Mha, shrubs for about 20 Mha, bare area for about 6 Mha, and water bodies shrunk for about 2 Mha, while the global agricultural and grass area is increased for about 72 Mha and 18 Mha, respectively. Major transitions of LC types are shown on Figure 47. Major transitions shown on Figure 47 are defined for the grid points in which area fraction changes from initial year 1992 to 2013 are bigger than 0.01. The name of the transition is given according to the largest area fraction present in the initial year (1992) replaced with the largest area of LC type in the final year (2013).

Global Land Cover change

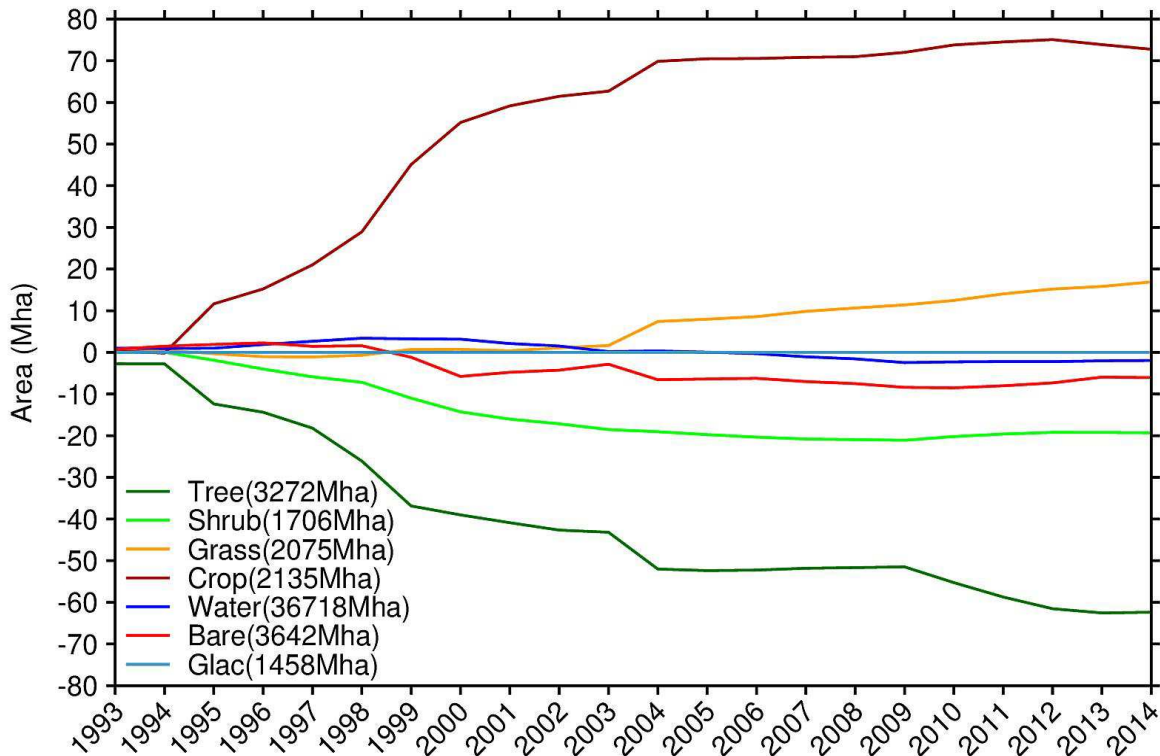


Figure 46: Annual change of area covered with the major vegetation and land cover types. Number in brackets indicate initial area in the year 1992.

Twelve regions are identified where these major transitions occur and all transitions for those regions have been quantified on the Figure 48 and Figure 49. Transitions from tree to crops (blue marked area on the Figure 47, panel Tree) happened mostly in the tropical rainforests of South America, Africa and Indonesia, but as well as along the Chines and the Baltic Seas' coasts (South America and Africa2 regions on Figure 49 and region China on Figure 48).

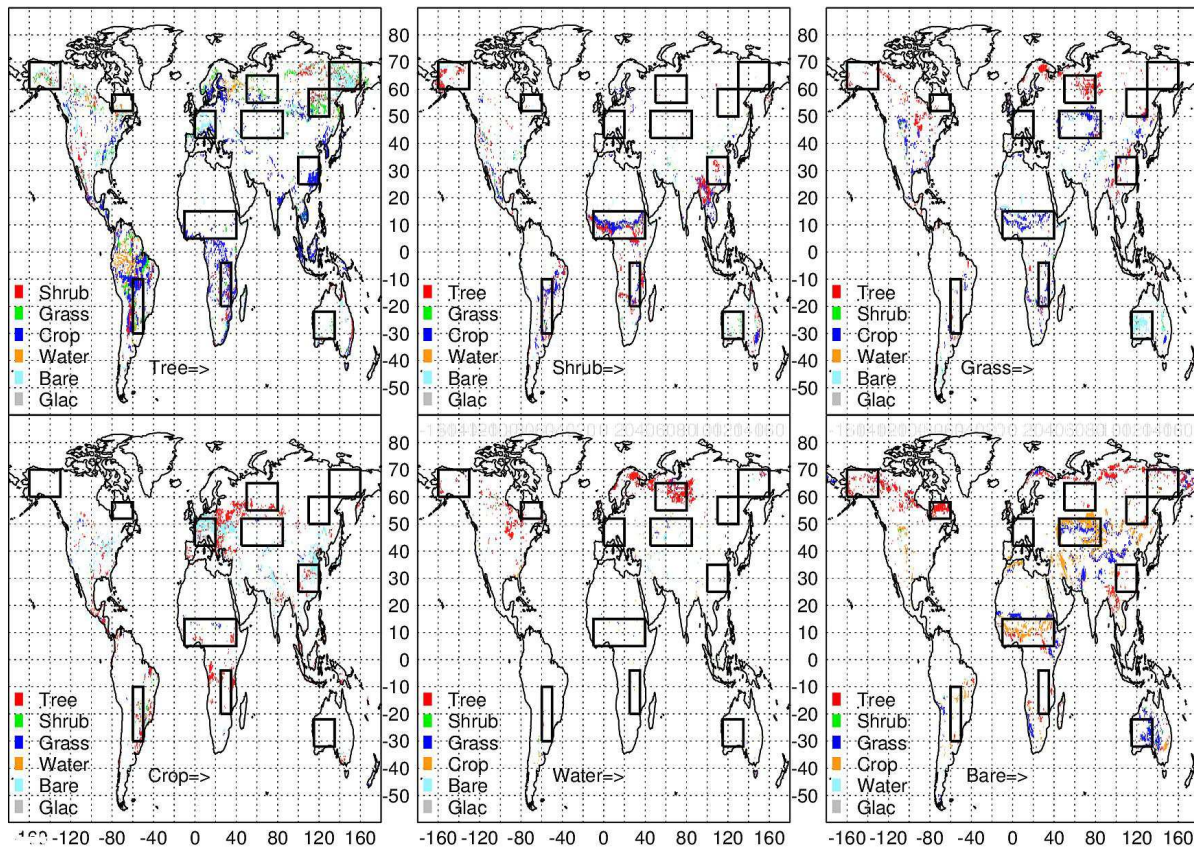


Figure 47: Major transitions of the land cover types from year 1992 to 2013. Regions of interest in which major transitions occur are also indicated.

Forest transition into the grass and bare area occurred in Siberia and mostly in the Eastern Siberia (Figure 48, Rus2 region). The Europe is characterized with some trees transition into the bare area (Figure 48, Europe), but this transition can also be spotted in the North America. Shrubs replacement with agriculture is the major transition of Sub Saharan savannas (Figure 47, panel Shrub and Figure 49, region Africa1). There have been also some shrubs replaced with the forests. Shrubs to tree transition can also be spotted in Alaska (Figure 49, Alaska region) and southeast from Himalaya in Burma and China. In Sub Saharan savannas (Figure 49, Africa2) and Kazakh steppes (Figure 48, Kazakh) transition of grass into crops occurs as well (Figure 47, panel Grass). Grass transition into trees occurs in Russia, between Ural Mountain and West Siberia (Figure 48, Rus1).

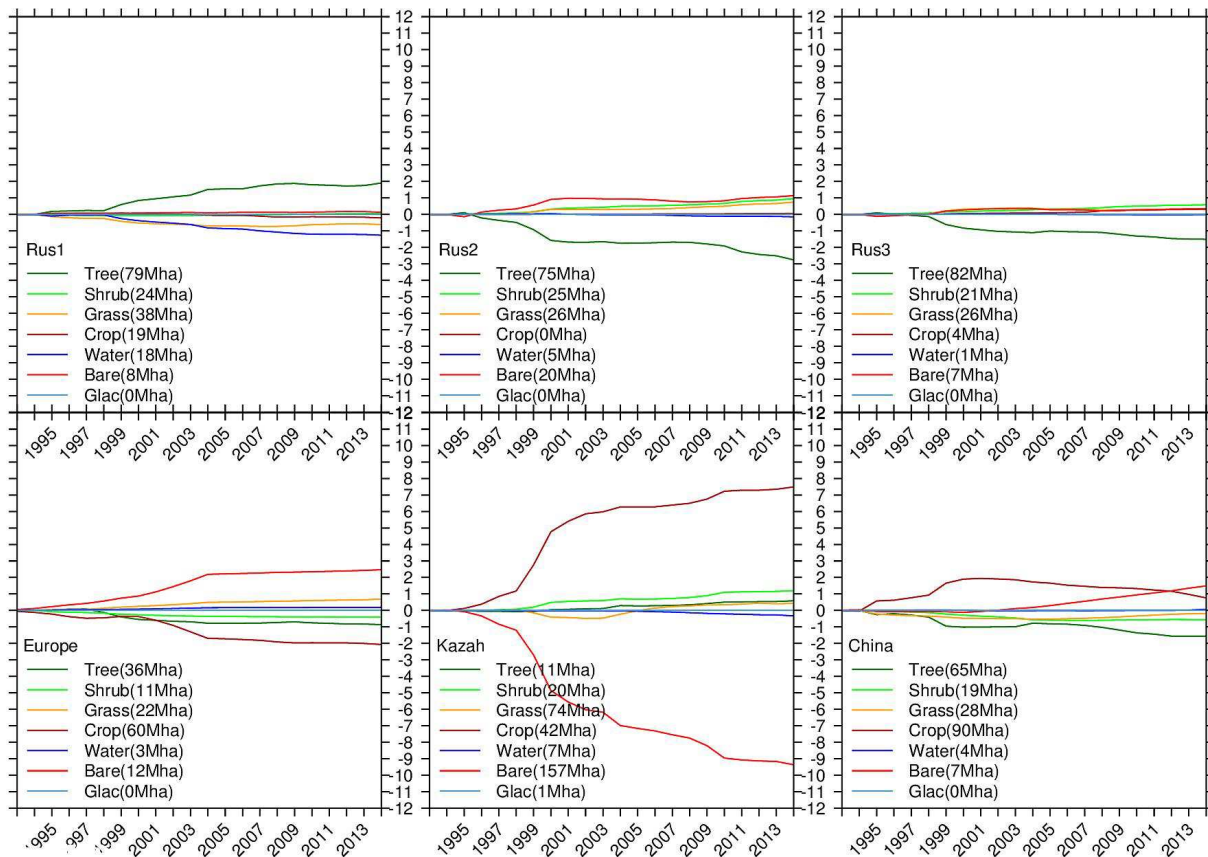


Figure 48: Annual change of area covered with the major vegetation and land cover types, for regions as indicated in Figure 47. Numbers in brackets indicate initial area in the year 1992.

In Western Australia grass is replaced with the bare area (Figure 49, Australia). In some parts of the World, mostly in Europe agriculture is replaced with forests and bare area (Figure 47, panel Crop). In northern Europe from North Scandinavia to West Siberia some inland water bodies have been replaced with trees (Figure 47, panel Water). Bare area of the high northern latitudes have been replaced with trees, Quebec is region identified to investigate that transition into more detail (Figure 47, panel Bare and Figure 49, Quebec region). In Sub Saharan Africa and Kazakh steppe bare areas have been replaced with the agriculture, while in Australia bare areas have been replaced by grass.

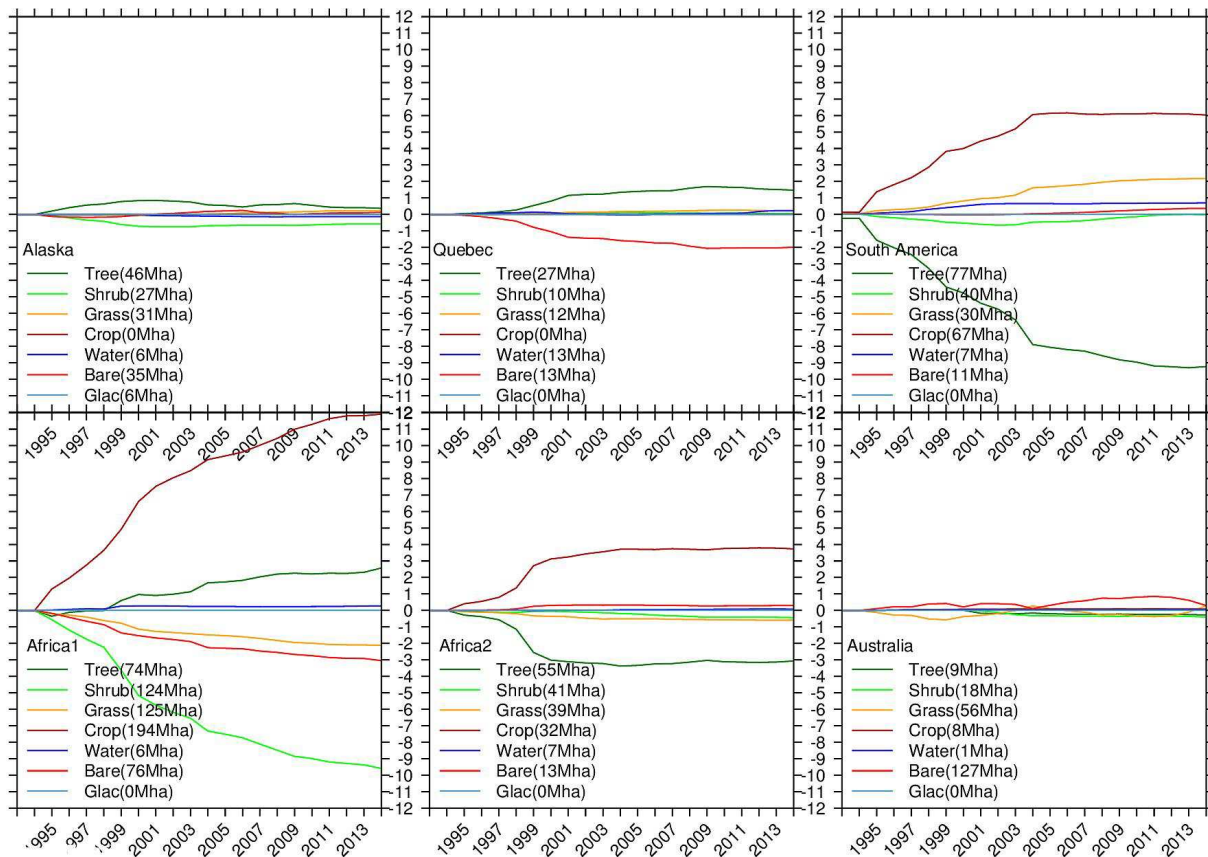


Figure 49: Annual change of area covered with the major vegetation and land cover types, for regions as indicated in Figure 47. Numbers in brackets indicate initial area in the year 1992.

5.2.3. Experimental Set up

Climate Forcing:

In order to compare the different climate simulations with the three models (ORCHIDEE, JSBACH and JULES) we choose in this first experiment to use the same climate forcing for each model run in “forced mode” (by opposition to the “coupled mode” when the land surface model are coupled to a general circulation model). Like for the previous ensemble of experiments (Hartley et al. 2017) we used the WFDEI-GPCC (WATCH Forcing Data methodology applied to ERA-Interim data) meteorological forcing data developed by [Weedon et al., 2011, 2014]. WFDEI-GPCC forcing used the precipitation from GPCC to correct the model re-analysis. The data were used at the native 0.5° spatial resolution and comprise: precipitation, temperature, wind, downwards shortwave and longwave radiation fluxes and pressure. Both JULES and ORCHIDEE use the data in their original 3h temporal resolution, while JSBACH makes use of the data accumulated to daily intervals.

	Ref	LC CCI Phase 2: Climate Assessment Report, Year 3		
	Issue	1.0	Date 2017-07-11	
	Page	77		

Ancillary data:

The same atmospheric CO₂ record was prescribed for these simulations using the observed trend over the simulation period. The other ancillary data, like soil texture maps or vegetation properties (albedo, ...) were not standardized across the different models.

Resolution, simulation period and spin-up:

We choose to run at 0.5 degrees resolution, which is currently the highest easily affordable resolution for global run. The analysis period was chosen as 1992-2014, the period for which the annual land cover changes are available. The spin-up of the carbon (and water pools) was not standardized for these first simulations. Given that not all groups will do a long (multi-centennial) spin-up to bring the soil carbon pool into equilibrium, we will not investigate the net carbon fluxes in the following analysis.

Experiments:

2 offline simulations, differing in the land cover that is imposed to the models were conducted with the following characteristics:

1. A reference simulation with the land cover kept constant each year following the map derived for the year 1992 (referred as “ref”).
2. A land cover change simulation (referred as “lcc”) with the annual map for the CCI_LC product prescribed each year to the model (period 1992 to 2014).

The reference simulations will be used to estimate the impact of the land cover changes only on the simulated energy, water and carbon fluxes (making the difference between the lcc and ref simulations).

5.2.4. Valorization of the results with an interactive web site

As explained in section 2 (the LSCE contribution), the results from the three model simulations are displayed through a common web site in order to facilitate their comparison between and to evaluate if the impact of the annual land cover changes is significantly different between the models. The site is: https://orchidas.lsce.ipsl.fr/dev/LCCCI_sims.php

We recall that the web-site offers two capabilities:

- A mapping facility for water, carbon and energy fluxes with different temporal averages and the possibility to visualize the difference between the “lcc” and the “ref” cases.
- A time series facility with aggregated quantities for an ensemble of pre-defined regions and different temporal averages.

5.3. Regional to continental scale results

5.3.2. Method

The analysis of the LCC impacts was performed at global and at regional scales, focusing on the 12 different regions described previously. We present here the results obtained on 4 of these regions where the LCC impacts appear the most significant. These regions are presented in Figure 50 and are named Europe, Africa2, Latin America and China, in the following analysis.

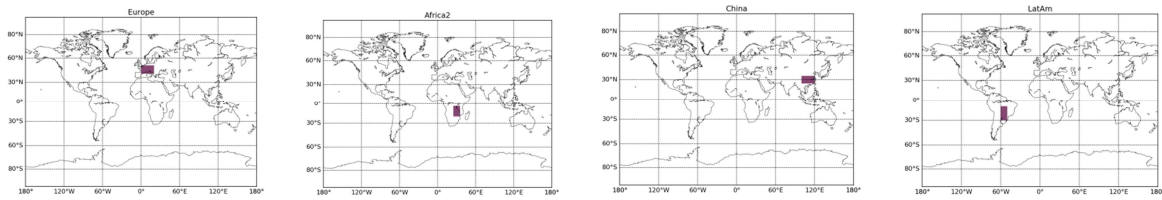


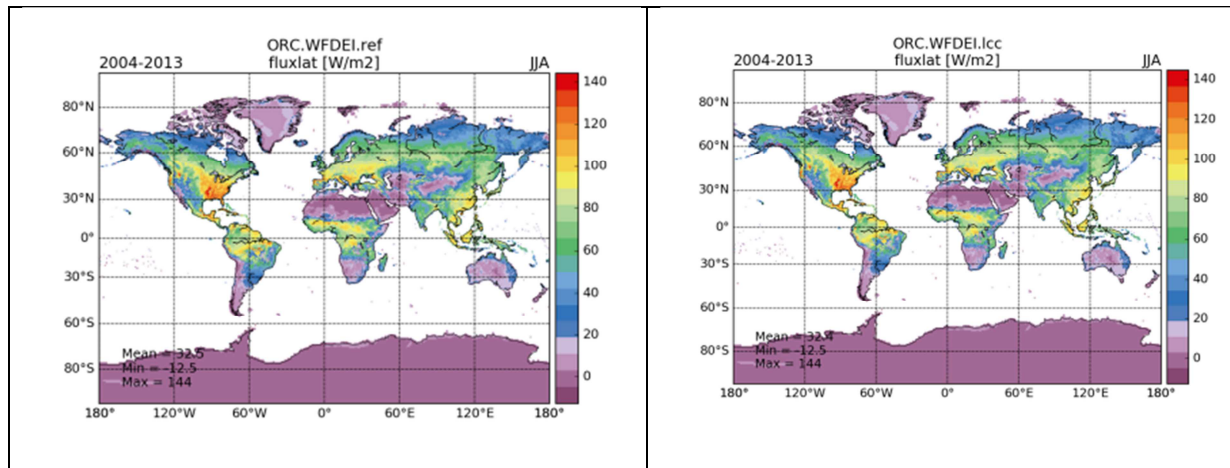
Figure 50: Regions highlighted for the analysis of the LCC impacts on water, carbon and energy budgets

In this section, we compared 4 simulations generated with ORCHIDEE and JSBACH forced with the same atmospheric forcing (WFDE-GPCC) and the same land cover maps derived in this project, i.e., a “ref” simulation using only the static land cover map of Year 1992 and a “lcc” simulation using annual maps from 1992 to 2013. We analyzed the 10 last years of the simulations to insure model equilibrium for the hydrological processes. All the results are displayed on the web site https://orchidas.lsce.ipsl.fr/dev/LCCCI_sims.php and we discuss here the most significant ones.

Note that the simulations with JULES are still under completion and that the results with this model will thus only be added to the web-site before the end of the project.

5.3.3. Energy and Water budget

If we look to the energy budgets variables at annual and global scale, it is clear that the contribution of the annual LC maps (simulations named "ORC.WFDEI-lcc" and "JSBACH.WFDEI-lcc") is very little. Even if we focus the comparison on the summer period (June-July-August months), as plotted in Figure 51 for the latent heat flux), the surface fluxes present the same patterns and same values. These differences are indeed much lower than the differences obtained between the 2 land surface models, ORCHIDEE and JSBACH.



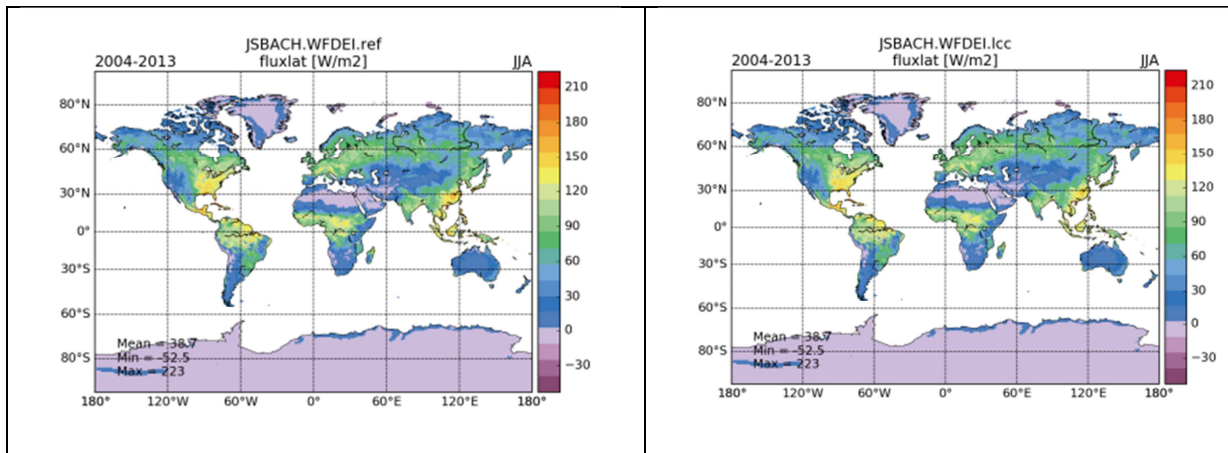
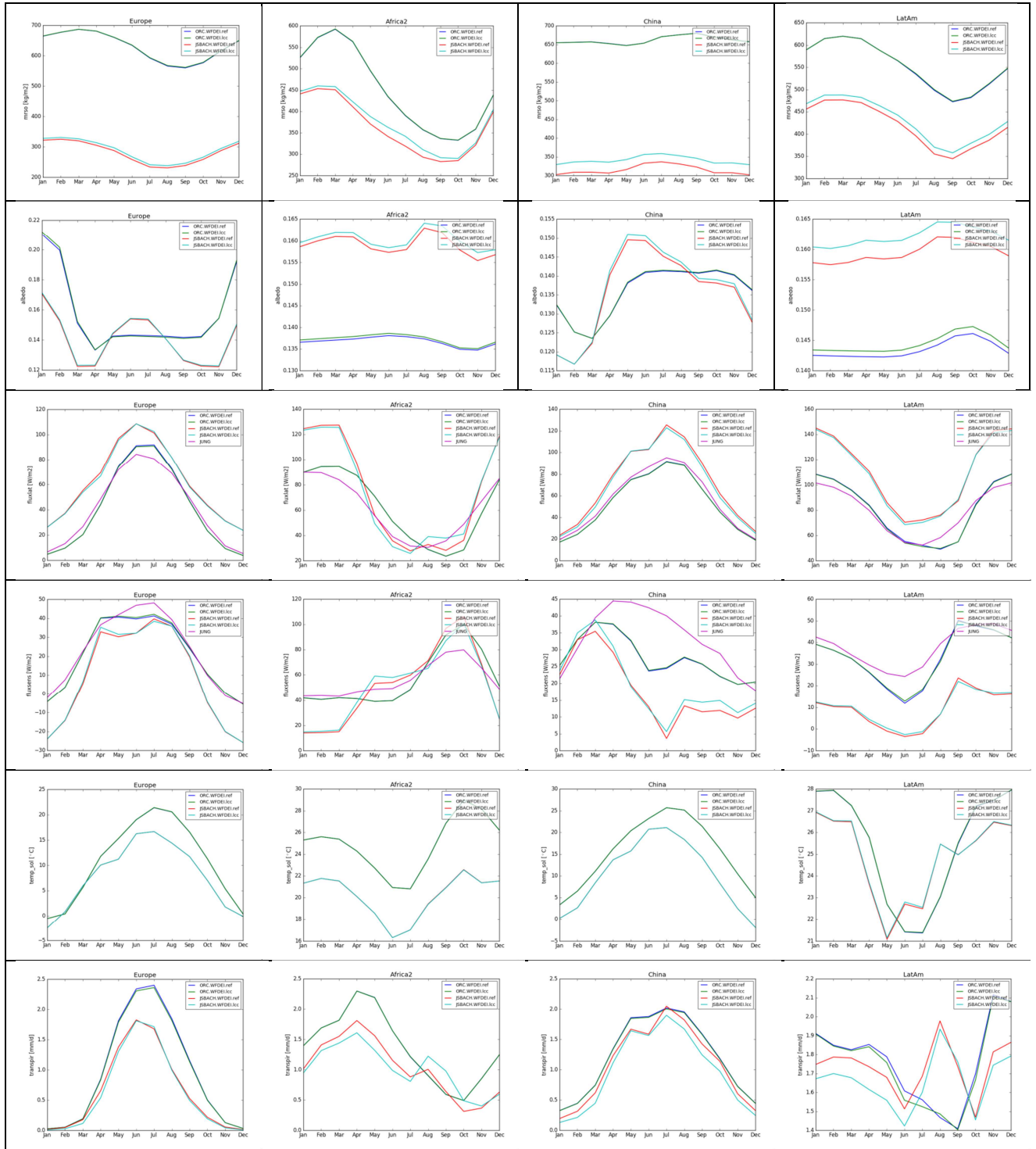


Figure 51: Summer latent heat fluxes simulated by ORCHIDEE and JSBACH for the 2 cases: prescribed LC of Year 1992 (ref subscript) and prescribed annual LC (lcc subscript)

A regional analysis in few zones defined previously (where we have identified large LC changes), shows more interesting results. Figure 52 displays the average seasonal cycles of various energy water and carbon variables calculated in the four simulations and compared to observations (i.e., data driven product) when available. Note that the web-site offers better viewing facilities to visualize more precisely the relatively small effects that are obtained: https://orchidas.lsce.ipsl.fr/dev/LCCCCI_sims.php. The plots of total soil moisture, albedo, latent and sensible heat fluxes, soil temperature, soil evaporation and transpiration, GPP and LAI, extracted for the Europe, Africa2, China and Latin America zones, show the following major results (:

- JSBACH model shows a larger sensitivity to LCC compared to ORCHIDEE;
- Model parametrizations induce larger impacts than LC map inputs;
- Seasonal cycles are correctly reproduced compared to the “observations”;
- LCC has relatively small impacts on the total energy fluxes (latent and sensibly fluxes) but impacts more the individual components (such as transpiration);
- The two models presents very different partitioning of the evapotranspiration

This last point explains indeed the larger sensitivity of JSBACH to LCC. If we consider the main two components of the evapotranspiration, which are the soil evaporation and the transpiration, we can see that JSBACH simulates larger values for soil evaporation and lower transpiration compared to ORCHIDEE. As an example, for the 4 regions selected, the Transpiration/Soil evaporation ratio is ranging between 2 and 3 in JSBACH, whereas it ranges between 7 and 15 with ORCHIDEE. Given that the LAI values in the 2 models are about the same, we can say that these 2 components are more balanced in JSBACH. Therefore, PFT changes like transitions between forests and crops or between grassland and bare soil will have much more impacts in JSBACH compared to ORCHIDEE.



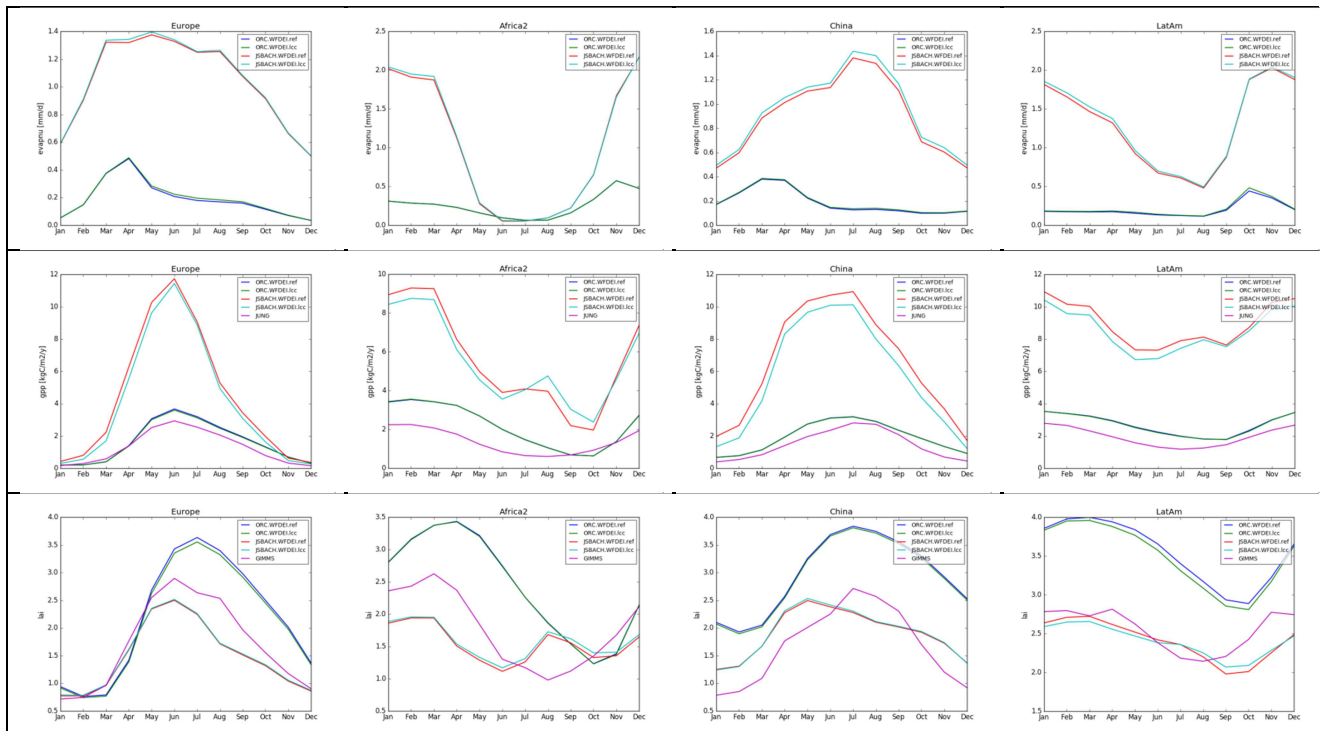


Figure 52: Energy, carbon and water variables simulated by ORCHIDEE and JSBACH for the 2 cases: prescribed LC of Year 1992 (ref subscript) and prescribed annual LC (lcc subscript) and for the 4 regions studied: Europe, Africa2, China and Latin America.

5.4. Perspectives

5.4.2. Impact of land cover change at local scale

The above analysis revealed a small impact of the annual land cover changes at regional scale (i.e. for regions of several 10.000 km²) on the energy, water and carbon fluxes simulated by ORCHIDEE and JSBACH. Given that the percentage of land cover change at this resolution is rather small, we are further investigating the impact of the LCC at the pixel level. For a given land cover transition (i.e., forest to cropland), we will select all pixels at 0.5 degrees from the current simulations that include such transition (i.e. where the transition occurred during the period 1992-2015). We will define several threshold values for the percentage of the grid cell surface that is concerned by the transition. The objective is to plot the differences for the major climate variables (surface temperature, water and carbon fluxes) between the simulation with land cover changes and the simulation using the land cover of 1992 for all years, as a function of this threshold (i.e. the magnitude of the transition in the grid cells). These diagnostics should highlight more clearly the potential of LC changes with the current model simulations (at 0.5 degrees).

Such analysis could not be performed for this Climate Assessment Report but will be completed before the end of the project.

	Ref	LC CCI Phase 2: Climate Assessment Report, Year 3		
	Issue	1.0	Date 2017-07-11	
	Page	82		

5.4.3. Opportunities to exploit high resolution land cover and land cover change maps

As the Sentinel 2 constellation becomes established and is expected to provide very high spatial resolution observations of the order of 20-30 metres, the challenge for weather and climate scientists is to demonstrate clearly the benefits of this improved information on weather and climate information. At the same time as satellite observations and derived products are improving, so too are weather and climate models. One area of model development has been to add greater complexity to coarse resolution models such that they are becoming models of the whole earth system, as opposed to merely climate. Another area of model development that builds on advances in supercomputing concerns a move towards very high resolution simulations at grid resolutions of 1 to 5 km. These models are able to resolve the processes that cause convective rainfall, and therefore offer an opportunity to realistically simulate fluxes of heat and moisture at resolutions approaching those of satellite observations. As such, there are 4 key areas of research that we suggest could be further developed with high resolution land cover.

1. **Improving Coarse Resolution Climate Simulations.** While the spatial resolution of these simulations would still remain of the order of 50-100 km, we would expect that high resolution land cover could advise improvements in our understanding of PFT fractions within the more detailed land cover classes found in the LC_CCI Phase 2 300 m products. This may include, for example, information about forest degradation (which can affect carbon storage), the roughness of the vegetation canopy (which can affect heat and moisture exchanges with the atmosphere), and links between topography, land cover and soil (which may affect hydrological models).
2. **Climate impact and mitigation studies.** There is a growing interest in using climate forcing information from high resolution climate models to drive land surface models in studies that investigate the impact of different land use management strategies on regional carbon budgets. Such simulations could be done at less than 5 km spatial resolution for a large continental domain such as Africa for periods of decades. This would allow weather and climate scientists to understand the local and regional impact of land use changes for the first time. For example, some recent studies have highlighted the importance of vegetation productivity in tropical grasslands (related to year-to-year variability in rainfall) as a key driver of inter-annual variability in atmospheric carbon dioxide. Such a novel use of advances in climate models and observational products could provide new insight into land use impacts on hydro-climate.
3. **High resolution weather and climate modelling.** In developing these new modelling approaches, new challenges and questions arise that could be best tackled through collaborations between land cover and weather/climate scientists. As well as improving our understanding of PFT fractional cover (as described above), we may also be able to consider improving our understanding of other physical properties of the land surface, such as canopy height, surface roughness, or urban morphology. The availability of other satellite observations such as albedo, FaPAR, fire, and surface soil moisture would also allow us to better analyse biases in models and target improvements in model parameterisations. Over the next few years, most large modelling centres have projects to develop completely new weather and climate models on icosahedral grids that will allow future models to be run much more efficiently at very high resolutions. This therefore highlights a significant need for high resolution land cover in the weather and climate community.

	Ref	LC CCI Phase 2: Climate Assessment Report, Year 3		
	Issue	1.0	Date 2017-07-11	
	Page	83		

4. **Locations.** It may be practical to focus efforts on improving high resolution land cover maps on certain areas of the world. While each institution will have their own preferences on location, justification for certain areas should be related to scientific need. Results from the year 2 offline uncertainty study have highlighted several locations as follows (in no particular order):
- a. Europe & North America: Cross-walking uncertainty in bare soil in the agricultural belt (extending into Russia) is particularly relevant.
 - b. SE Asia: Urban mapping (morphology of buildings), tree PFT fraction especially in Southern China. Important for simulating high impact weather impacts on populations
 - c. Africa: Shrub vs grass cover in tropical savannahs. Based on LC class uncertainty in year 2 results.
 - d. South America: Tropical savannahs are important for carbon fluxes because tropical grasses are very productive and they are very responsive to inter-annual variability in climate.
 - e. Northern high latitudes: tree PFT vs bare soil uncertainty seems to contribute most to albedo uncertainty. This may be linked to thermokarst lakes, the northern extent of the tree line, or LC mapping of wetlands.

	Ref	LC CCI Phase 2: Climate Assessment Report, Year 3		
	Issue	1.0	Date 2017-07-11	
	Page	84		

6. REFERENCES

- Alton P (2016) The sensitivity of models of gross primary productivity to meteorological and leaf area forcing: A comparison between a Penman-Monteith ecophysiological approach and the MODIS Light-Use Efficiency algorithm. *Agricultural and Forest Meteorology* 218-219: 11-24.
- Anav, A., et al. (2015), Spatiotemporal patterns of terrestrial gross primary production: A review, *Rev. Geophys.*, 53, 785–818, doi:10.1002/2015RG000483.
- Best MJ, Pryor M, Clark DB, et al. (2011) The Joint UK Land Environment Simulator (JULES), model description – Part 1: Energy and water fluxes. *Geoscientific Model Development* 4: 677-699.
- Birky AK (2001) NDVI and a simple model of deciduous forest seasonal dynamics. *Ecological Modelling* 143: 43-58.
- Bonan GB (2008) Forests and climate change: forcings, feedbacks, and the climate benefits of forests. *Science* 320:1444–1449
- Brando P, Goetz S, Baccini A, Nepstad DC, Beck PSA, Christman MC (2010) Seasonal and interannual variability of climate and vegetation indices across the Amazon. *Proceedings of the National Academy of Sciences USA* 107: 14685-14690.
- Brovkin, V., L. Boysen, V. K. Arora, J. P. Boisier, P. Cadule, L. Chini, M. Claussen, P. Friedlingstein, V. Gayler, B. J. J. M. Van Den Hurk, G. C. Hurtt, C. D. Jones, E. Kato, N. De Noblet-Ducoudré, F. Pacifico, J. Pongratz, and M. Weiss. "Effect of Anthropogenic Land-Use and Land-Cover Changes on Climate and Land Carbon Storage in CMIP5 Projections for the Twenty-First Century." *Journal of Climate* J. Climate 26.18 (2013): 6859-881.
- Brovkin, V., Raddatz, T., Reick, C. H., Claussen, M., and Gayler, V.: Global biogeophysical interactions between forest and climate, *Geophys. Res. Letters*, 36, L07 405, doi:10.1029/2009GL037543, 2009.
- Chavana-Bryant C, Malhi Y, Wu J, Asner GP, Anastasiou A, Enquist BJ, Cosio Caravasi EG, Doughty CE, Saleska SR, Martin RE, Gerard FF (2016) Leaf aging of Amazonian canopy trees as revealed by spectral and physiochemical measurements. *New Phytologist* doi: 10.1111/nph.13853.
- Chen JM, Pavlic G, Brown L, Cihlar J, Leblanc SG, White HP, Hall RJ, Peddle DR, King DJ, Trofymow JA, Van der Sanden JJ, Pellikka PKE, Swift DE (2002) Derivation and validation of Canada-wide coarse-resolution leaf area index maps using high-resolution satellite imagery and ground measurements. *Remote Sensing of Environment* 80: 165-184.
- Clark DB, Mercado LM, Sitch S, et al. (2011) The Joint UK Land Environment Simulator (JULES), model description – Part 2: Carbon fluxes and vegetation dynamics. *Geoscientific Model Development* 4: 701-722.
- Clerici, N., Weissteiner, C. J., & Gerard, F. (2012). Exploring the use of MODIS NDVI-based phenology indicators for classifying forest general habitat categories. *Remote Sensing*, 4(6), 1781-1803.
- Congalton, R.G.; Gu, J.; Yadav, K.; Thenkabail, P.; Ozdogan, M. Global Land Cover Mapping: A Review and Uncertainty Analysis. *Remote Sens.* 2014, 6, 12070-12093.
- Cox P., Huntingford C, Harding R. (1998) A canopy conductance and photosynthesis model for use in a GCM land surface scheme. *Journal of Hydrology* 212: 79-94.
- Curry, J. (2011), Reasoning about climate uncertainty, *Climatic Change*, 108: 723. doi:10.1007/s10584-011-0180-z

	Ref	LC CCI Phase 2: Climate Assessment Report, Year 3		
	Issue	1.0	Date 2017-07-11	
	Page	85		

- Davin, E. L. and N. de Noblet-Ducoudré, 2010: Climatic Impact of Global-Scale Deforestation: Radiative versus Nonradiative Processes. *J. Climate*, 23, 97–112, doi: 10.1175/2009JCLI3102.1.
- Druel et al., Accounting for shrubs and non-vascular plants in the ORCHIDEE land surface model to improve energy, water and carbon budgets of boreal ecosystems, GMD, in preparation
- Ellison, D., N. Futter, M. and Bishop, K. (2012), On the forest cover–water yield debate: from demand- to supply-side thinking. *Glob Change Biol*, 18: 806–820. doi:10.1111/j.1365-2486.2011.02589.x
- Essery RLH, Best MJ, Betts RA, Cox PM, Taylor CM (2003) Explicit Representation of Subgrid Heterogeneity in a GCM Land Surface Scheme. *Journal of Hydrometeorology* 4: 530-543.
- Fan L, Gao Y, Bruck H, Bernhofer Ch (2009) Investigating the relationship between NDVI and LAI in semi-arid grassland in Inner Mongolia using in-situ measurements. *Theor. Appl. Climatol.* 95: 151-156.
- Fassnacht KS, Gower ST, MacKenzie MD, Nordheim EV, Lillesand TM (1997) Estimating leaf area index of north central Wisconsin forests using the Landsat Thematic Mapper. *Remote Sensing of Environment* 61: 229-245.
- Feddema, J.J.; Oleson, K.W.; Bonan, G.B.; Mearns, L.O.; Buja, L.E.; Meehl, G.A.; Washington, W.M. The importance of land-cover change in simulating future climates. *Science* 2005, 310, 1674–1678.
- Flato, G. M. (2011), Earth system models: an overview, *WIREs Clim. Change* 2011, 2:783–800. doi: 10.1002/wcc.148.
- Forzieri G, G. Duveiller, G. Georgievski, W. Li, E. Robertson, M. Kautz, P. Lawrence, P. Clais, J. Pongratz, S. Sitch, A. Wiltshire, A. Arneth, A. Cescatti (2017) Benchmarking sensitivity of biophysical processes to leaf area changes in land surface models, submitted to the *Journal of Advances in Modeling Earth Systems*
- Ghimire, B., C. A. Williams, J. Masek, F. Gao, Z. Wang, C. Schaaf, and T. He (2014), Global albedo change and radiative cooling from anthropogenic land cover change, 1700 to 2005 based on MODIS, land use harmonization, radiative kernels, and reanalysis, *Geophys. Res. Lett.*, 41, 9087–9096, doi:10.1002/2014GL061671.
- Goldewijk, K. (2016, April). A historical land use data set for the Holocene; HYDE 3.2. In *EGU General Assembly Conference Abstracts* (Vol. 18, p. 1574).
- Goll, Daniel S., Victor Brovkin, Jari Liski, Thomas Raddatz, Tea Thum, and Kathe E. O. Todd-Brown. "Strong Dependence of CO₂ Emissions from Anthropogenic Land Cover Change on Initial Land Cover and Soil Carbon Parametrization." *Global Biogeochem. Cycles Global Biogeochemical Cycles* 29.9 (2015): 1511-523.
- Gordon, Line J., Will Steffen, Bror F. Jönsson, Carl Folke, Malin Falkenmark, and Åse Johannessen (2005), Human modification of global water vapor flows from the land surface, *PNAS* 2005 102 (21) 7612-7617; doi:10.1073/pnas.0500208102.
- Guimberteau M., et al., ORCHIDEE-MICT (revision 4126), a land surface model for the high-latitudes, gmd-2017-122, submitted on 17 May 2017.
- Hagemann, S., and Stacke, T.: Impact of the soil hydrology scheme on simulated soil moisture memory, *Climate Dyn.*, 44, 1731-1750, doi:10.1007/s00382-014-2221-6, 2015.
- Hagolle, O. ; Lobo, A. ; Maisongrande, P. ; Cabot, F. ; Duchemin, B. ; de Pereyra, A. Quality assessment and improvement of temporally composited products of remotely sensed imagery by combination of VEGETATION 1 and 2 images. *Remote Sensing of Environment* 2005, vol.94, 172-186.

	Ref	LC CCI Phase 2: Climate Assessment Report, Year 3		
	Issue	1.0	Date 2017-07-11	
	Page	86		

- Hansen, M. C., Potapov, P. V., Moore, R., Hancher, M., Turubanova, S. A., Tyukavina, A., ... & Kommareddy, A. (2013). High-resolution global maps of 21st-century forest cover change. *science*, 342(6160), 850-853.
- Harris I, Jones PD, Osborn TJ, Lister DH (2014) Updated high-resolution grids of monthly climatic observations - the CRU TS3.10 Dataset. *International Journal of Climatology* 34: 623-642.
- Hartley et al (2017): SI RSE
- He, T., S. Liang, and D. Song, (2014). Analysis of global land surface albedo climatology and spatial-temporal variation during 1981-2010 from multiple satellite products. *Journal of Geophysical Research: Atmospheres*, 119, 10281-10298, doi: 10.1002/2014JD021667
- Hermance, J. F., Jacob, R. W., Bradley, B. A., & Mustard, J. F. (2007). Extracting phenological signals from multiyear AVHRR NDVI time series: Framework for applying high-order annual splines with roughness damping. *IEEE Transactions on Geoscience and Remote Sensing*, 45(10), 3264-3276.
- Herold, N., A. Behrangi, and L. V. Alexander (2017), Large uncertainties in observed daily precipitation extremes over land, *J. Geophys. Res. Atmos.*, 122, 668–681, doi:10.1002/2016JD025842.
- Huemmerich KF (2013). Simulations of seasonal and latitudinal variations in leaf inclination angle distribution: Implications for remote sensing. *Advances in Remote Sensing* 2: 93-101.
- Huerte A, Didan K, Miura T, Rodriguez EP, Gao X, Fereira LG (2002) Overview of radiometric and biophysical performance of the MODIS vegetation indices. *Remote sensing of Environment* 83: 195-213.
- Hurt, G. C., Chini, L. P., Frohling, S., Betts, R. A., Feddema, J., Fischer, G., ... & Jones, C. D. (2011). Harmonization of land-use scenarios for the period 1500–2100: 600 years of global gridded annual land-use transitions, wood harvest, and resulting secondary lands. *Climatic change*, 109(1-2), 117.
- IPCC, 2014: *Climate Change 2014: Synthesis Report*. Contribution of Working Groups I, II and III to the Fifth Assessment Report of the Intergovernmental Panel on Climate Change [Core Writing Team, R.K. Pachauri and L.A. Meyer (eds.)]. IPCC, Geneva, Switzerland, 151 pp.
- Jones, A.D., Calvin, K.V., Collins, W.D. et al (2015), Accounting for radiative forcing from albedo change in future global land-use scenarios, *Climatic Change* (2015) 131: 691. doi:10.1007/s10584-015-1411-5.
- Jung, M., M. Reichstein, and A. Bondeau (2009). Towards global empirical upscaling of FLUXNET eddy covariance observations: Validation of a model tree ensemble approach using a biosphere model. *Biogeosciences*, 6, 2001-2013
- Jung, Martin, Mona Vetter, Martin Herold, Galina Churkina, Markus Reichstein, Soenke Zaehle, Philippe Ciais, Nicolas Viovy, Alberte Bondeau, Youmin Chen, Kristina Trusilova, Frauke Feser, and Martin Heimann. "Uncertainties of Modeling Gross Primary Productivity over Europe: A Systematic Study on the Effects of Using Different Drivers and Terrestrial Biosphere Models." *Global Biogeochem. Cycles* Global Biogeochemical Cycles 21.4 (2007).
- Kalnay E, Kanamitsu M, Kistler R, et al. (1996) The NCEP/NCAR 40-Year Reanalysis Project. *Bulletin of the American Meteorological Society* 77: 437-471.
- Kandasamy, S., Baret, F., Verger, A., Neveux, P., & Weiss, M. (2013). A comparison of methods for smoothing and gap filling time series of remote sensing observations-application to MODIS LAI products. *Biogeosciences*, 10(6), 4055-4071.

	Ref	LC CCI Phase 2: Climate Assessment Report, Year 3		
	Issue	1.0	Date 2017-07-11	
	Page	87		

- Kottek, Markus, Jürgen Grieser, Christoph Beck, Bruno Rudolf, and Franz Rubel. "World Map of the Köppen-Geiger Climate Classification Updated." *Meteorologische Zeitschrift Meteorol. Z.* 15.3 (2006): 259-63.
- LC_CCI CAR (2016). Year 2 Climate Assessment Report. On the potential application of the NDVI condition product for improving understanding of modelled Leaf Area Index (Chapter 2)
- Le Quéré C, Moriarty R, Andrew RM, Peters GP, Ciais P, Friedlingstein P, Jones SD, Sitch S, Tans P, Arneeth A, Boden TA, Bopp L, Bozec Y, Canadell JG, Chevallier F, Cosca CE, Harris I, Hoppema M, Houghton RA, House JI, Jain AK, Johannessen T, Kato E, Keeling RF, Kitidis V, Klein Goldewijk K, Koven C, Landa C, Landschützer P, Lenton A, Lima ID, Marland GH, Mathis JT, Metz N, Nojiri Y, Olsen A, Ono T, Peters W, Pfeil B, Poulter B, Raupach MR, Regnier P, Rödenbeck C, Saito S, Sailsbury JE, Schuster U, Schwinger J, Séférian R, Segsneider J, Steinhoff T, Stocker BD, Sutton AJ, Takahashi T, Tilbrook B, van der Werf GR, Viovy N, Wang YP, Wanninkhof R, Wiltshire A, Zeng N (2015) Global Carbon Budget 2014. *Earth System Science Data*, doi:10.5194/essd-7-47-2015.
- Lee, X. et al (2011), Observed increase in local cooling effect of deforestation at higher latitudes, *Nature*, <http://dx.doi.org/10.1038/nature10588>
- Loranty, M. M., Berner, L. T., Goetz, S. J., Jin, Y. and Randerson, J. T. (2014), Vegetation controls on northern high latitude snow-albedo feedback: observations and CMIP5 model simulations. *Glob Change Biol*, 20: 594–606. doi:10.1111/gcb.12391
- Loveland, T. R., Reed, B. C., Brown, J. F., Ohlen, D. O., Zhu, Z., Yang, L. W. M. J., & Merchant, J. W. (2000). Development of a global land cover characteristics database and IGBP DISCover from 1 km AVHRR data. *International Journal of Remote Sensing*, 21(6-7), 1303-1330.
- Lüdeke M, Janecek A, Kohlmaier GH (1991) Modelling the seasonal CO₂ uptake by land vegetation using the global vegetation index. *Tellus* 43B: 188-196.
- Ma, J., X. Yan, W. Dong and J. Chou (2015), Gross primary production of global forest ecosystems has been overestimated. *Sci. Rep.* 5, 10820; doi: 10.1038/srep10820.
- Mahmood, R., Pielke, R. A., Hubbard, K. G., Niyogi, D., Dirmeyer, P. A., McAlpine, C., Carleton, A. M., Hale, R., Gameda, S., Beltrán-Przekurat, A., Baker, B., McNider, R., Legates, D. R., Shepherd, M., Du, J., Blanken, P. D., Frauenfeld, O. W., Nair, U.S. and Fall, S. (2014), Land cover changes and their biogeophysical effects on climate. *Int. J. Climatol.*, 34: 929–953. doi:10.1002/joc.3736
- Makarieva, A. M., V. G. Gorshkov, D. Sheil, A. D. Nobre, P. Bunyard, B.-L. Li, 2014: Why Does Air Passage over Forest Yield More Rain? Examining the Coupling between Rainfall, Pressure, and Atmospheric Moisture Content. *J. Hydrometeor.*, 15, 411–426, doi: 10.1175/JHM-D-12-0190.1.
- Maslin, M. (2013), Cascading uncertainty in climate change models and its implications for policy. *The Geographical Journal*, 179: 264–271. doi:10.1111/j.1475-4959.2012.00494.x
- meteorological forcing data set: WATCH Forcing Data methodology applied to ERA-Interim reanalysis data, *Water Resour. Res.*, 50, 7505–7514, doi:10.1002/2014WR015638.
- Muller, J.-P. (2013), GlobAlbedo final validation report Rep., University College London. [Available at http://www.globalbedo.org/docs/GlobAlbedo_FVR_V1_2_web.pdf.]
- Myneni RB, Hall FG, Sellers PJ, Marshak AL (1995) The interpretation of spectral vegetation indexes. *IEEE Transactions on Geoscience and Remote Sensing* 33: 481-486.
- Olson, J. S., Watts, J. A., & Allison, L. J. (1983). Carbon in live vegetation of major world ecosystems (No. DOE/NBB-0037). Oak Ridge National Lab., TN (USA).

	Ref	LC CCI Phase 2: Climate Assessment Report, Year 3		
	Issue	1.0	Date 2017-07-11	
	Page	88		

- Ottlé, C., Lescure, J., Maignan, F., Poulter, B., Wang, T., & Delbart, N. (2013). Use of various remote sensing land cover products for plant functional type mapping over Siberia. *Earth System Science Data*, 5(2), 331-348.
- Peel, M. C., B. L. Finlayson, and T. A. McMahon. "Updated World Map of the Köppen-Geiger Climate Classification." *Hydrology and Earth System Sciences Discussions Hydrol. Earth Syst. Sci. Discuss.* 4.2 (2007): 439-73.
- Peel, M. C., Finlayson, B. L., and McMahon, T. A. (2007), Updated world map of the Köppen-Geiger climate classification, *Hydrol. Earth Syst. Sci.*, 11, 1633-1644, doi:10.5194/hess-11-1633-2007.
- Peng S, Ciais P, Chevallier F, Peylin P, Cadule P, Sitch S, Piao S, Ahlström A, Huntingford C, Levy P (2015) Benchmarking the seasonal cycle of CO₂ fluxes simulated by terrestrial ecosystem models *Global Biogeochemical Cycles* 29: 46-64 10.1002/2014GB004931.
- Poulter B, MacBean N, Hartley A, et al (2015) Plant functional type classification for earth system models: results from the European Space Agency's Land Cover Climate Change Initiative. *Geosci Model Dev* 8:2315–2328. doi: 10.5194/gmd-8-2315-2015
- Poulter, B., P. Ciais, E. Hodson, H. Lischke, F. Maignan, S. Plummer, and N. E. Zimmermann. "Plant Functional Type Mapping for Earth System Models." *Geoscientific Model Development Geosci. Model Dev.* 4.4 (2011): 993-1010.
- Quaife, T., S. Quegan, M. Disney, P. Lewis, M. Lomas, and F. I. Woodward. "Impact of Land Cover Uncertainties on Estimates of Biospheric Carbon Fluxes." *Global Biogeochem. Cycles Global Biogeochemical Cycles* 22.4 (2008).
- Quaife, Tristan, and Edward Cripps. "Bayesian Analysis of Uncertainty in the GlobCover 2009 Land Cover Product at Climate Model Grid Scale." *Remote Sensing* 8.4 (2016): 314.
- Raddatz, T. J., Reick, C., Knorr, W., Kattge, J., Roeckner, E., Schnur, R., Schnitzler, K.-G., Wetzell, P., and Jungclaus, J. H.: Will the tropical land biosphere dominate the climate-carbon cycle feedback during the twenty-first century?, *Climate Dyn.*, doi: 10.1007/s00382-007-0247-8, 2007.
- Ramankutty, N., and J. A. Foley (1999), Estimating historical changes in global land cover: Croplands from 1700 to 1992, *Global Biogeochem. Cycles*, 13(4), 997–1027, doi:10.1029/1999GB900046.
- Reick, Christian H., Veronika Gayler, Thomas Raddatz, Reiner Schnur and Stiig Wilkenskjeld: JSBACH – the land component of ECHAM6, 2015
- Roeckner, E., G. Bäuml, L. Bonaventura, R. Brokopf, M. Esch, M. Giorgetta, S. Hagemann, I. Kirchner, L. Kornblueh, E. Manzini, A. Rhodin, U. Schlese, U. Schulzweida, A. Tompkins (2003): The atmospheric general circulation model ECHAM 5. PART I: Model description. MPI-Report No. 349
- Sellers, P.J.; Dickinson, R.E.; Randall, D.A.; Betts, A.K.; Hall, F.G.; Berry, J.A.; Collatz, G.J.; Denning, A.S.; Mooney, H.A.; Nobre, C.A.; N. Sato; C. B. Field; A. Henderson-Sellers Modeling the exchanges of energy, water, and carbon between continents and the atmosphere. *Science* 1997, 275, 502–509.
- Sheil, D. and D. Murdiyarto; How Forests Attract Rain: An Examination of a New Hypothesis. *BioScience* 2009; 59 (4): 341-347. doi: 10.1525/bio.2009.59.4.12
- Sitch S, Friedlingstein P, Gruber N, et al (2015) Recent trends and drivers of regional sources and sinks of carbon dioxide. *Biogeosciences* 12:653–679. doi: 10.5194/bg-12-653-2015
- Spracklen, D. V., S. R. Arnold, and C. M. Taylor (2012), Observations of increased tropical rainfall preceded by air passage over forests, *Nature* 489, 282–285, doi:10.1038/nature11390

	Ref	LC CCI Phase 2: Climate Assessment Report, Year 3		
	Issue	1.0	Date 2017-07-11	
	Page	89		

- Steltzer H, Welker JM (2006) Modeling the effect of photosynthetic vegetation properties on the NDVI-LAI relationship. *Ecology* 87(11): 2765–2772.
- Sterling, S. M., A. Ducharne, and J. Polcher (2013), The impact of global land-cover change on the terrestrial water cycle, *Nature Climate Change* 3, 385–390 doi:10.1038/nclimate1690
- Stevens B. and Bony S. 2013, What are climate models missing? *Science* 340, 1053. (doi:10.1126/science.1237554)
- Stevens, B., Giorgetta, M., Esch, M., Mauritsen, T., Crueger, T., Rast, S., Salzmann, M., Schmidt, H., Bader, J., Block, K., Brokopf, R., Fast, I., Kinne, S., Kornblueh, L., Lohmann, U., Pincus, R., Reichler, T., and Roeckner, E.: The atmospheric component of the MPI-M Earth System Model: ECHAM6, *J. Adv. Model Earth Syst.*, 5, 146-172. doi:10.1002/jame.20015, 2013.
- Still, C. J., J. A. Berry, G. J. Collatz, and R. S. DeFries, Global distribution of C3 and C4 vegetation: Carbon cycle implications, *Global Biogeochem. Cycles*, 17(1), 1006, doi:10.1029/2001GB001807, 2003.
- Still, C.J., J.A. Berry, G.J. Collatz, and R.S. Defries (2009), ISLSCP II C4 Vegetation Percentage. ORNL DAAC, Oak Ridge, Tennessee, USA. <http://dx.doi.org/10.3334/ORNLDAAAC/932>.
- Stocker, Thomas. *Climate Change 2013: The Physical Science Basis: Working Group I Contribution to the Fifth Assessment Report of the Intergovernmental Panel on Climate Change*.
- Stöckli R and Vidale PL (2004) European plant phenology and climate as seen in a 20-year AVHRR land-surface parameter dataset. *International Journal of Remote Sensing*, 25(17): 3303-3330
- Tansey K et al., (2005) A global inventory of burned areas at 1km resolution for the year 2000 derived from SPOT VEGETATION data. *Climatic Change* 67(2): 345-377.
- Taylor, K. E., Stouffer, R. J., and Meehl, G. A.: An overview of CMIP5 and the experiment design, *Bull. Amer. Meteor. Soc.*, 93 (4), 485-498, 2012.
- Taylor, K. E., Williamson, D., and Zwiers, F.: The sea surface temperature and sea-ice concentration boundary conditions for AMIP II simulations, PCMDI Report, 60, Program for Climate Model Diagnosis and Intercomparison. Lawrence Livermore National Laboratory, Livermore, California, 25 pp., 2000.
- Tillack A, Clasen A, Kleinschmit B, Forster M (2014) Estimation of the seasonal leaf area index in an alluvial forest using high-resolution satellite-based vegetation indices. *Remote Sensing of Environment* 141: 52-63.
- Trenberth, K. E., L. Smith, T. Qian, A. Dai, and J. Fasullo, 2007: Estimates of the global water budget and its annual cycle using observational and model data. *J. Hydrometeor.*, 8, 758–769, doi:10.1175/JHM600.1.
- Tucker CJ (1979) Red and photographic infrared linear combinations for monitoring vegetation. *Remote Sensing of Environment* 8: 127-150.
- Turner DP, Cohen WB, Kennedy RE, Fassnacht KS, Briggs JM (1999) Relationships between leaf area index and Landsat TM spectral vegetation indices across three temperate zone sites. *Remote Sensing of Environment* 70(1): 52-68.
- Ustin, Susan L., and John A. Gamon. "Remote Sensing of Plant Functional Types." *New Phytologist* 186.4 (2010): 795-816.
- van der Werf et al. (2010): G. R. van der Werf, J. T. Randerson, L. Giglio, G. J. Collatz, M. Mu, P. S. Kasibhatla, D. C. Morton, R. S. DeFries, Y. Jin, and T. T. van Leeuwen, "Global fire emissions and the contribution of deforestation, savanna, forest, agricultural, and peat fires (1997–2009)", *Atmos. Chem. Phys.*, 10, 11707–11735, 2010, doi:10.5194/acp-10-11707-2010

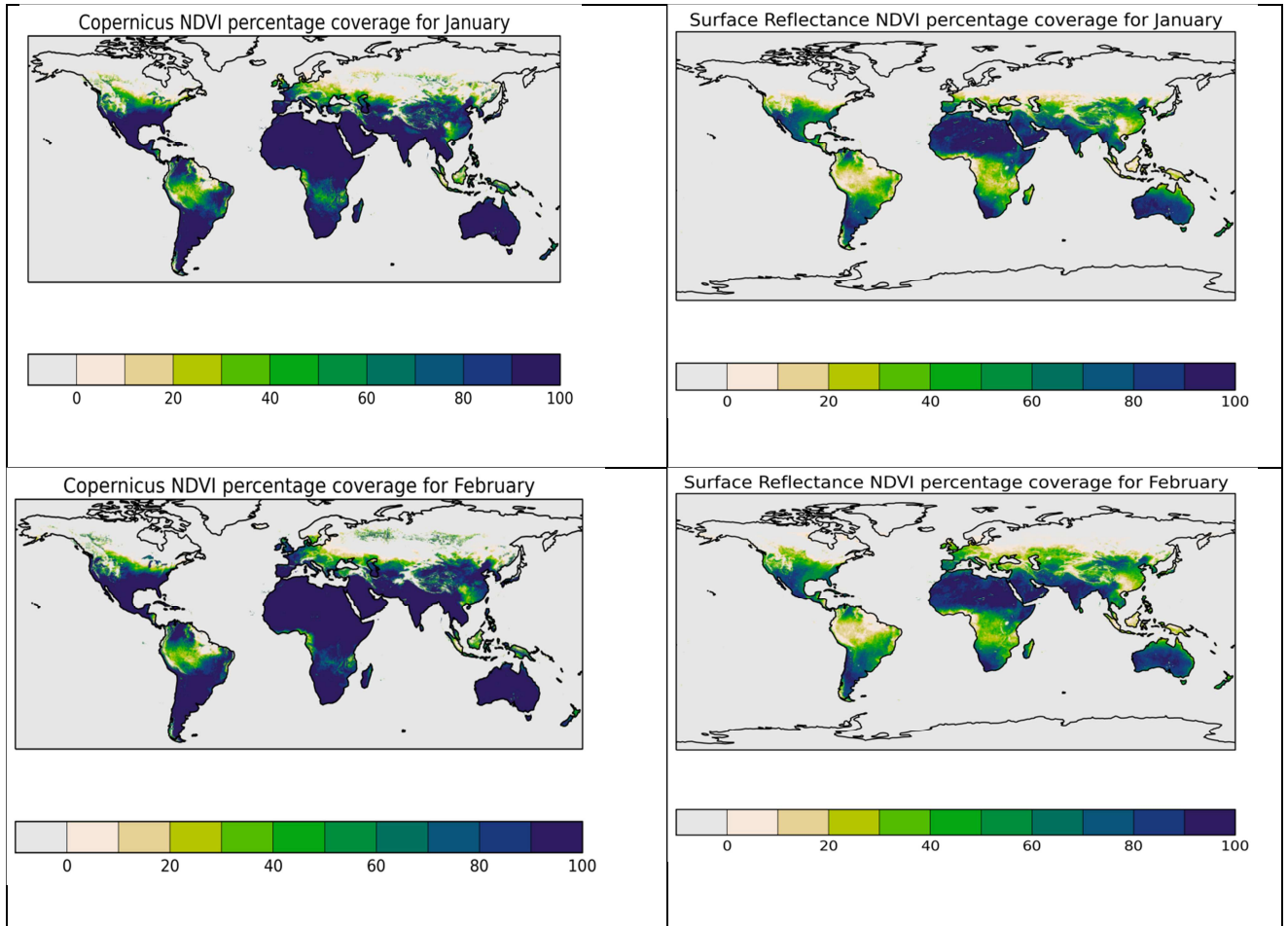
	Ref	LC CCI Phase 2: Climate Assessment Report, Year 3		
	Issue	1.0	Date 2017-07-11	
	Page	90		

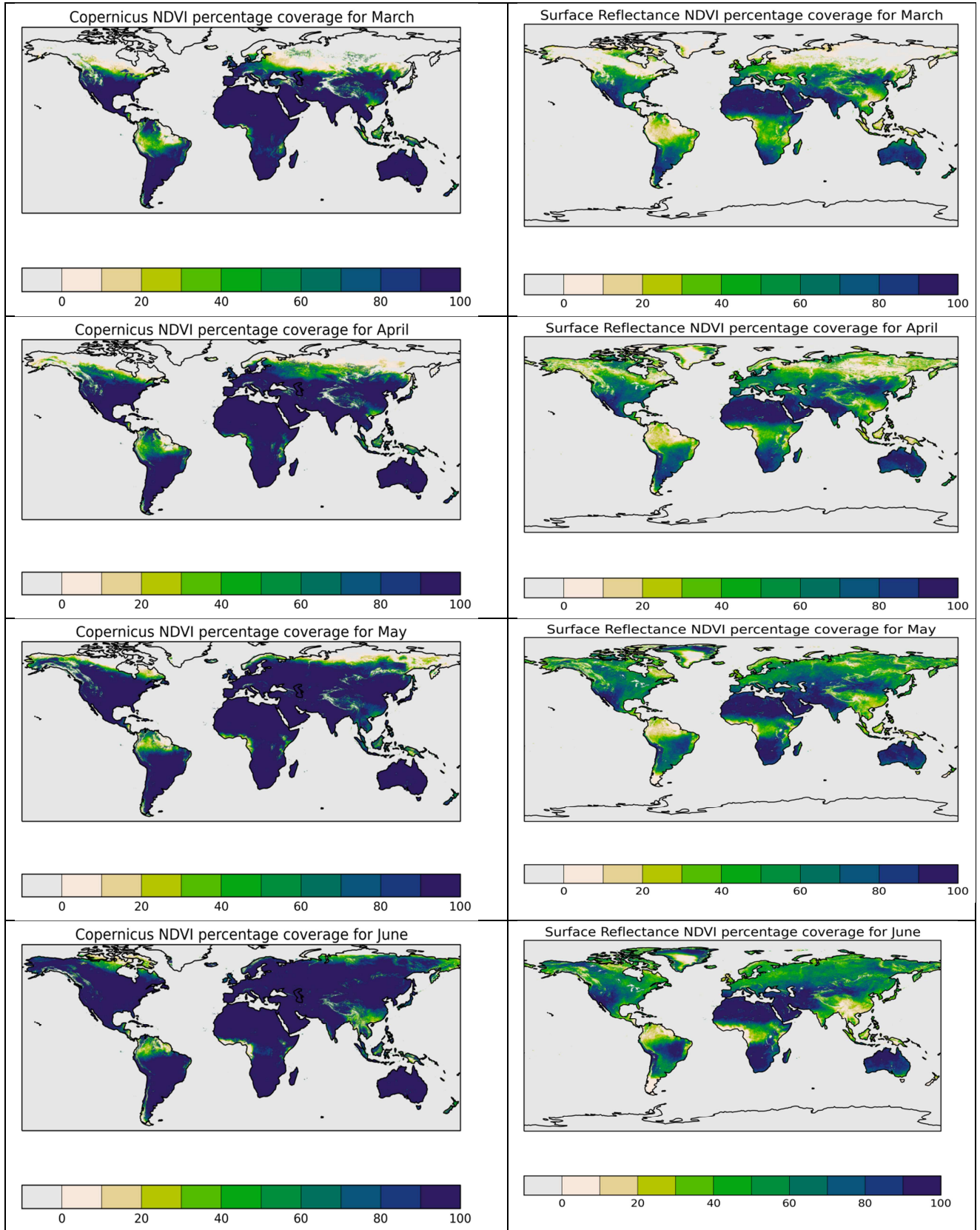
- Wang Q, Adiku A, Tenhunen J, Granier A (2005) On the relationship of NDVI with leaf area index in a deciduous forest site. *Remote Sensing of Environment* 94: 244-255.
- Wang, K., and R. E. Dickinson (2012), A review of global terrestrial evapotranspiration: Observation, modeling, climatology, and climatic variability, *Rev. Geophys.*, 50, RG2005, doi:10.1029/2011RG000373.
- Weedon, Graham P., et al. "The WFDEI meteorological forcing data set: WATCH Forcing Data methodology applied to ERA-Interim reanalysis data." *Water Resources Research* 50.9 (2014): 7505-7514.
- Wilkenskjeld et al. (2017): Stiig Wilkenskjeld, Silvia Kloster, and Goran Georgievski, "Assessing Carbon Emissions from Wildfires using observed data from ESA-CCI-Fire and the JSBACH vegetation model."
- Yoshimura, K. and Kanamitsu, M.: Dynamical Global Downscaling of Global Reanalysis, *Mon. Weather Rev.*, 136(8), 2983–2998, 2008.
- Zängl, G., Reinert, D., Rípodas, P. and Baldauf, M. (2015), The ICON (ICOsahedral Non-hydrostatic) modelling framework of DWD and MPI-M: Description of the non-hydrostatic dynamical core. *Q.J.R. Meteorol. Soc.*, 141: 563–579. doi:10.1002/qj.2378
- Zhang, X., Friedl, M. A., Schaaf, C. B., Strahler, A. H., Hodges, J. C., Gao, F., ... & Huete, A. (2003). Monitoring vegetation phenology using MODIS. *Remote sensing of environment*, 84(3), 471-475.
- Zhang, Y. et al. Multi-decadal trends in global terrestrial evapotranspiration and its components. *Sci. Rep.* 6, 19124; doi: 10.1038/srep19124 (2016).
- Zhao, K. and Jackson, R. B. (2014), Biophysical forcings of land-use changes from potential forestry activities in North America. *Ecological Monographs*, 84: 329–353. doi:10.1890/12-1705.1
- Zhu, Z.; Bi, J.; Pan, Y.; Ganguly, S.; Anav, A.; Xu, L.; Samanta, A.; Piao, S.; Nemani, R.R.; Myneni, R.B. Global data sets of vegetation leaf area index (LAI) 3g and Fraction of Photosynthetically Active Radiation (FPAR) 3g derived from Global Inventory Modeling and Mapping Studies (GIMMS) Normalized Difference Vegetation Index (NDVI3g) for the period 1981 to 2011. *Remote Sens* 2013, 5, 927–948.

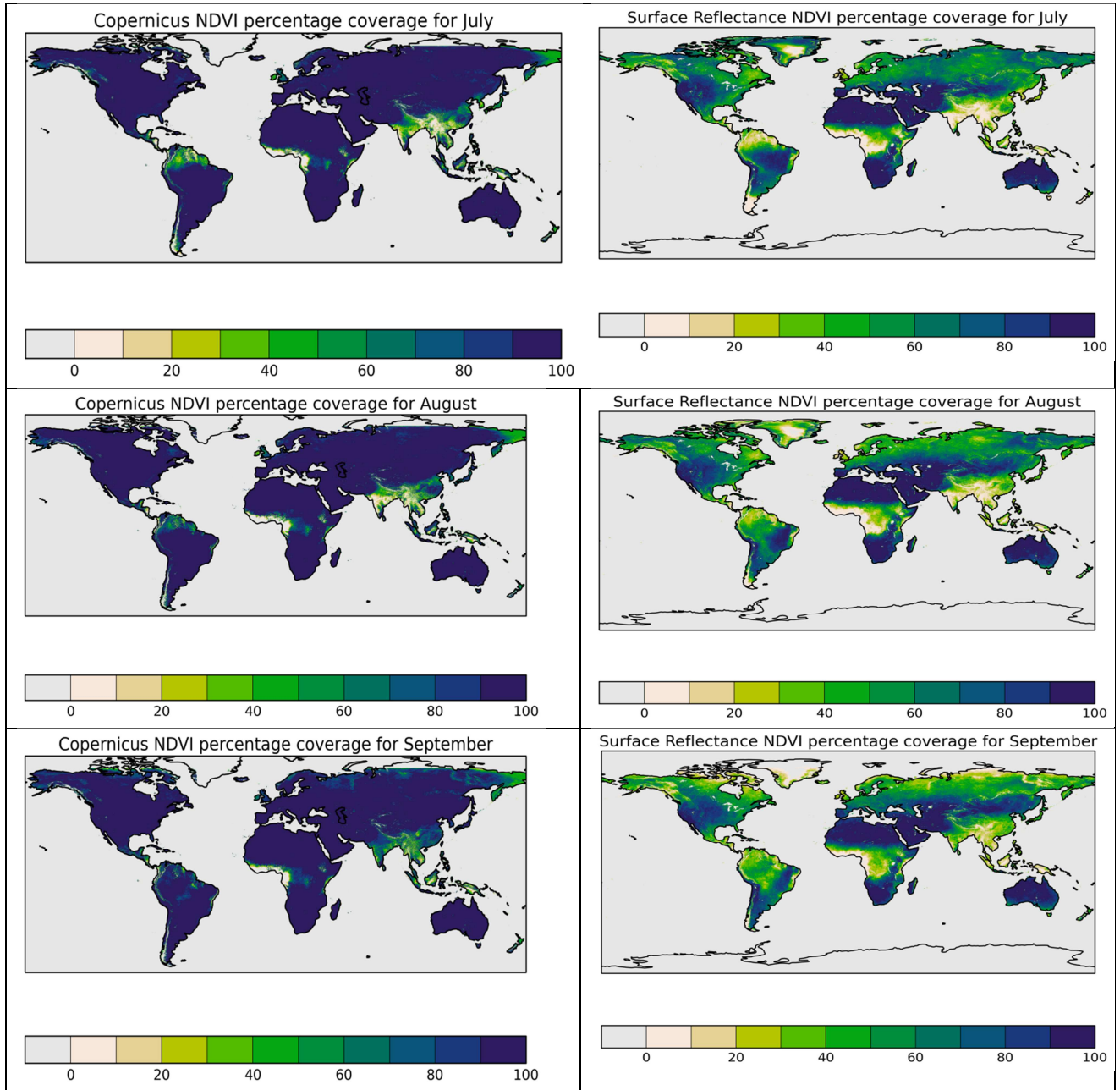
7. APPENDIX

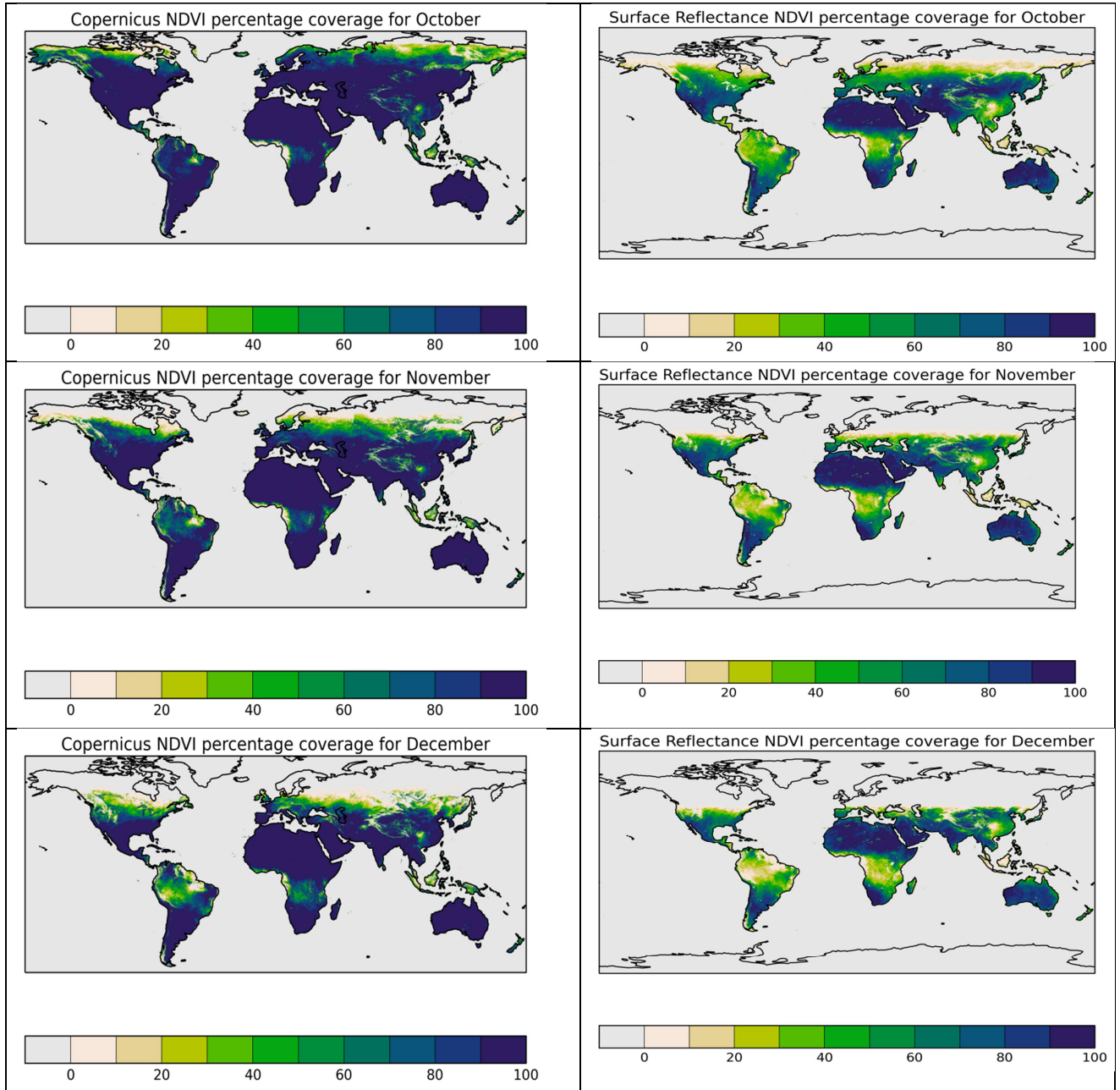
7.1. Appendices for MOHC model results

7.1.2. Appendix MOHC – 1









7.1.3. Appendix MOHC - 2

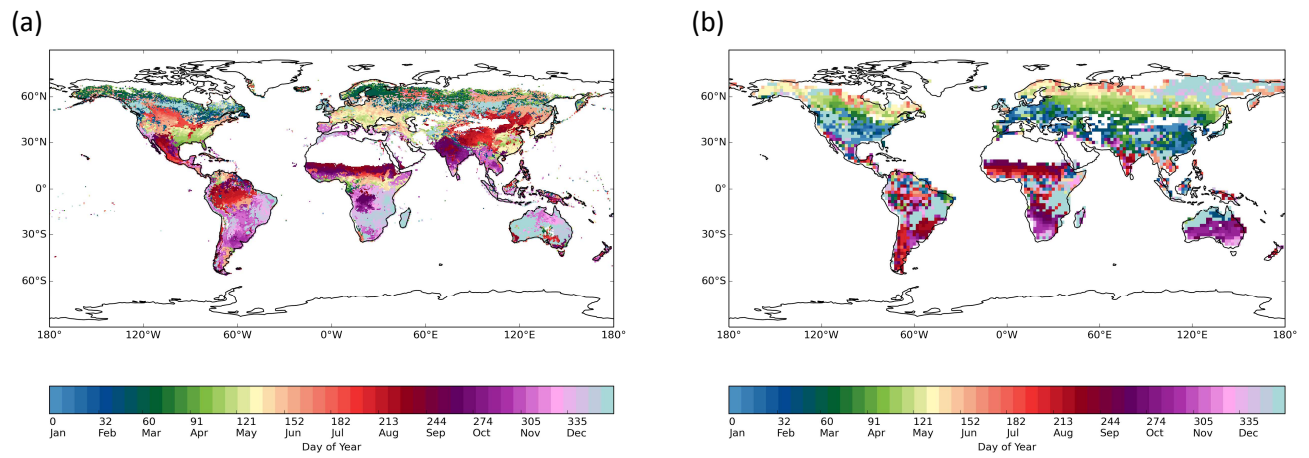


Figure A1. Comparison of (a) Condition-NDVI and (b) JULES-NDVI for maturity (Ma).

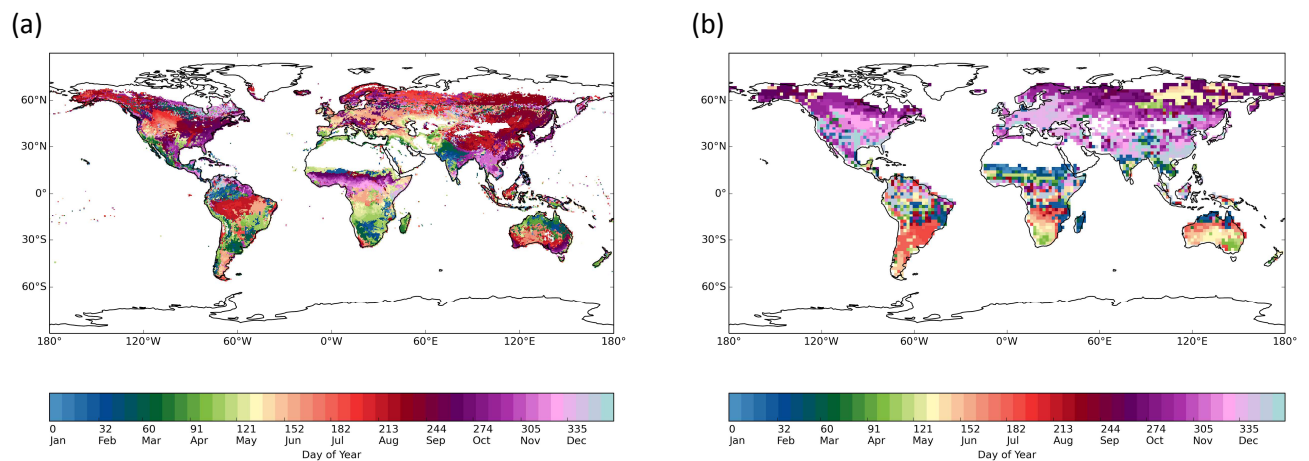


Figure A2. Comparison of (a) Condition-NDVI and (b) JULES-NDVI for senescence (Se).

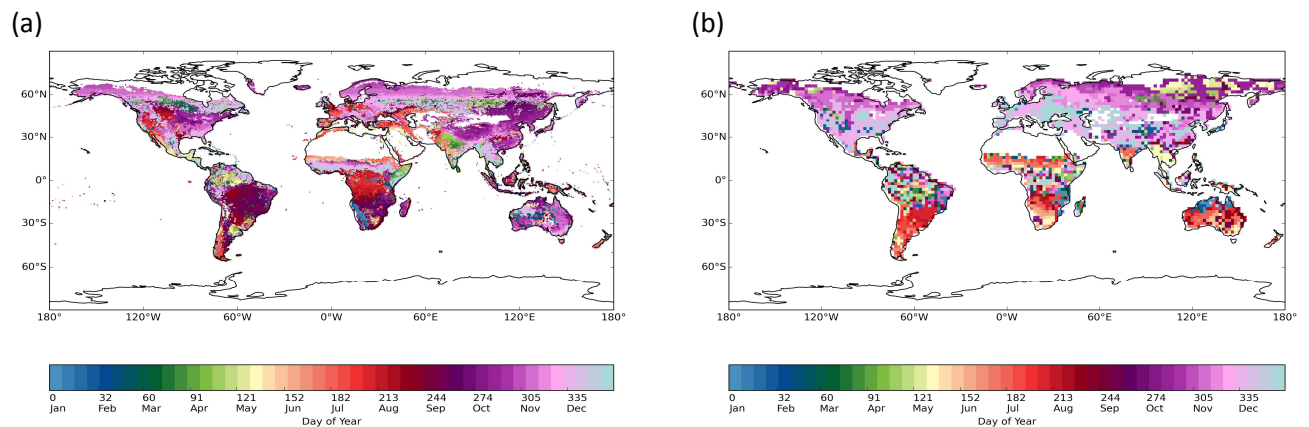


Figure A3. Comparison of (a) Condition-NDVI and (b) JULES-NDVI for end of season (EOS).

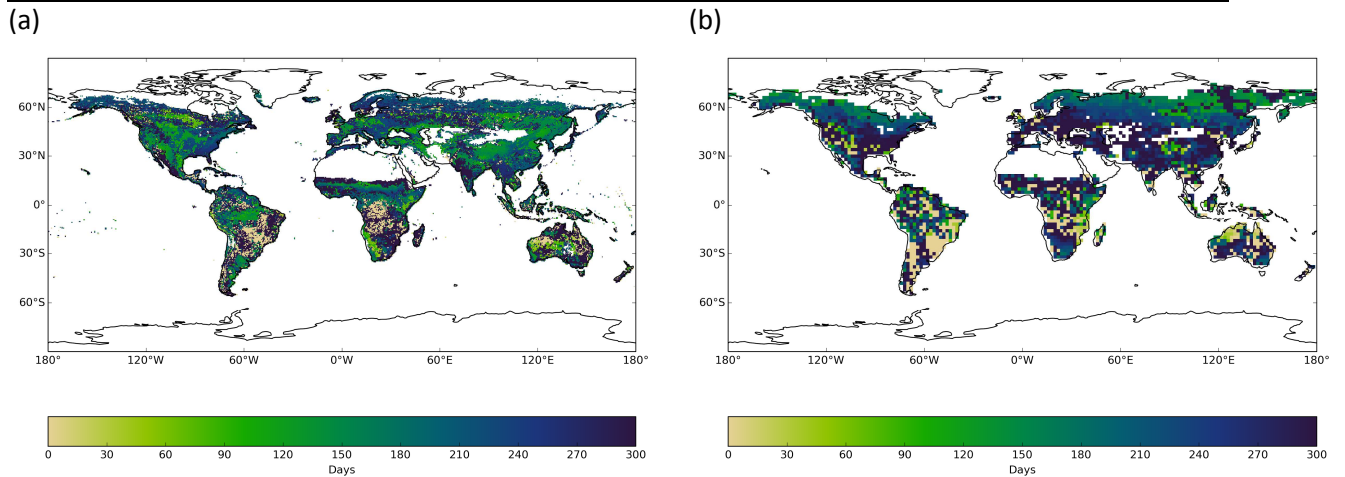


Figure A4. Comparison of (a) Condition-NDVI and (b) JULES-NDVI for length of season (LOS).

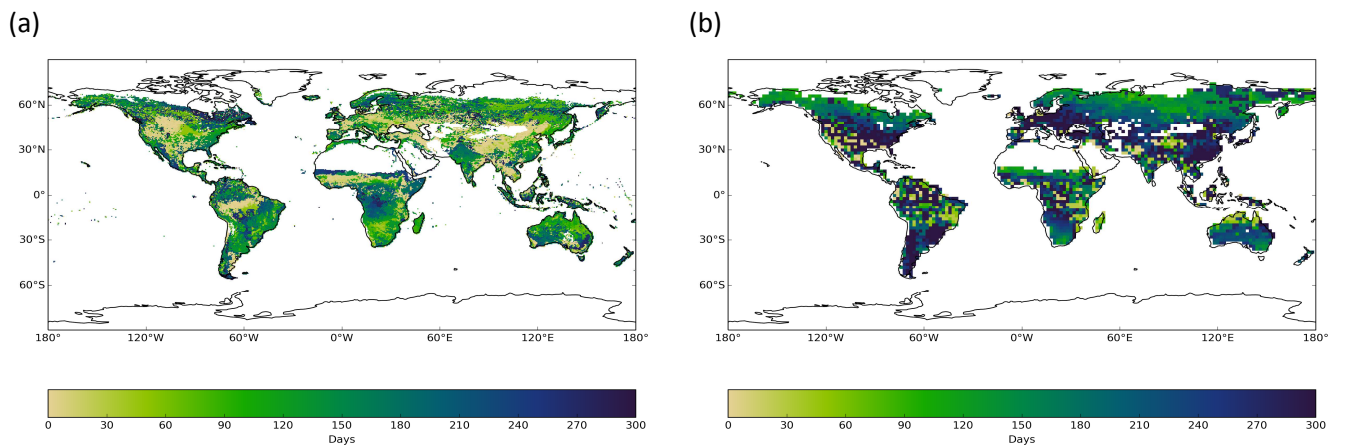


Figure A5. Comparison of (a) Condition-NDVI and (b) JULES-NDVI for length of greenness (LOG).

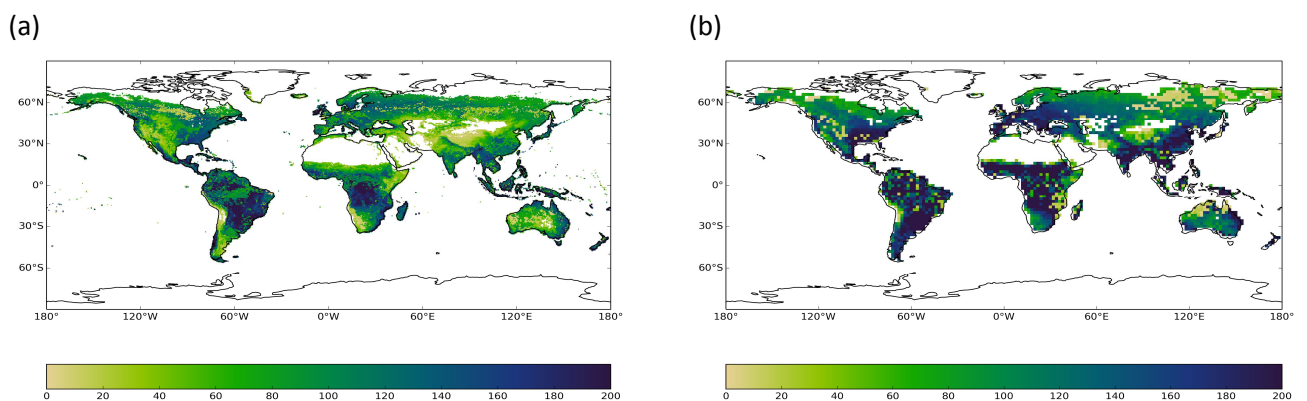
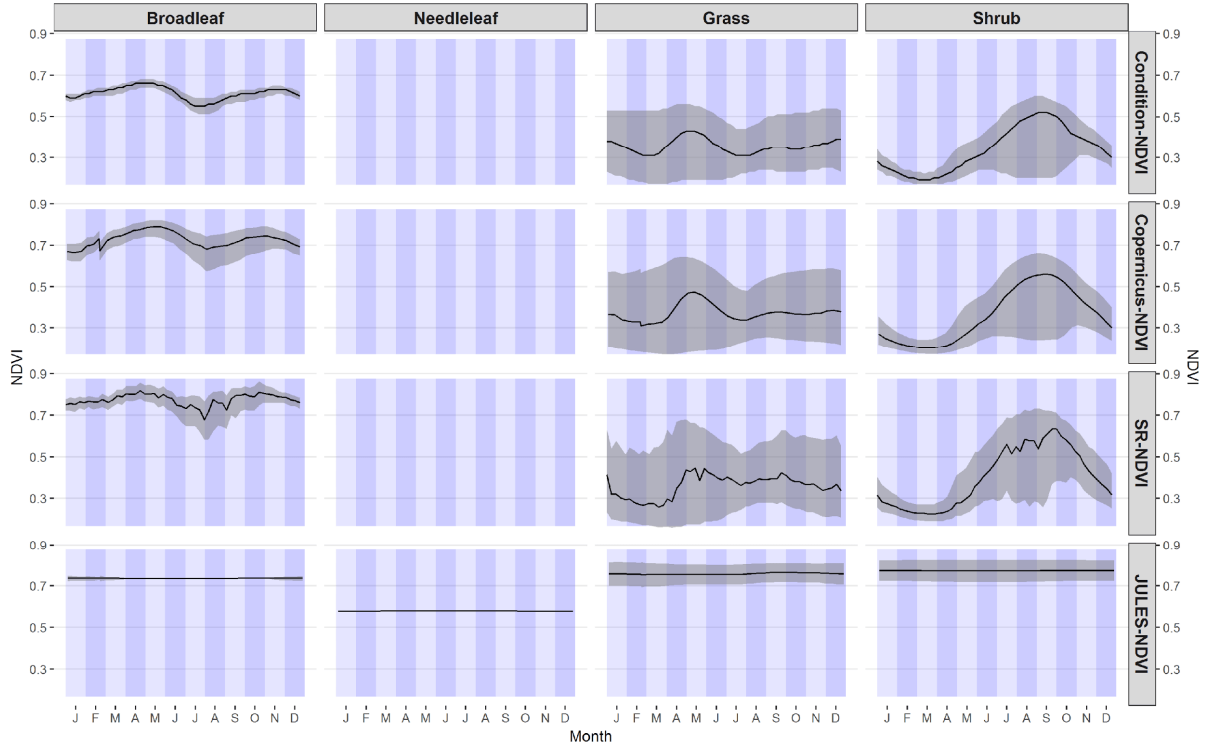


Figure A6. Comparison of (a) Condition-NDVI and (b) JULES-NDVI for season integral (SI).

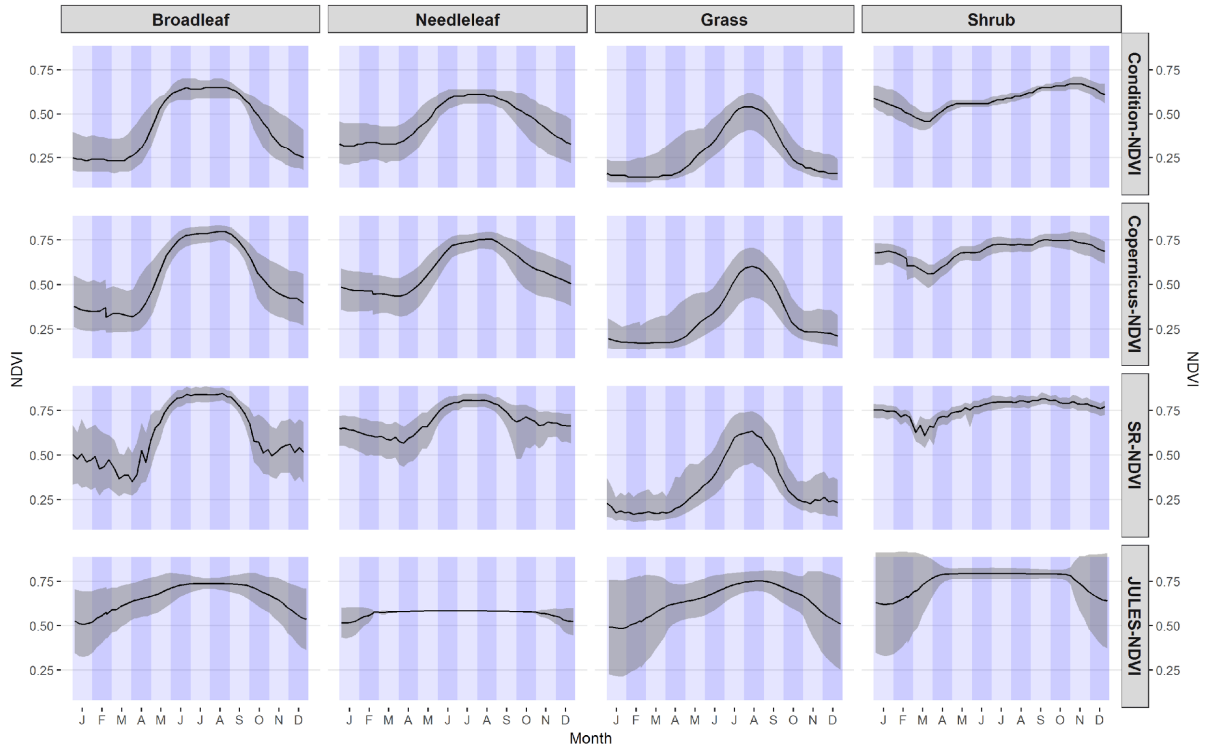
7.1.4. Appendix MOHC - 3

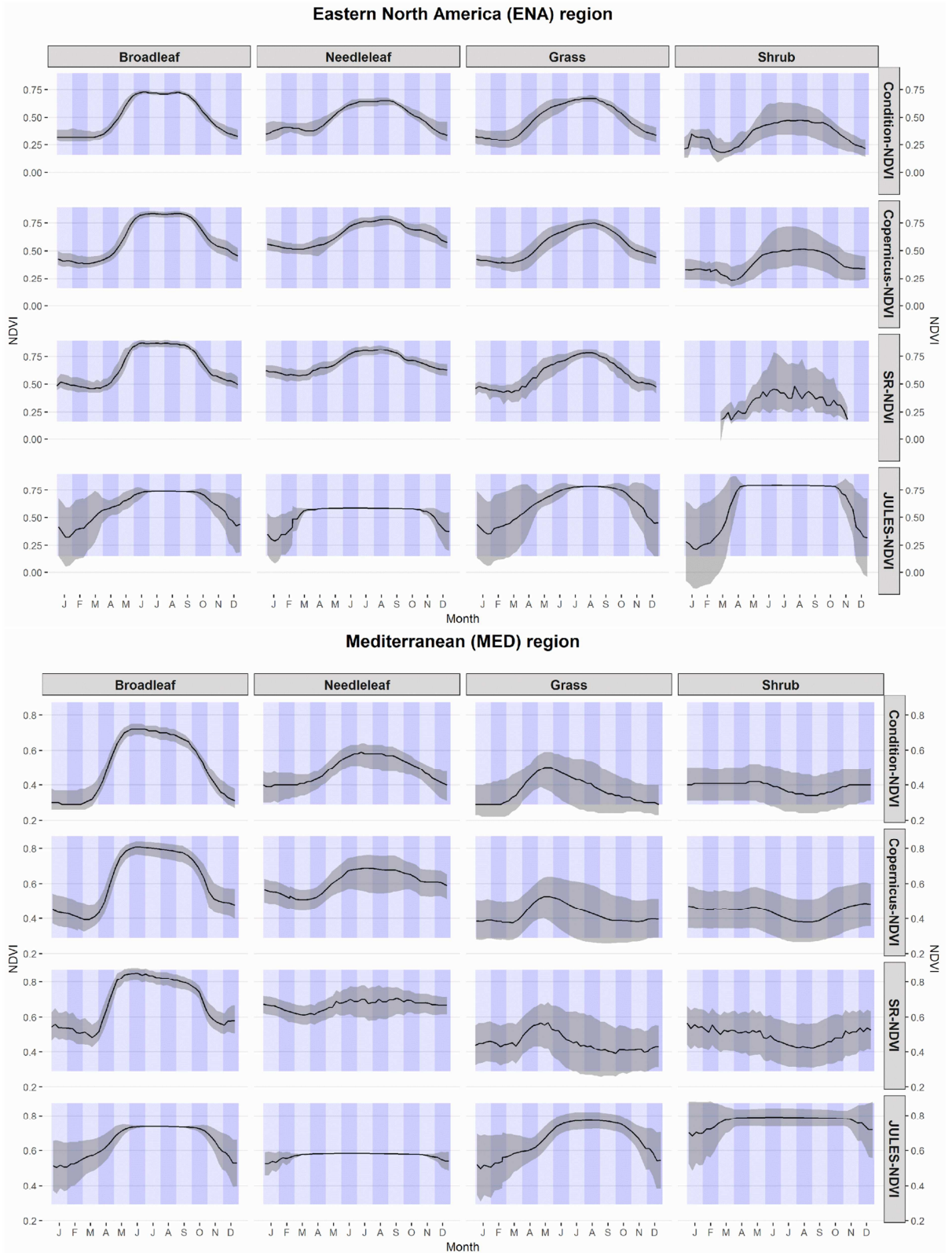
East Africa (EAF) region

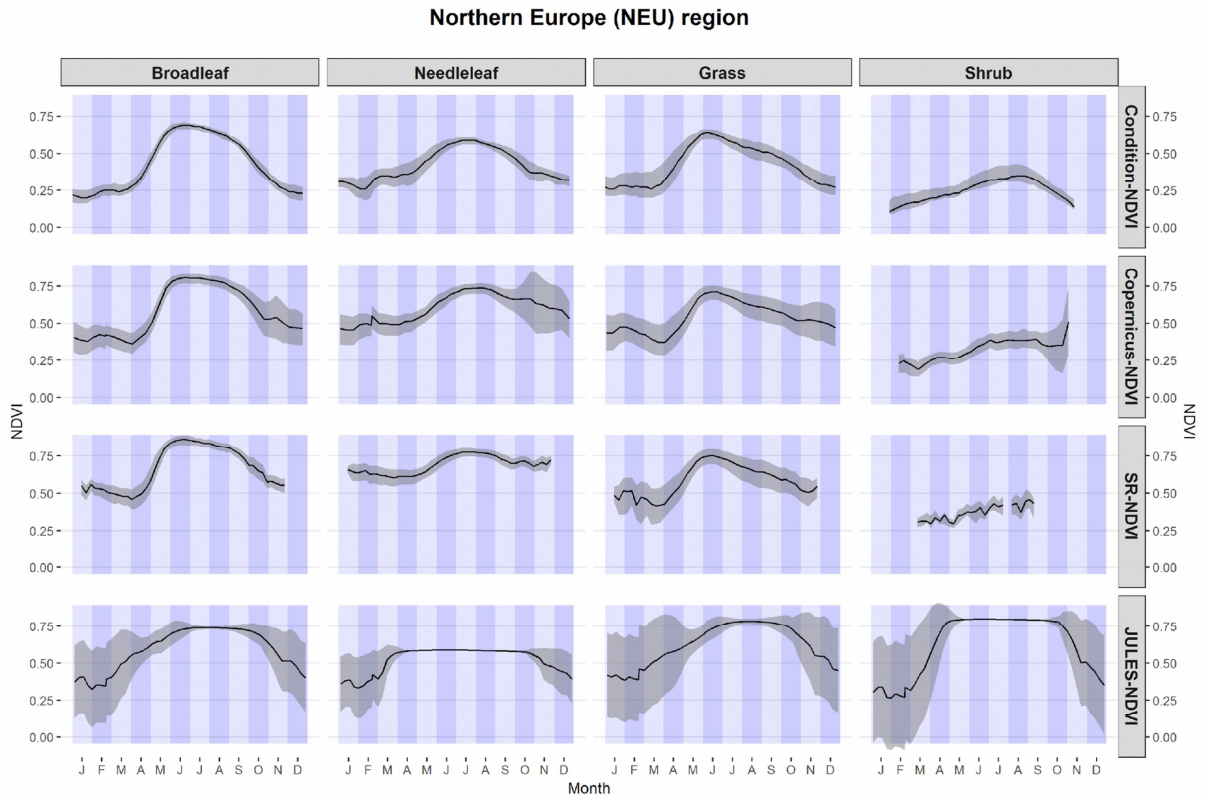
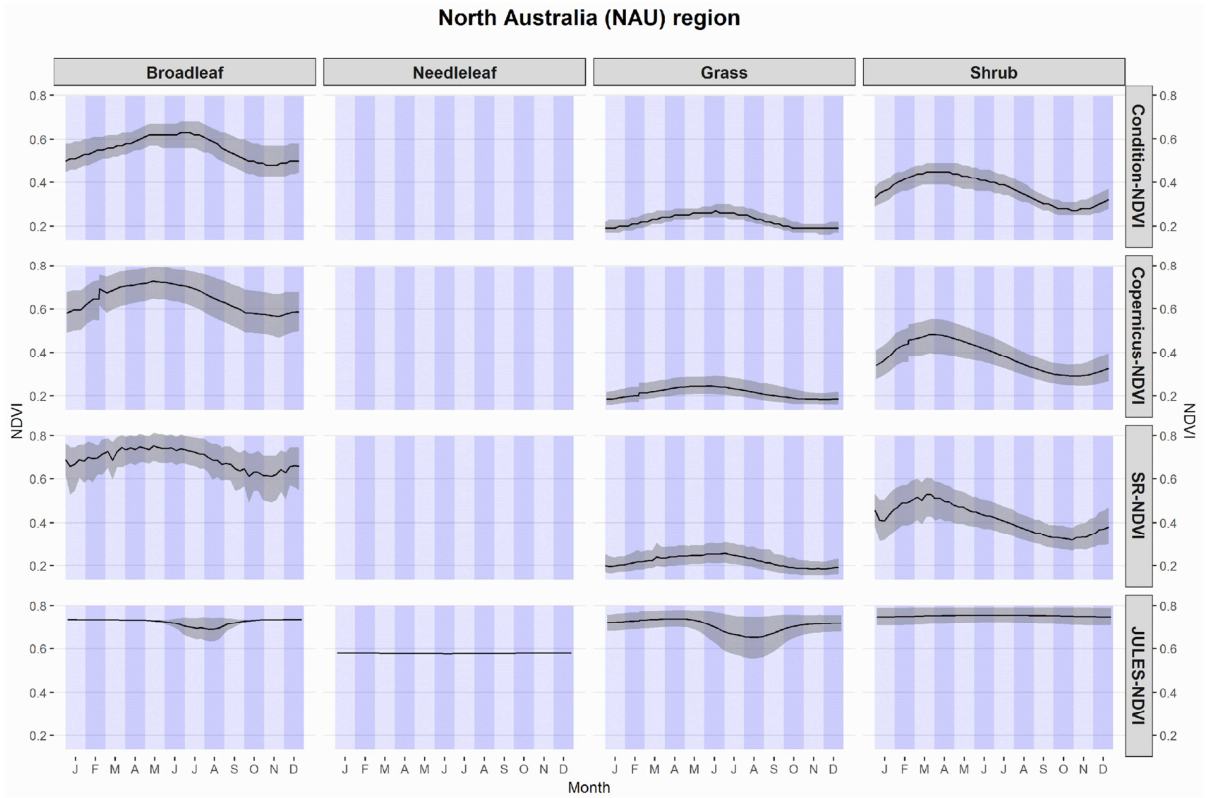


8.

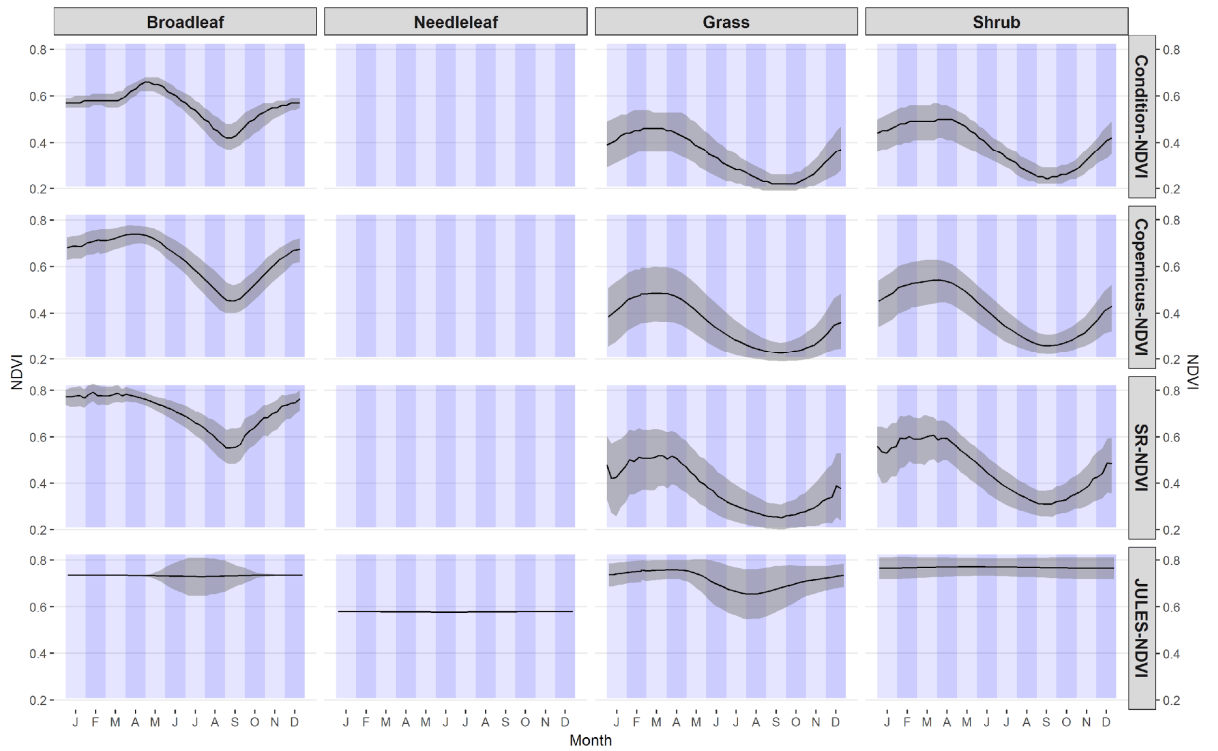
East Asian (EAS) region



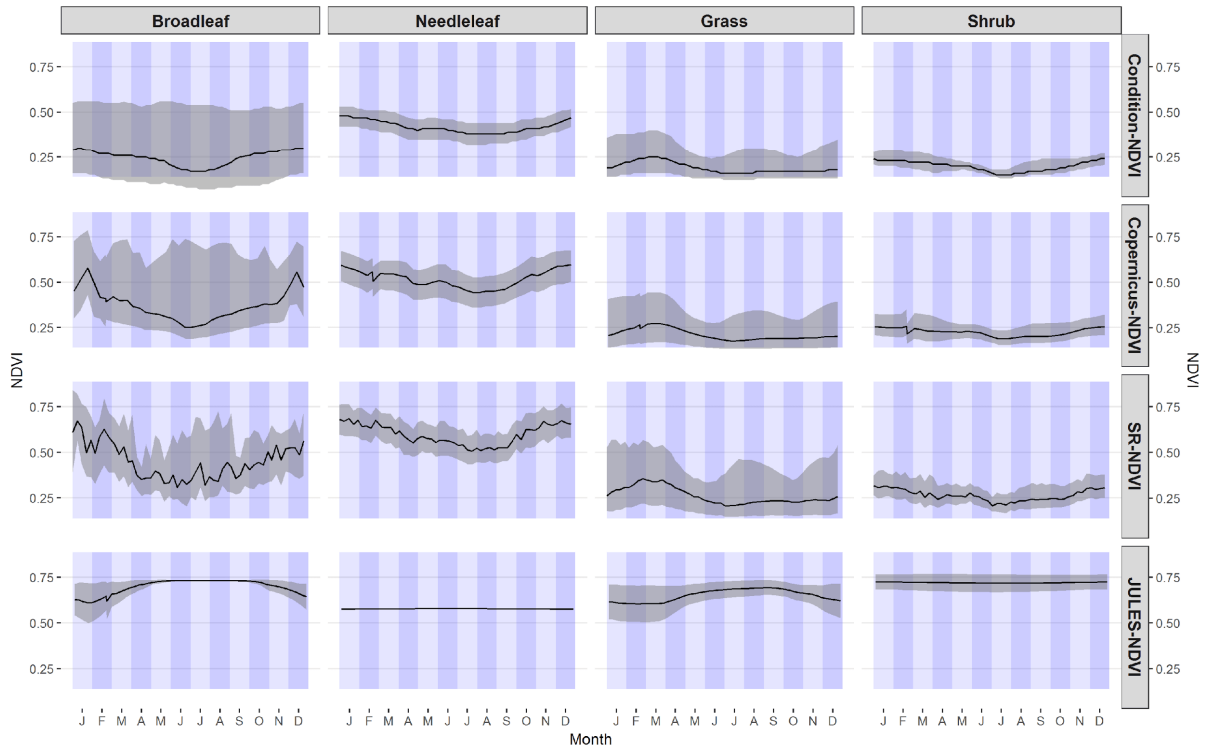




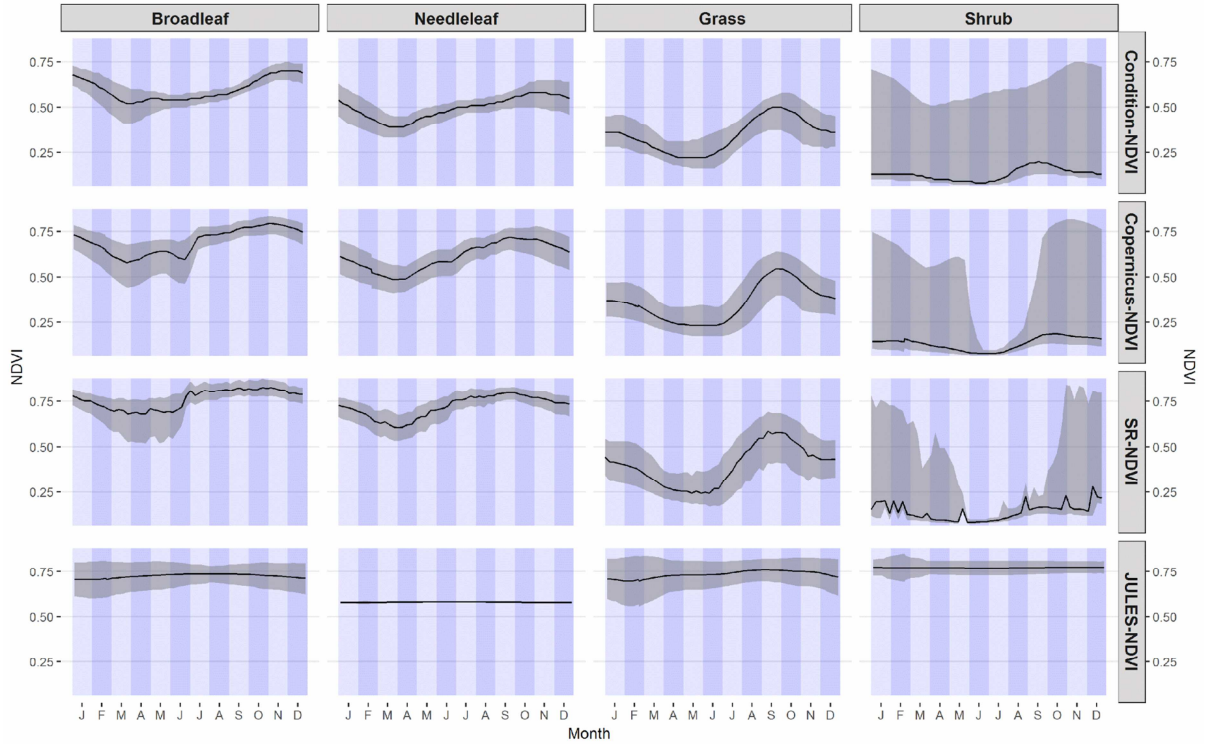
Southern African (SAF) region



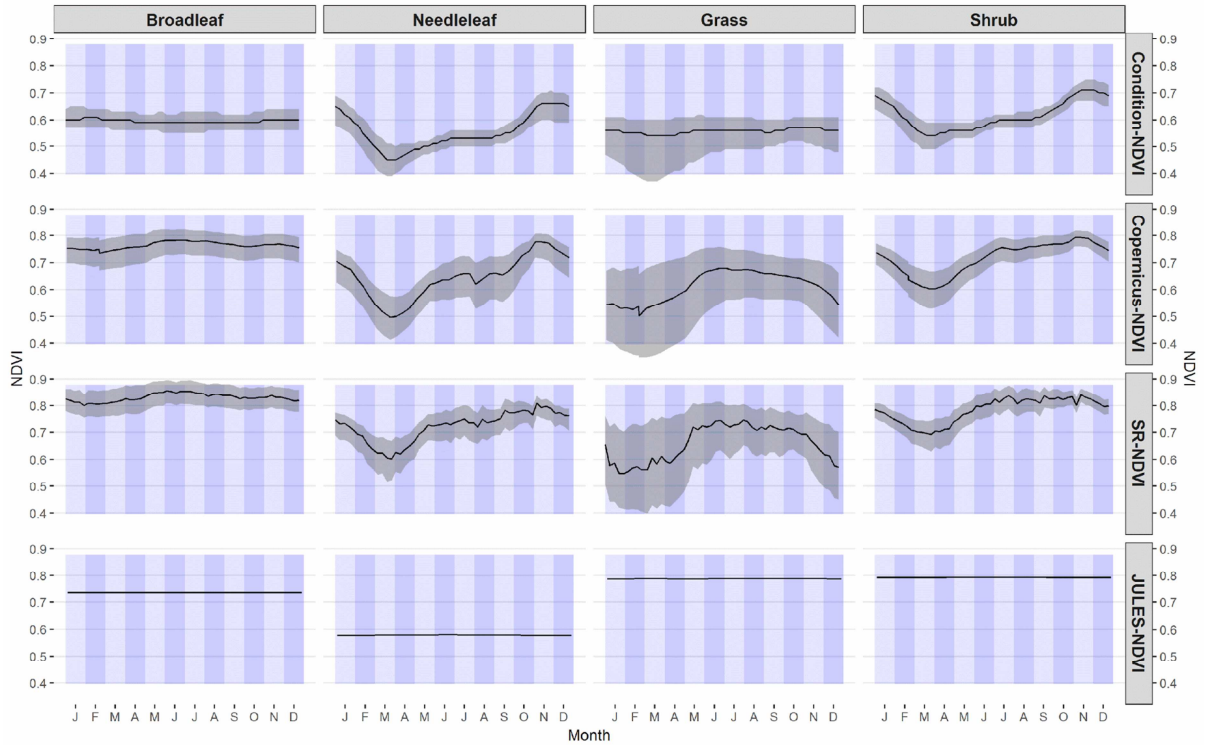
Sahara (SAH) region



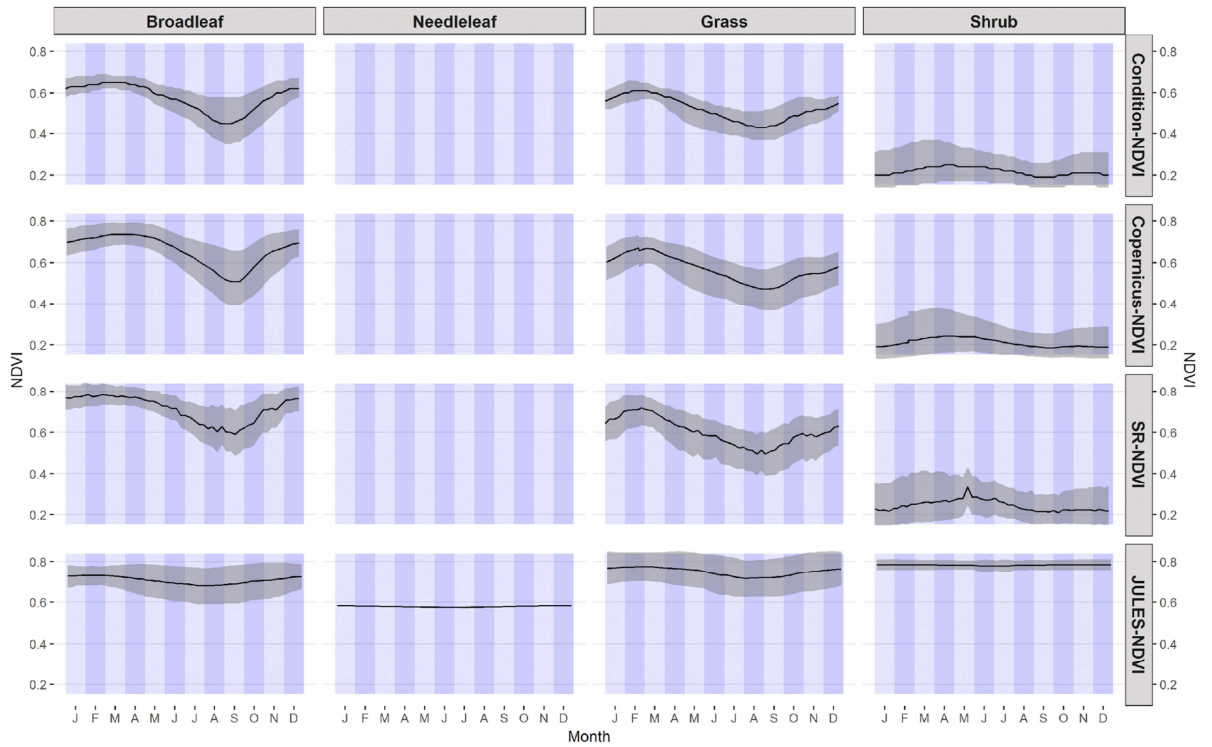
Southern Asia (SAS) region



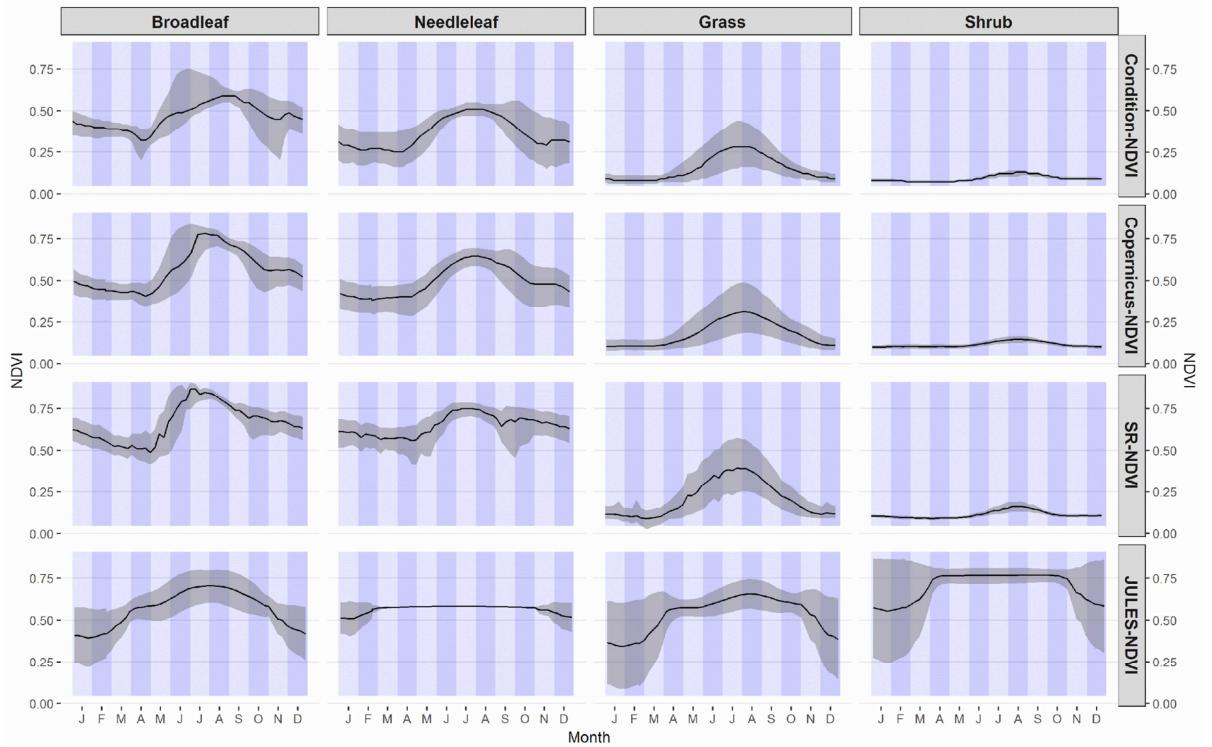
South East Asia (SEA) region



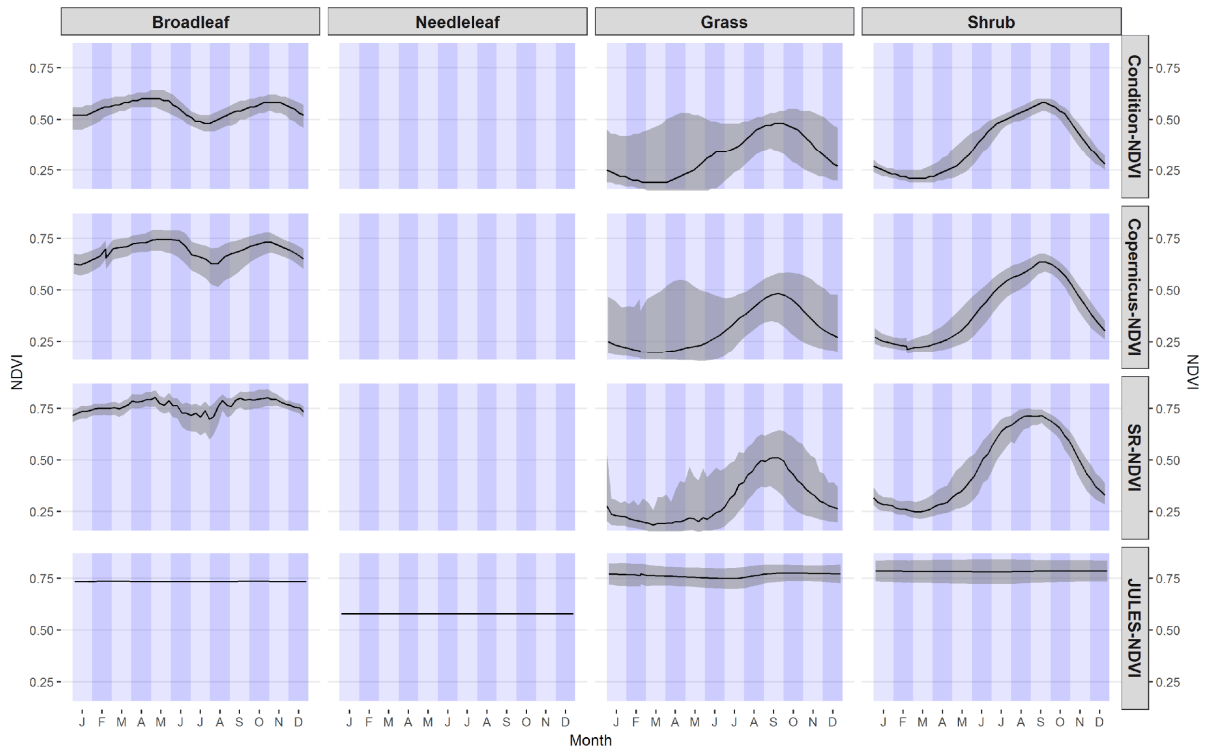
Southern South America (SSA) region



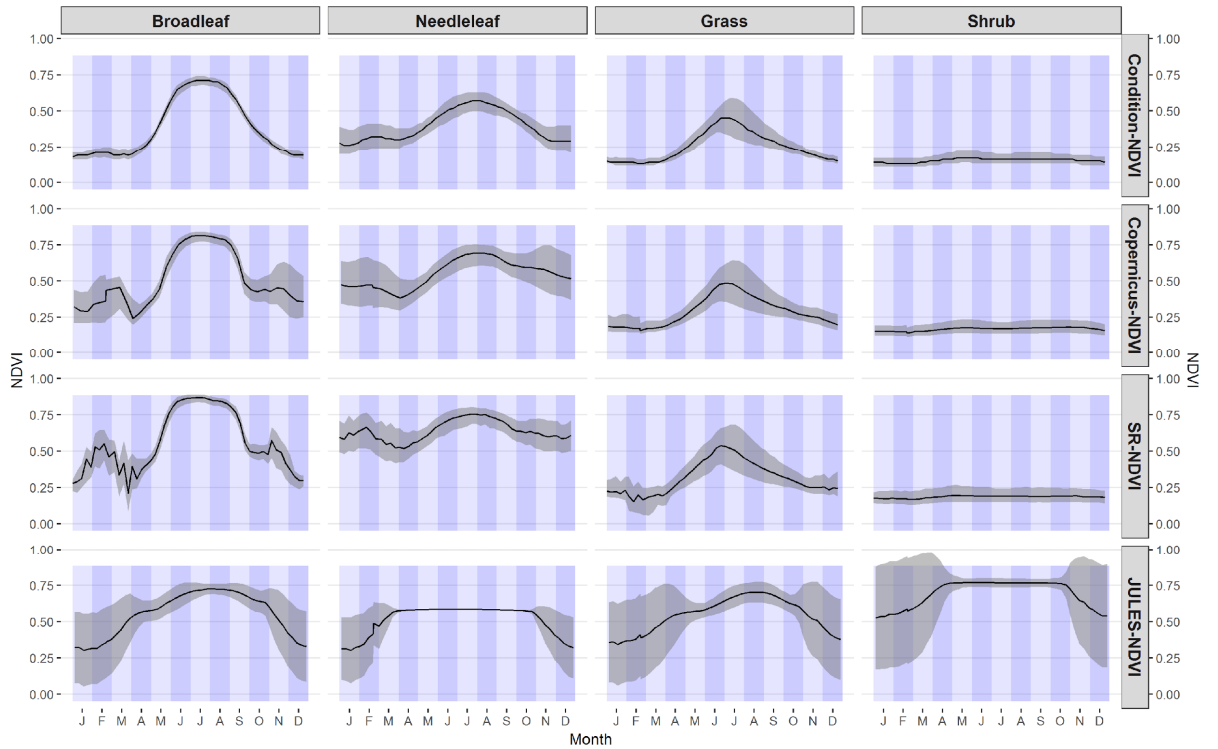
Tibet (TIB) region

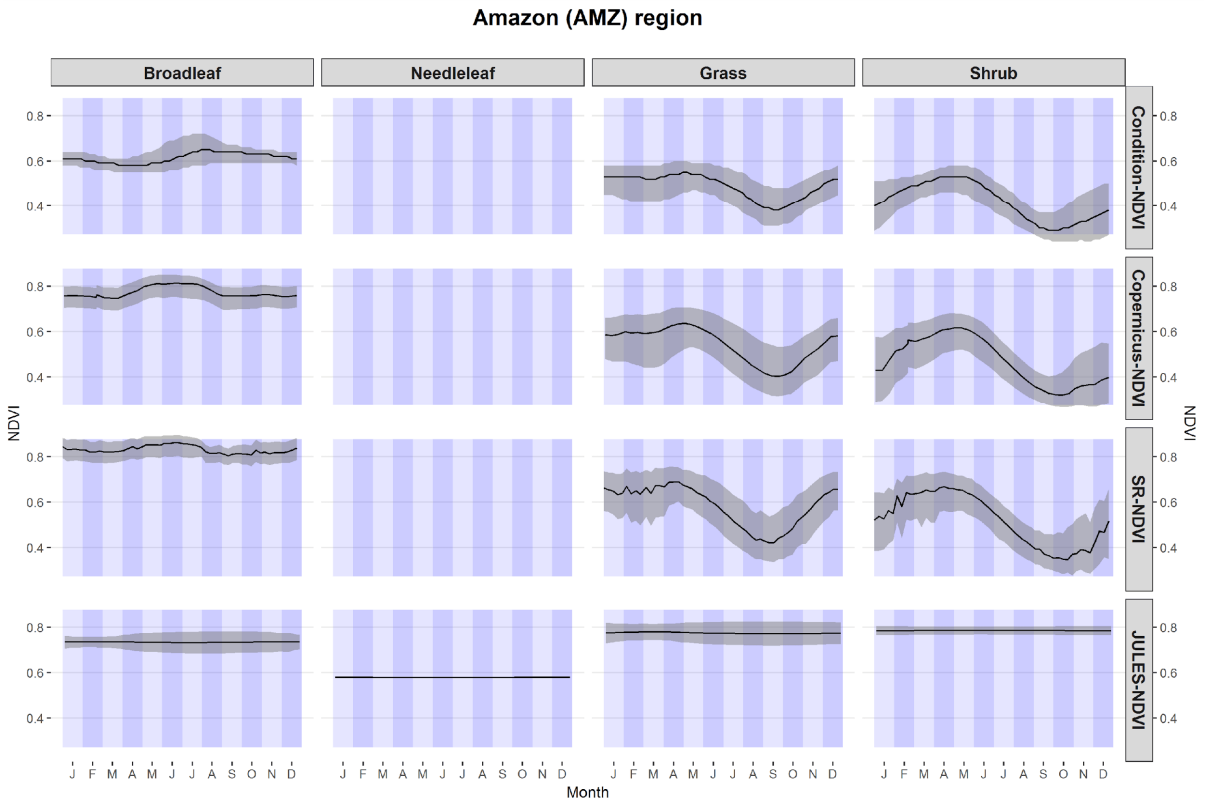
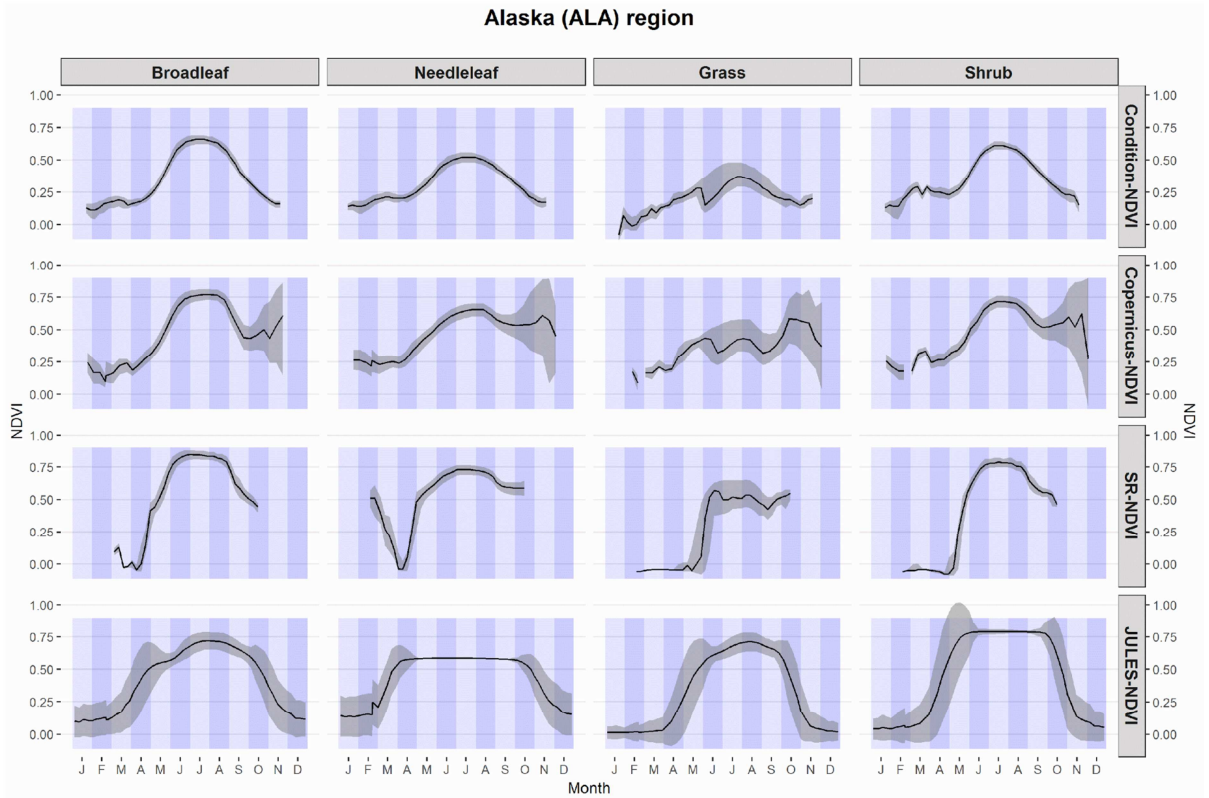


West Africa (WAF) region

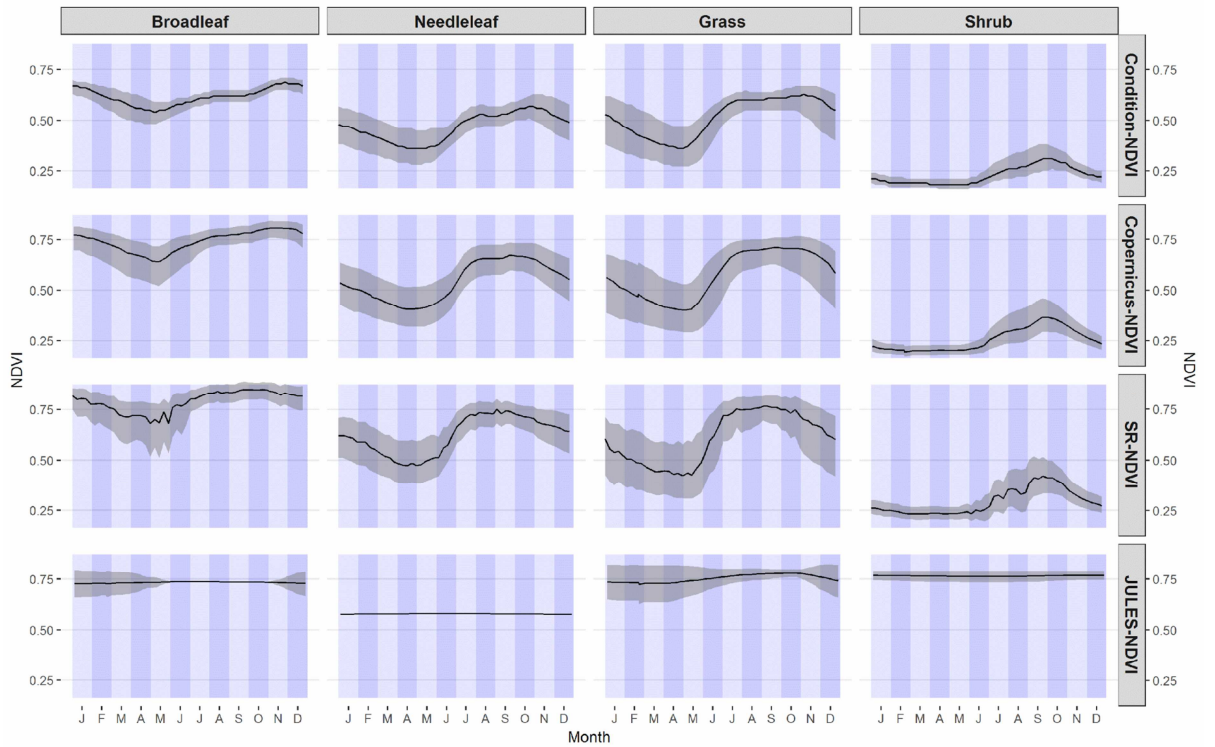


Western North America (WNA) region

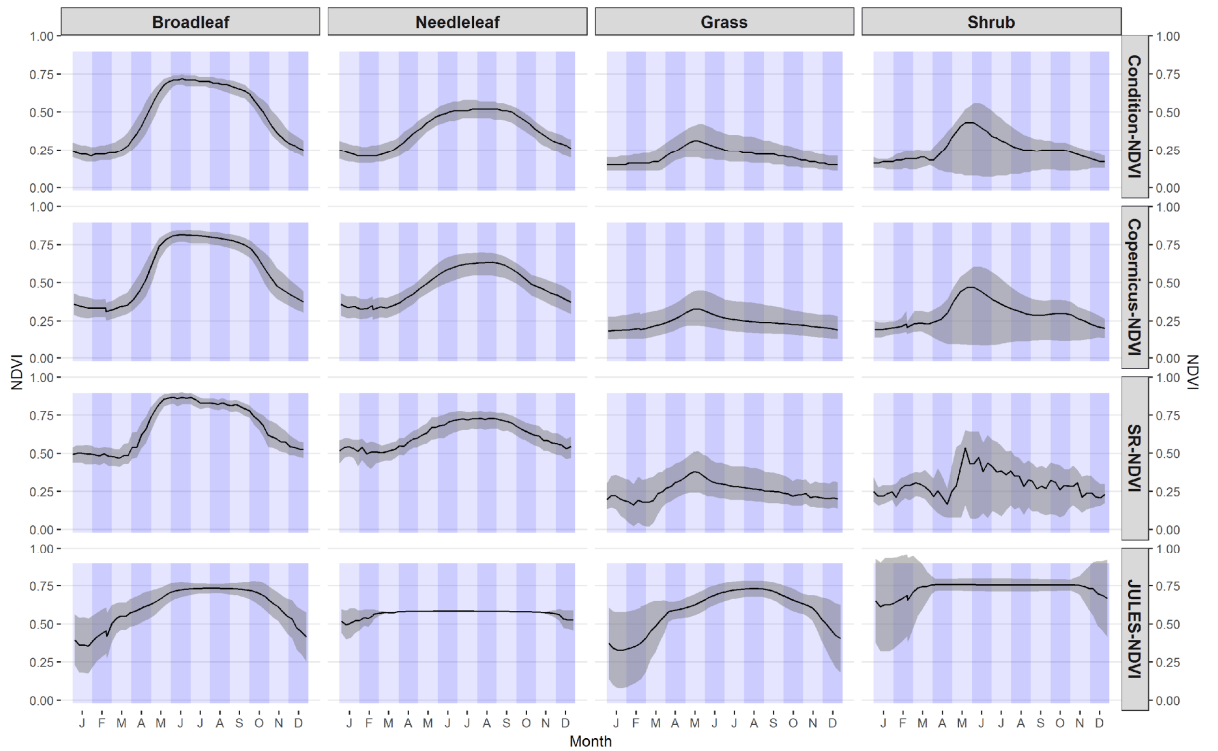




Central America (CAM) region



Central Asia (CAS) region



Central North America (CNA) region

